Adaptive Suppression of Interfering Signals in Communication Systems

by

Altin Pelteku

A Dissertation
Submitted to the Faculty
of the
WORCESTER POLYTECHNIC INSTITUTE
in partial fulfillment of the requirements for the
Degree of Doctor of Philosophy
in
Electrical and Computer Engineering
by

May 2013

APPROVED:

Professor John A. McNeill, Major Advisor

Professor Donald R. Brown III

Professor David S. Ricketts (Carnegie Mellon University)

Abstract

The growth in the number of wireless devices and applications underscores the need for characterizing and mitigating interference induced problems such as distortion and blocking. A typical interference scenario involves the detection of a small amplitude signal of interest (SOI) in the presence of a large amplitude interfering signal; it is desirable to attenuate the interfering signal while preserving the integrity of SOI and an appropriate dynamic range. If the frequency of the interfering signal varies or is unknown, an adaptive notch function must be applied in order to maintain adequate attenuation.

This work explores the performance space of a phase cancellation technique used in implementing the desired notch function for communication systems in the 1-3 GHz frequency range. A system level model constructed with MATLAB and related simulation results assist in building the theoretical foundation for setting performance bounds on the implemented solution and deriving hardware specifications for the RF notch subsystem devices. Simulations and measurements are presented for a Low Noise Amplifier (LNA), voltage variable attenuators, bandpass filters and phase shifters. Ultimately, full system tests provide a measure of merit for this work as well as invaluable lessons learned.

The emphasis of this project is the on-wafer LNA measurements, dependence of IC system performance on mismatches and overall system performance tests. Where possible, predictions are plotted alongside measured data. The reasonable match between the two validates system and component models and more than compensates for the painstaking modeling efforts. Most importantly, using the signal to interferer ratio (SIR) as a figure of merit, experimental results demonstrate up to 58 dB of SIR improvement. This number represents a remarkable advancement in interference rejection at RF or microwave frequencies.

In Loving Memory of my Mother, Marie Pelteku

Acknowledgements

This project caps a long academic journey and it is difficult, at this point in time, to avoid feeling somewhat sentimental or nostalgic while looking back and reflecting on my academic life. I have a deep feeling of gratitude towards all those sharing parts of this journey with me whether mentioned here or not.

First and foremost, I would like to thank my parents, Marie and Engjellush, for their encouragement and unconditional love. I am thankful for the love and support of my wife, Jonida, who is also my best friend. We've been blessed with two children, Mary and Stephen, who are the joy of our lives. I thank my dependable and trustworthy siblings, Nikoleta and George, for looking over their younger brother and for the memorable times growing up. I would like to recognize their families and my nephews and nieces who are very much part of my life.

I would like to thank my advisor Professor John McNeill for giving me the chance to work under his guidance. I learned a lot from his approach to problems, his patience and his overall generous attitude towards life. The noteworthy annual trips to the International Solid-State Conference were an important step in my professional development.

I would like to thank my thesis committe members, Professor Donald R. Brown III and Professor David S. Ricketts, for their consideration, review of this work and important feedback.

This work was supported by New England Center for Analog and Mixed Signal Design (NECAMSID) and BAE systems and it would not have been possible without the help and support of John Windyka, David Meharry and Frank Stroili. I would also like to thank Douglas Jansen for helping with many Cadence related questions.

Through the years at WPI I have met many caring, wonderful and very competent people, some of whom I have had the privelege of working with: Professor Fred Looft, Professor Reinhold Ludwig, Professor Diran Apelian, Professor Alexander Emanuel and many others. I would like to recognize my dependable friend, Instructor Stephen Bitar, who possesses the noble quality of dedicating his time to others.

Times spent in the NECAMSID lab were more refreshing due to project challenges but also the daily interactions and the exchange of ideas with several of my colleagues, Christopher Leonidas David, Hattie Spetla, Tsai Chen, Ali Ulas Ilhan, Chilann Chan and Alihusain Sirohiwala with whom I shared struggles and moments of camaraderie.

I would also like to thank my current colleagues and manager at Northrop Grumman as well as prior colleagues at Analog Devices, Teradyne and Ucentric, who have contributed a great deal to my professional development.

Last but not least, my journey started in Korçë, so I would like to recognize my extended family, my teachers and all my friends growing up in that corner of the world.

I thank all!

Contents

List of Figures

List of Tables

Chapter 1

Introduction

With the growing number and variety of wireless devices the need for characterizing and mitigating interference becomes a critical system consideration [15]- [70]. One important engineering problem to be considered in todays communication systems is the detection of a small amplitude signal of interest (SOI) in the presence of a large amplitude interfering signal at a nearby frequency. If the frequency of the interfering signal is known, then a fixed band-reject function, such as a "notch" filter, can be used to filter-out the interfering signal. If the frequency of the interfering signal varies or is unknown, then the notch filter must adapt to achieve adequate attenuation.

In this work, the fundamental strategy for mitigating interference issues is depicted in Fig. 1.1. The system is modeled by:

- Continuous wave signal of interest, at ω_S, and interferer, at ω_J, at a nearby frequency.
- A filtering scheme for attenuating the interfering signal.

A system level model that simulates a relevant communication environment has been constructed with MATLAB and expected improvement in interference rejection is evaluated while varying controllable design parameters. The figure of merit to be used in evaluating the system performance is the Signal to Interferer plus Noise Ratio (SINR) Improvement:

$$\text{SINR Improvement} = \frac{\text{SINR}_{out}}{\text{SINR}_{in}}, \tag{1.1}$$

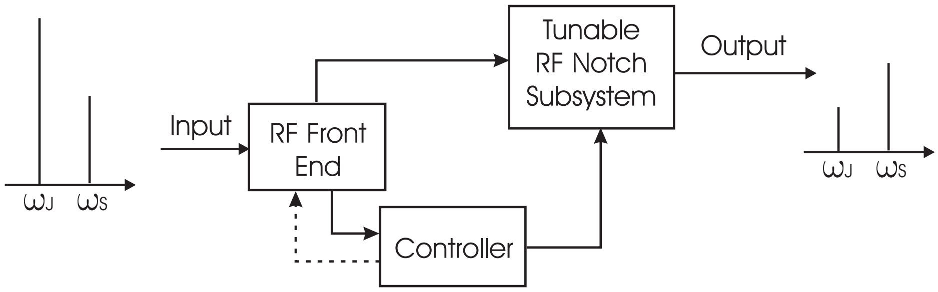

Figure 1.1: System Level Strategy.

with SINR_{out} and SINR_{in} being respectively the output and input Signal to Interferer plus Noise Ratios. The modeling strategy consists of varying critical design parameters and recording the SINR improvement; this is used in establishing a feasible performance space and design specifications. Hardware is built and tested and results are compared with modeling predictions.

1.1 Organization

This dissertation is organized in the following manner. Chapter 2 is an overview of prior interference suppression techniques used in a variety of different applications. Chapter 3 studies the performance of the filtering schemes considered in this work: a second order bandreject filter and a phase cancellation technique. MATLAB modeling results are used to determine feasible solutions and design specifications. Chapter 4 reviews theoretical concepts important to the design and test of a differential Low Noise Amplifier (LNA) and peripheral test fixtures. The design procedure and physical layouts for the LNA and test fixtures is presented in Chapter 5. Finally, test results are reported in Chapter 6 along with conclusions and discussions in Chapter 7.

1.1.1 Abbreviations

This thesis uses many abbreviations and acronyms and defines them below in Table 1.1 for the reader's convenience.

Acronym	Explanation
ADC	Analog to Digital Converter
BER	Bit Error Rate
BiCMOS	Bipolar Complementary Metal-Oxide Semiconductor
CDMA	Code Division Multiple Access
CMRR	Common Mode Rejection Ratio
CW	Continuous Wave
dB	Decibel
GSM	Global System for Mobile communications
FEM	Finite Element Modeling
FSK	Frequency Shift Keying
IC	Integrated Circuit
IF	Intermediate Frequency
IMD	Intermodulation Distortion
IP3	Third-Order Intercept Point
LNA	Low Noise Amplifier
NF	Noise Figure
ω	Radian Frequency
MMIC	Monolithic Microwave Integrated Circuit
RADAR	Radio Detection and Ranging
RF	Radio Frequency
RFID	Radio Frequency Identification
SIR	Signal to Interferer Ratio
SINR	Signal to Interferer-plus-Noise Ratio
SNR	Signal to Noise Ratio
SOI	Signal of Interest

Table 1.1: Common Abbreviations.

Chapter 2

Background

This section discusses interference mechanisms and their importance in different communication standards, while presenting existing solutions in different applications along with their strengths and drawbacks.

2.1 Motivation

The growth in the number of wireless devices and applications has led to a crowding of the wireless spectrum and more stringent requirements for receiver designs. Radio frequency interference continues to be a persistent problem in many communication systems and will potentially exacerbate as the unused wireless spectrum continues to shrink. There are, in general, two types of interfering signals:

1. Intentional jammers used in military applications, such as electronic warfare (EW).

2. Unintentional, yet harmful interference, primarily associated with wireless commercial systems.

In heterodyne receivers, depicted in Fig. 2.1, a fundamental tradeoff involves balancing between image-rejection and adjacent channel suppression [3]. In direct conversion receivers, shown in Fig. 2.2, LO leakage and second order distortion can be troublesome [2]. Nonlinearities, which can occur in every component, play an important role in a receiver's inherent robustness to interfering signals. Whereas noise sets the floor of the dynamic range or the

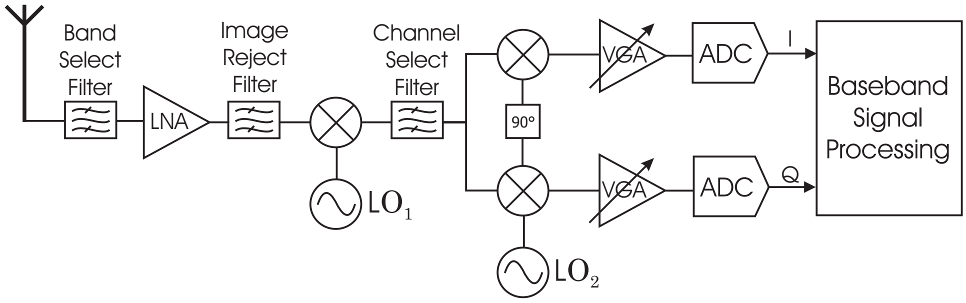

Figure 2.1: Typical Heterodyne Receiver Chain.

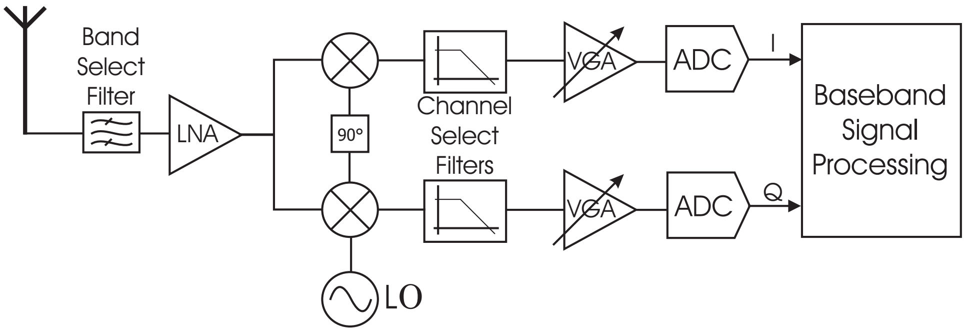

Figure 2.2: Direct Conversion Receiver.

minimum discernible signal (MDS), nonlinear behavior sets the ceiling of a receiver's dynamic range. Related figures of merit include the input (or output) third order intercept point (IP3), 1dB compression point or out-of-band blocking. Depending on the strength of the interfering signal and receiver's inherent linearity, either of the following can occur:

1. Intermodulation interference, describing a scenario when out-of band signals mix to produce in-band interfering tones that can be mistaken for a real signal.

2. Blocking or desensitization, in cases when the interferer is strong enough to reduce the sensitivity of the receiver or even saturate the front-end electronics, such as the LNA.

2.1.1 Intermodulation Interference

When two tones are added together in a non-linear element, in addition to the signals at the input frequencies, other comensurate frequency components are generated at the output. Third order intermodulation products (IMD) are especially troublesome because their proximity to the desired signals makes them difficult to filter out; higher order IMD products, albeit weaker, are also generated. For two similar strength out-of-band signals the power generated in the third order product is given by: $\mathrm{P}_{\mathrm{IMD}} = 3P_i - 2\mathrm{IIP3}$, where $\mathrm{P}_{\mathrm{IMD}}$ is the power of the IMD signal generated by two tones of input power P_i in a receiver with a third order input intercept point of IIP3. The frequencies at which these components are generated are depicted in Fig.2.3 below. IMD products are generally much weaker than

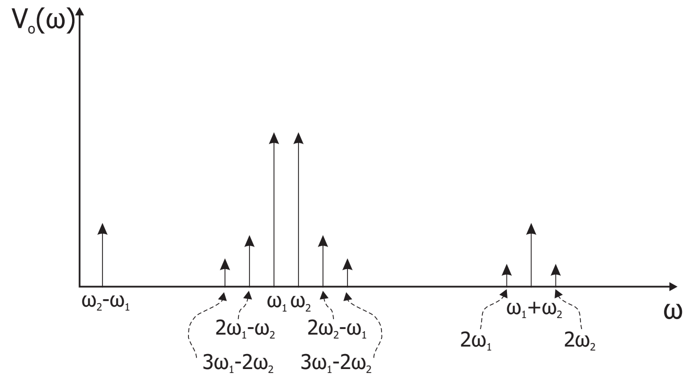

Figure 2.3: Generic Nonlinear Behavior of Active Devices.

the signals that generate them, however, large amplitude interfering tones, which may be outside the receivers passband, generate spurious signals that interfere with and can obscure a weak, desired signal. Even-order IMD products usually occur at frequencies well above or below the desired passband and are easily rejected by channel filters. The greatest concern are third-order products that occur at $2\omega_1 - \omega_2$ and $2\omega_2 - \omega_1$, where $2\omega_1 - \omega_2$ and $2\omega_2 - \omega_1$ denote the mixing frequencies. Third order IMD products, typically the strongest of all odd-order products, often cannot be rejected by filters, therefore, degrading the signal to noise ratio (SNR) and the overall performance of the receiver.

2.1.2 Blocking or Desensitization

Desensitization refers to the scenario when the gain of a small, desired signal compresses as the power of a large interfering signal is increased. As the power of the interfering tone increases, the gain of a component may compress or even saturate, resulting in further degradation of SNR for all wanted signals; the effect may be referred to as desensitization or blocking [1]. The reduced gain results in lower sensitivity, lower SNR and reduction of the receivers capacity to process in-band signals. The safe blocking power level depends on the type of system or application. For example, commercial wireless systems often specify linearity in terms of 1dB compression point since at such point severe degradation in audio quality is encountered. In pulsed RADAR systems a 0.1dB gain compression or expansion can be detrimental to clutter removal [46].

2.1.3 Cross-Modulation Distortion

Cross modulation is the transfer of modulation from one signal to another in a nonlinear circuit. The process of cross-modulation distortion is highlighted in Fig. 2.4 for a typical CDMA transceiver [14]. Due to finite rejection of the duplexer, transmitter power leaks into

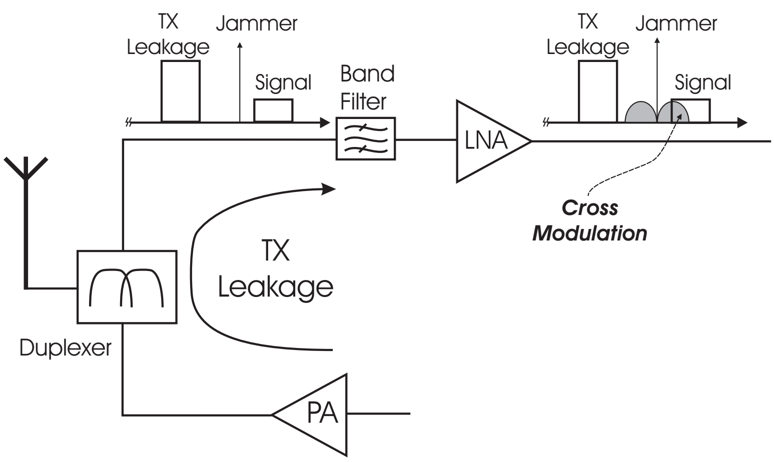

Figure 2.4: Cross-Modulation Distortion.

the receive path. This “TX leakage” can mix with a strong jammer and resulting modulation can occupy part of the receive band. Modulation transfer to the receive carrier is enabled by the presence of a strong interfering tone and can occur whenever two modulated signals are simultaneously present in the same circuit. The overall effect on a receiver is lower sensitivity and lower SNR.

2.2 Prior Work in Interference Suppression

The body of work dealing with interference cancellation is diverse and evolving everyday along with new requirements and applications for wireless technologies; an overview of prior work is divided in separate categories for similar application areas.

2.2.1 Cellullar Applications

Cellullar communication systems impose stringent operating conditions. A 900MHz GSM channel, for example, has blocker requirements depicted in Fig. 2.5. In time division duplex (TDD) systems, such as GSM, jamming signals can originate due to co-channel interference from other users or ACI from adjacent operating bands. In frequency division

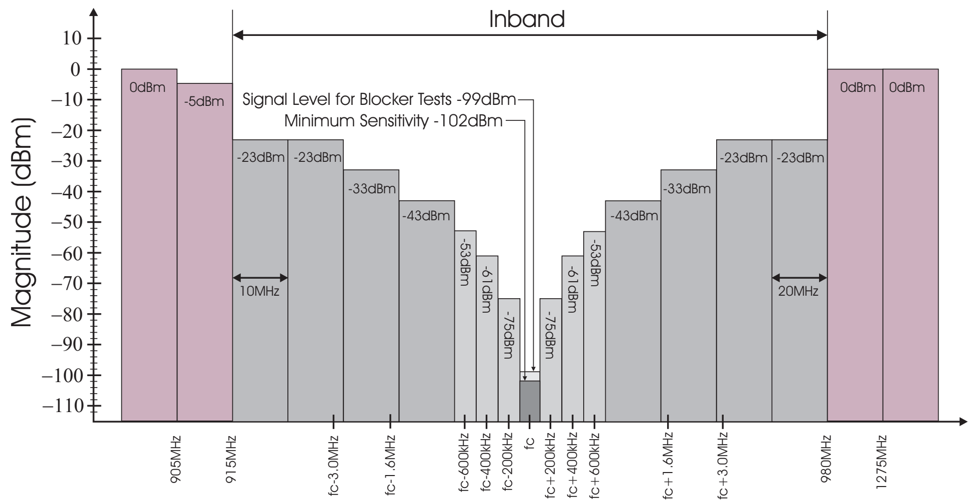

Figure 2.5: GSM 900 Blocker Specifications.

duplexing (FDD) schemes, such as WCDMA, blocking signals are dominated by TX leakage. Blocker profile for WCDMA is depicted in Fig. 2.6. When strong enough the TX leakage signal can saturate the receiver, or it can generate second order intermodulation distortion

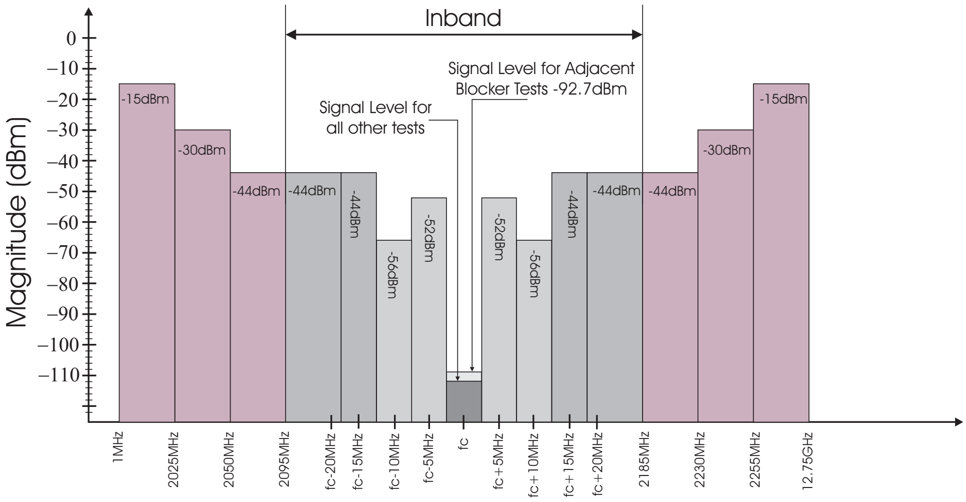

Figure 2.6: WCDMA Blocker Specifications.

(IMD_2) at baseband in direct-conversion mixers. In addition, mixing with nearby strong jammers generates cross-modulation distortion (XMD) that falls in the desired band [14]. The topic of interference in cellular communications has been extensively researched and published beginning with 2G and more recently in 3G networks [13]- [21]. With well regulated transmission and reception of user equipment and of base stations 99.99% of the signals received lie below −40dBm power level [4], which decreases the likelihood of blocking/desensitization and IMD interference type becomes more prevalent. The high demand for spectrum resources by the co-existance of different networks and standards can be more efficiently accomodated via dynamic allocation schemes [5]. Co-channel (CI) and adjacent channel interference (ACI) are the main concerns [6], [7] in spectrum sharing environments reducing network capacity [8] and increasing the probability of bit-error [9]. The probability of blocking can be markedly reduced with careful choice of a guard band, or an empty frequency band, inserted between two adjacent operating bands [10]. A wider guard band performs better in reducing ACI [11] yet consumes significant spectral resources and reduces network capacity [12].

An analysis of different interference mechanisms contributing to coverage reduction in WCDMA systems are explained in [13]; their coverage reduction effects are modeled and simulated using ray-tracing propagation models [14] for the path loss in urban environments. In [15] interference between CDMA and GSM was experimentally investigated on the PCS band with real base transceiver stations (BTS) and handsets; handset and BTS receiver desensitization as a function of SIR and guard band have been plotted. The importance of guard band separating adjacent carriers of different CDMA operators has been in investigated in the context of the spatial near-far problem [16]; theoretical interference prediction models have been derived and their accuracy confirmed in a laboratory test environment. Measured co-site spurious emission data between PCS1900 and WCDMA base stations is presented in [17] and outage probability in PCS1900 mobile stations simulated in [19]. Degradation in sensitivity and noise figure due to adjacent channel interference using GSM standards at 900 MHz has been simulated in [20]; results are studied for different guard bands as a function of coupling loss in coordinated operation modes.

Spread spectrum systems are inherently robust to narrow band interference (NBI) [22], however, system performance can be affected by producing a significant number of error bits; research has shown suppressing NBI prior to despreading markedly reduces the BER [23]-[26]. Adaptive filtering makes use of the fact a spread spectrum signal, resembling the flat spectrum of white noise, cannot be predicted accurately, whereas a good sampling of past values facilitates a good estimate of the narrow band interferer, which is subsequently subtracted from the spectrum of the received signal; the filtering is usually accomplished at DC or low IF with digital signal processing. Early work relied upon adaptive linear prediction and interpolating filters [27], [28] while nonlinear filters have shown even better results [29]. Good SNR improvement can be expected if the input SNR is high enough [28], otherwise improvement decreases significantly; one troublesome scenario involves a weak SOI in the presence of a strong interferer nearby, especially if the front-end electronics or the down conversion mixers saturate, digital signal processing can't recover the desired spectrum.

Hardware implementations of blocker suppression range from baseband channel select filters [34]- [35] to LMS adaptive filters [33] and analog front-ends with feed-forward amplification [42]- [44]. In [34] an opamp RC leapfrog filter [36] is implemented with common-mode feedback that adjusts the open-loop gain of the opamp; power dissipation is kept low by drawing a supply current according to the magnitude of the blocker. In [35] a cascaded channel select filter with two single-pole RC sections combined with g_m-C sections is integrated into a WCDMA receiver IC. In [33] the problem of TX leakage in CDMA receivers has been addressed with an LMS adaptive filter; an out of phase copy of the TX leakage is added through an auxiliary path to the output of the receive LNA. The LMS algorithm appropriately scales the in-phase and quadrature components of the copy so as to match the TX leakage signal at the output of the LNA.

Suppression using Feed-forward Amplifiers

Traditionally, feed-forward amplifiers have been utilized to reduce distortion [37]- [41]. Recently, there is renewed interest in adopting feed-forward techniques to suppress narrowband interference at the front-end of a receiver [42]- [44]; the simplified block diagram of the method is depicted in Fig. 2.7. The receiver consists of a main path LNA that amplifies

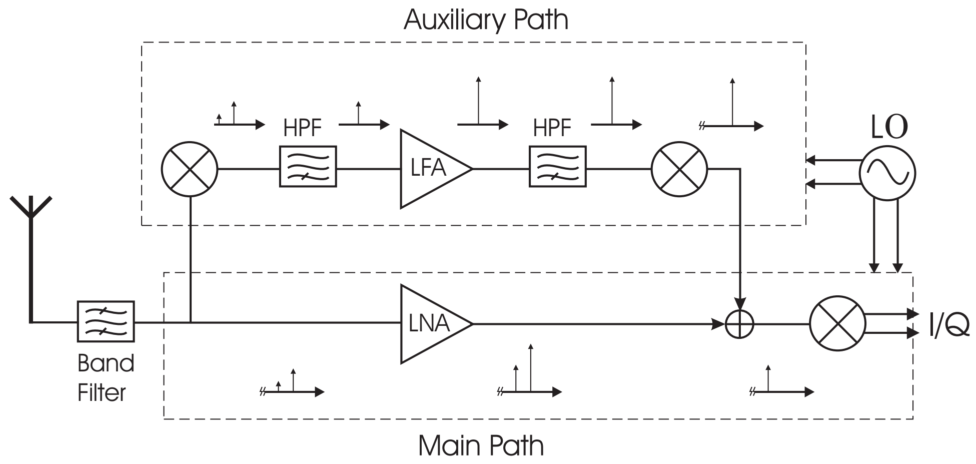

Figure 2.7: Feedforward Cancellation.

all signals. An auxiliary path downconverts all signals to baseband and applies a high-pass filter that rejects the desired signal. Low frequency amplification and up-conversion stages adjust the amplitude of the interfering tone so as to replicate that of the main path. When summation is applied at the output of the LNA, destructive interference nullifies the interfering tones.

A 1GHz front-end incorporating feed-forward cancellation has been implemented in 0.13μm

CMOS with measured data showing rejection of up to 25dB [43]. In [42] 27dB blocker rejection is achieved at cellullar bands with a receiver fabricated in 0.18μm CMOS. Feed-forward cancellation in a 65nm CMOS receiver improves blocker rejection by $\geq$ 21dB [44].
The feed-forward technique can work well if the amplitudes and phases of the interfering tones are matched at the summation point; hard nonlinear behavior in the LNA or the auxilliary path may reduce its suppression ability via AM-AM or AM-PM. In addition, large interferers can render the technique ineffective by saturating the front-end.

2.2.2 Scenarios in Military Environments

Contrary to situations in regulated commercial wireless environments, jamming of communication links consists of purposeful interference generation in areas of interest in the electromagnetic spectrum; it is often part of a larger military strategy or campaign. It can be used not only to disrupt the opponent's command and control but often to diminish the propaganda capability by jamming TV and radio channels. Its effectiveness is displayed in making speech unintelligible, in analog systems, or significantly degrading the BER in digital systems so as to cause unreliable communication. Depending on the scheme used it can be classified in the following categories [45]:

1. *Narrowband or partial-band jamming* targets the carrier frequency thereby swamping the reception of the signal of interest. Partial band jammers can be effective against spread spectrum receivers as well, when enough power is transmitted and the jamming device is positioned close to the receiver causing unreliable reception. The narrowband technique is often deployed in friendly territory, otherwise known as standoff jammers, since impact on friendly communications can be minimal.

2. *Barrage jamming*, on the other hand, consists of emission over a broad frequency range, or sweeping the emitter's frequency fast enough so that the effect is nearly instantaneous. Barrage jammers are often deployed in an adversary's territory, also known as standin jammers, for the reason of minimizing negative impacts on friendly communications.

3. A *Follower jammer* employs the strategy of acquisition and tracking a target's corre-

sponding frequency [47]; this is typical for targets that rapidly change their broadcast frequency, like in frequency hopping, in order to combat harmful interference. The price tag and complexity of such jamming scheme are its main drawbacks. Fundamental limitations of repeater jamming due to frequency estimation and signal sorting are derived in [48].

Degradation of speech intelligibility in FM and AM analog modulated systems under jamming conditions has been plotted in [49]. The anti-jam performance of fast frequency hopped FSK systems in multitone partial band jamming environments has been evaluated [50]. Curves for BER versus energy per bit to jammer spectral density $\left[\frac{E_b}{N_J}\right]$ have been plotted; with convolutional coding anti-jam performance is significantly improved. The ergodic capacity of frequency-hopped MIMO systems has been studied under the influence of uniform partial-band noise jamming with numerical simulations demonstrating that space-time coded systems are robust to this type of intentional interference [51]; here the ergodic capacity refers to the ensemble-average capacity of the channel. The anti-jam properties and ability of MIMO systems to improve packet error rates for different SIRs has been quantified in [30].

Improvement schemes in military or aerial communications often takes the form of space-time adaptive processing (STAP) where nulls are inserted in the direction of sidelobe jammers [52]; the idea is depicted in Fig. 2.8. A challenging scenario arises when jammers and signals of interest are colocated in the mainbeam of an antenna array. Using narrow-beam antenna arrays mainbeam jammers with spatial angular separation from the SOI $\gtrapprox 20\%$ of the half-power beamwidth (HPBW), spatial nulls can still be inserted to improve SNR by about 10dB [54]. In [53] strong jamming signals are cancelled using a tapped-delay line correlator; sufficient information about the jamming frequencies is assumed. Wideband interference from multiple beam jammers is suppressed using a set of auxiliary antennas with adaptive tapped delay lines in [55]; in the absence of system errors better than 60dB improvement can be achieved. Space fast-time adaptive processing have emerged as an alternative to the conventional STAP techniques using coherent multipath reflections from the terrain to suppress the mainbeam jammer [56]. In [57] an algorithmn that exploits coherent interferer multipath has been implemented in defeating mainbeam jamming showing

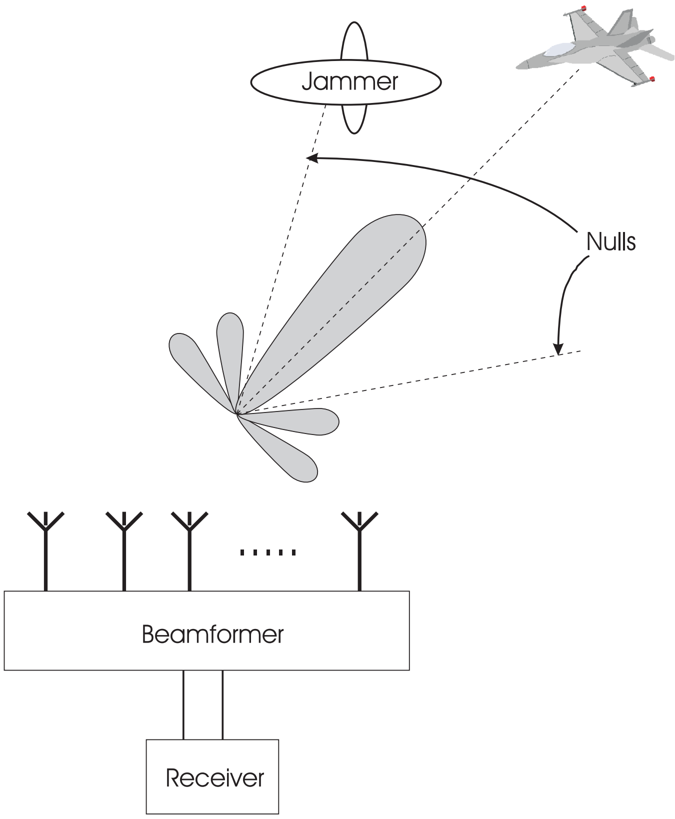

Figure 2.8: Space-time Adaptive Processing.

improvements of up to 47dB.

2.2.3 Unlicensed Bands and Wireless Networks

Devices and protocols operating in the unlicensed frequency bands have become popular over the years; the industrial, scientific and medical (ISM) band around 2.4GHz (US) and the unlicensed national information infrastructure (UNII) band around 5.2GHz (US) exemplify the growth and consequent challenges. Ubiquitous applicable standards and devices include, in the 2.4GHz ISM band, wireless LANs (802.11 b/g/n), bluetooth, cordless phones and microwave ovens, along with 802.11a and many wireless internet service providers (WISPs) in the UNII band. The growing popularity of deployed devices and the number of new standards sharing this band increases the likelyhood of mutual and harmful interference. Colliding signals from two or more nodes can cause lost packets reducing overall network performance; henceforth, much of the effort has focused on communication techniques that are inherently more robust to interference. With Orthogonal Frequency Division Multiplexing (OFDM) being the technology of choice for many wideband wireless communication systems operating in the unlicensed bands, like 802.11 a/g/n, performance evaluation of OFDM systems is often synonymous with the larger research effort in this area.

The performance of IEEE 802.11g wireless LAN receivers under the influence of narrowband interference has been evaluated [58]. Measuring packet error rate (PER) as a function of signal to jamming ratio (SJR) for different data rates shows that narrowband interference has a significant impact on the performance of an OFDM system. The impact of narrowband interference on the performance of an OFDM ultra-wideband (UWB) receiver and in particular on the degradation of the SINR at the output of an ADC has been analyzed in [59]; an analog front-end technique based on a feed-forward approach to suppress NBI in UWB receivers is presented in [60]. Suppressing the NBI of Bluetooth packets on IEEE 802.11g systems via two methods, a differentiation in frequency direction algorithm and a median filter, has been proposed in [61]. In many other instances, however, the interfering signal is wideband, often employing similar communication protocols. The performance of IEEE 802.11b under IEEE 802.15.4 (low-rate WPAN) interference has been modeled and simulated in [62] and experimentally characterized in [63]; measurements with the newer 802.11g/n standards, instead of 802.11b, have been recorded in [64]. A mathematical model for the BER of 802.11b and bluetooth communications in the presence of RFID interference has been used to quantify the network's performance degradation [65]; simulation results are compared to what's predicted by theory. In [66] the number of interfering signals has been modeled as a poisson process in the frequency and space domain, while a closed form expression for quantifying CW randomly distributed interfering signals in the unlicensed bands has been derived. The performance of commercial wireless devices operating in the 2.4 GHz ISM band has been investigated using interference temperature as a proxy [67] with measurements showing a lower limit than predicted by theory; here interference temperature describes the robustness of a radio to interference in its spectrum space [68].

2.2.4 Other Communication Systems

Other systems that countinually strugle with in-band interference include, among others, GPS and Satellite Systems, Software Defined Radio and RFID. Many satellite systems operate in the unlicensed bands, such as 2.4 GHz, so they share the problems and solutions presented in Section 2.2.3.

In Software Defined Radio the effects of jamming on wideband digital receivers have been investigated and probability of bit error versus jammer to signal ratio with and without automatic gain control (AGC) has been numerically evaluated [71]; systems with AGC show better resistance to interference and susceptibility to strong jamming signals can be improved by employing techniques such as coding or adaptive “notch” filtering.

The operation of a GPS receiver can severely be limited or completely disrupted in the presence of in-band interference and jamming signals. The effects of jamming on GPS reception are twofold:

1. RF interference results in reduced signal to noise ratio values. As the signal to noise ratio drops below an acceptable level the satellite can no longer be tracked.

2. The GPS receiver may cease to track satellites when placed close to a transmitting source. This is due to “blocking” of the “front end” of the receiver and is independent of transmitting frequency.

In typical RFID systems, the reader can transmit up to 30dBm (1W) of RF power in order to activate and communicate with the RFID tag. Conversely, the RFID receiver must be able to detect powers as low as -80dBm or less, in the presence of TX leakage signals as high as 10dBm. In order to accommodate such a wide dynamic range the receiver must reject or suppress a large blocker that is only a few hundred kHz away from the desired signal; present microwave technology struggles to accomplish such task.

2.3 Novelty of this Work

In most of the work referenced in this thesis interference rejection is improved via digital signal processing techniques at baseband; such methods work relatively well if nonlinearities do not significantly degrade the input-output characteristics at the RF front-end so as to cause hard distortion or blocking. In either scenario, it may be beneficial, depending on the severity of the nonlinearities, to provide some rejection in the analog front-end. The approached pursued in this work allows for the capability to adaptively tune to an interfering signal and suppress it; such system involves two main architectural components:

1. The RF front end that accomplishes the suppression of the jammer and

2. A control algorithm that tracks the interfering signal's frequency.

This project demonstrates the suppression capability of an analog front end and its implementation in hardware; the control algorithm part is not discussed here.

2.3.1 Goals

The goals of this thesis are summarized below.

1. Develop the theoretical background to facilitate computer modeling of the system and the proposed solution scheme

2. Conduct computer simulations to determine improvement bounds based on an appropriate figure of merit and develop feasible design specifications

3. Implement the proposed solution method with a capable RFIC front-end

4. Design RF subsystems and peripheral devices that communicate with the RFIC front-end

5. Test and correlate results to model predictions

Chapter 3

System Modeling and Solutions

3.1 System Modeling with Matlab

The filtering schemes considered in this chapter consist of a second order bandstop filter and a phase cancellation system.

3.1.1 Parameters in Performance Space

The frequency domain response of a desired "notch" function depicting critical parameters is shown in Fig. 3.1 below, where ω_S and ω_J referer to the wanted signal and interferer frequencies, respectively. Several challenges that affect SINR improvement can be recog-

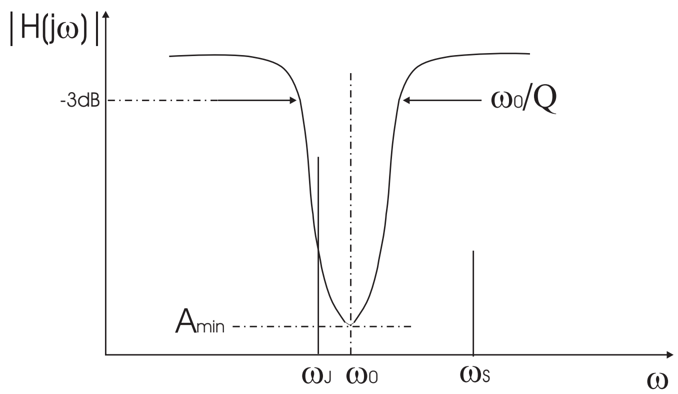

Figure 3.1: Parameters in performance space.

nized in designing a suitable filter:

- Notch Depth (A_{min})
- Center Frequency Accuracy ($\omega_0 \cong \omega_J$)
- Quality Factor (Q), Bandwidth (BW) ($Q = \dfrac{\omega_0}{BW}$)
- Accurate setting of the rejection frequency ($\omega_0 \cong \omega_J$)
- Interferer proximity to SOI ($\omega_J \cong \omega_S$)

The feasibility study with MATLAB consists of recording SINR improvement while varying filter parameters and interferer proximity to the SOI.

3.2 Performance Predictions using 2-nd Order Notch Filter

A second order band-reject filter with the following transfer function has been constructed and simulated using MATLAB:

$$H(s) = \frac{s^2 + \left(\dfrac{A_{min}\ \omega_0}{Q}\right) s + \omega_0^2}{s^2 + \left(\dfrac{\omega_0}{Q}\right) s + \omega_0^2}, \tag{3.1}$$

where ω_0 is the center frequency, Q the quality factor and A_{min} the stop band rejection. The simulations for the bandreject filter are carried out in two steps:

- Two tone simulations where only the SOI and the interferer are considered and the performance is based on signal to interferer ratio (SIR) improvement.
- Total noise in the channel is added to the previous category and SINR improvement is evaluated and plotted.

3.2.1 Proximity and Accuracy Investigation

SIR improvement for the two tone environment is evaluated as:

$$\text{SIR Improvement} = \frac{\text{SIR}_{out}}{\text{SIR}_{in}} = \frac{\dfrac{P_S|H(\omega_S)|^2}{P_J|H(\omega_J)|^2}}{\dfrac{P_S}{P_J}} = \frac{|H(\omega_S)|^2}{|H(\omega_J)|^2} \tag{3.2}$$

where P_S, P_J denote the signal power and interfering tone power, respectively, whereas $|H(\omega_S)|$ and $|H(\omega_J)|$ denote the corresponding transfer function magnitudes at the signal and interferer frequencies. Figure 3.2(a) shows a surface plot of SIR improvement as a function of proximity (closeness of ω_J to ω_S) and accuracy (closeness of ω_0 to ω_J) for a fixed Q (Q=50), while Fig. 3.2(b) displays its contours taken as cross-sections in the xy-plane. The plot indicates that SIR improvement is positively affected as separation between

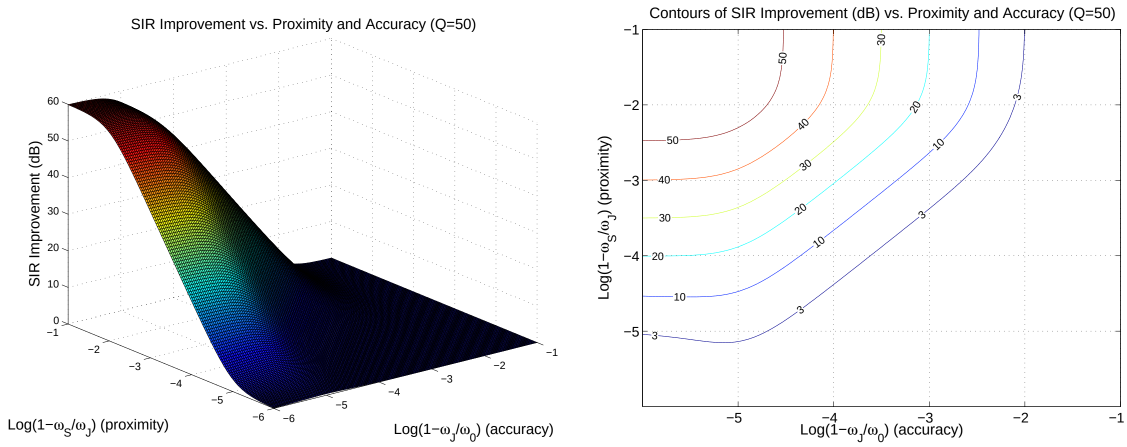

(a) 3D Surface (b) Contours

Figure 3.2: SIR Improvement vs. Proximity and Accuracy

the signal (ω_S) and interferer frequency (ω_J) increases, however, improvement tapers off as the accuracy of setting the center frequency of the filter degrades. Targeting 40dB SIR improvement, Figure 3.3 shows fixed (40dB) improvement contours for four filter quality factor values (Q = 10, 30, 50 and 100). Higher Q filters perform better whenever the center frequency is accurately set and the interferer is close to the signal; however, a lower Q offers better improvement when accuracy is limited and the interferer frequency is much different from that of the signal. The plot accentuates the need for accurately tracking the interferer frequency, or $\omega_0 \cong \omega_J$.

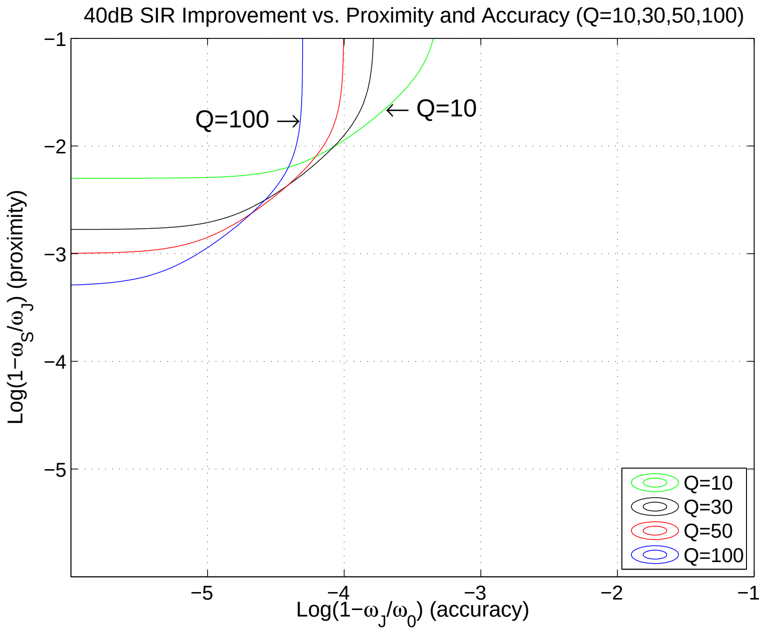

Figure 3.3: 40dB SIR Improvement vs. Proximity and Accuracy

3.2.2 Effect of Input Noise Power and Noise Figure

With the input and output noise power levels denoted as N_i and N_o, respectively, SINR improvement is evaluated:

$$\frac{\mathrm{SINR}_{out}}{\mathrm{SINR}_{in}} = \frac{\dfrac{P_S\left|H\left(\omega_S\right)\right|^2}{P_J\left|H(\omega_J)\right|^2+N_o}}{\dfrac{P_S}{P_J+N_i}} = \frac{\left|H\left(\omega_S\right)\right|^2\left(P_J+N_i\right)}{P_J\left|H\left(\omega_J\right)\right|^2+N_o} \tag{3.3}$$

$$= \frac{P_J\left|H\left(\omega_S\right)\right|^2+N_i\left|H\left(\omega_S\right)\right|^2}{P_J\left|H\left(\omega_J\right)\right|^2+N_o} = \frac{\dfrac{P_J}{N_i}+1}{\dfrac{P_J\left|H\left(\omega_J\right)\right|^2}{N_i\left|H\left(\omega_S\right)\right|^2}+NF} \tag{3.4}$$

where the noise figure of the system NF is defined as:

$$NF = \frac{N_o}{N_i\left|H\left(\omega_S\right)\right|^2} \tag{3.5}$$

Figure 3.4(a) shows a surface plot of SINR improvement as a function of noise figure, interferer and input noise power levels for a fixed Q, while Fig. 3.4(b) displays its contours.

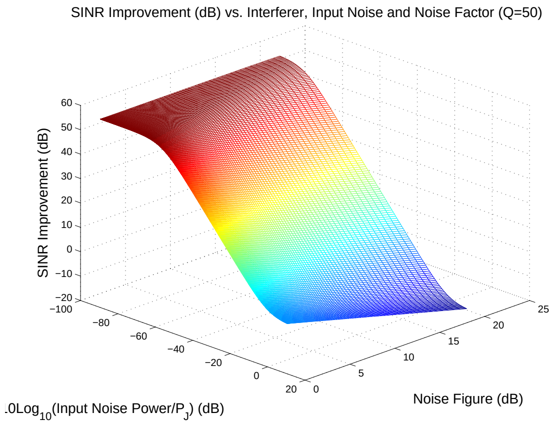

(a) 3D Surface

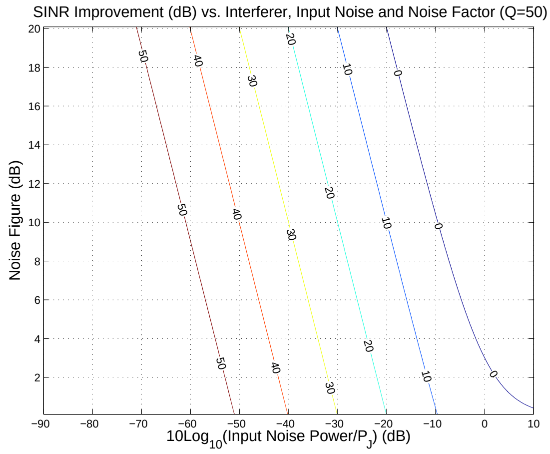

(b) Contours

Figure 3.4: SINR Improvement vs. Noise Figure, Interferer and Noise Power

Chosen accuracy and proximity levels are, respectively, $\dfrac{\omega_J}{\omega_0} = 1 - 10^{-4}$ and $\dfrac{\omega_S}{\omega_J} = 1 - 10^{-1}$. The plots show that as the input channel noise power increases a lower NF is necessary in order to maintain the same SINR level; improvement is severely limited when noise power dominates, in effect filling up the notch. Additionally, in order to maintain a targeted improvement both noise figure, design dependent, and input noise power must be under certain values.

3.2.3 Performance Limitations with Typical RF Filters

Tunable, lumped element band-reject filters require multiple poles in order to achieve steep frequency roll-offs. Additional components increase parasitic losses, which in turn degrade the overall filter quality factor and reduce tunable range. Fixed-frequency, commercial filter designs in 1-3GHz RF bands can satisfy stopband rejections in the range of 20-40dB. The challenges of a notch filter design for a chosen 0.2% proximity $(\dfrac{\omega_S}{\omega_J})$ are highlighted in Fig. 3.5, where $\omega_0 = \omega_J$ (absolute accuracy). In order to achieve 40dB SIR improvement better than 57dB rejection is warranted when Q=30; while fixed-frequency microwave filters have trouble meeting such specification, the task becomes impractical with tunable ones.

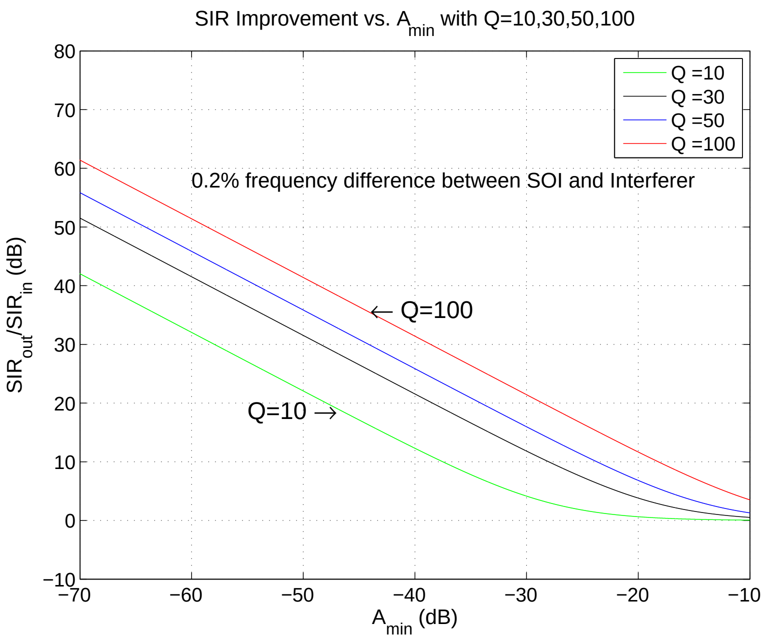

Figure 3.5: Improvement Contours vs. Stopband Rejection.

Furthermore, deviations from the assumed absolute accuracy will impose further stringent filter requirements. Therefore, while the second-order filter solution presents a starting point for developing the theory, it is impractical and other options need to be considered.

3.3 Proposed Phase-Cancellation Technique

An attractive approach for implementing the notch function in integrated circuits is the phase cancellation technique depicted in Fig. 3.6. It consists of a tunable bandpass filter that tracks the interferer, a tunable time-delay network that adjusts the phase, and a differential amplifier that rejects common-mode signals. Ideally, the interfering tones appear in-phase (common-mode) at the differential inputs of the amplifier, while the SOI tones are out of phase. The total transfer function is not exactly in the form of (3.1), but with appropriate choice of design parameters a similar notch function can be obtained [151].

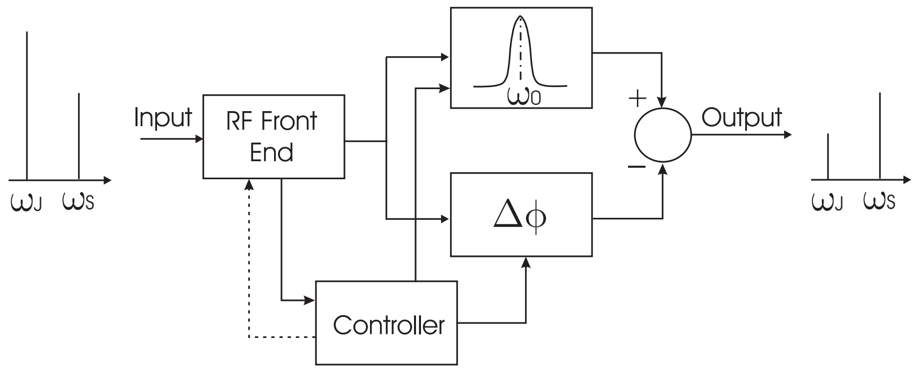

Figure 3.6: Phase Cancellation System.

3.3.1 System Solution

To study the notch behavior of the phase-cancellation design a mathematical derivation is carried by matching the phases of the interfering tones at the input of the differential amplifier. Considering the transfer functions of the bandpass filter and the phase delay network, respectively, to be:

$$H_B(\omega) = \frac{j\omega\left(\dfrac{\omega_B}{Q_B}\right)}{-\omega^2 + j\omega\left(\dfrac{\omega_B}{Q_B}\right) + \omega_B^2} \tag{3.6}$$

$$H_{\Phi}(\omega) = (1+\alpha)\, e^{-j\omega\tau} \tag{3.7}$$

where ω_B, Q_B are the center frequency and quality factor of the bandpass and α, τ are the amplitude adjust and the time constant of the phase delay network. With A_d being the differential gain of the amplifier, the total transfer function of the system is:

$$H_T(\omega) = A_d\left[H_B - H_{\Phi}\right] = A_d\left[\frac{j\omega\left(\dfrac{\omega_B}{Q_B}\right)}{-\omega^2 + j\omega\left(\dfrac{\omega_B}{Q_B}\right) + \omega_B^2} - (1+\alpha)\, e^{-j\omega\tau}\right] \tag{3.8}$$

In order to find where the minimum of the phase cancellation system occurs, one must solve $\dfrac{d|H_T|}{d\omega} = 0$, which results in a transcedental equation that to a first-order approximation yields a fifth-degree polynomial having no closed-form solution. An alternative approach to finding the minima is derived from the assumption that this minima occurs at the frequency where the input tones to the differential amplifier are in phase:

$$\begin{aligned}
\angle H_T(\omega_0) &= \angle H_B(\omega_0) \\
-\omega_0\tau &= \angle \frac{\left[\dfrac{\omega_0\omega_B}{Q_B}\right]^2 + j\left[\dfrac{\omega_0\omega_B^3}{Q_B} - \dfrac{\omega_0^3\omega_B}{Q_B}\right]}{\left[\left(\omega_B^2-\omega_0^2\right)^2 + \left(\dfrac{\omega_0\omega_B}{Q_B}\right)^2\right]} \\
-\omega_0\tau &= tan^{-1}\left[\frac{\left(\omega_B^2-\omega_0^2\right)Q_B}{\omega_0\omega_B}\right] \qquad (3.9)
\end{aligned}$$

For small arguments the arctan function can be approximated to a first-order by $arctan(x) \approx x, for\ x \approx 0$, so:

$$\begin{aligned}
-\omega_0\tau &\approx \left[\frac{\left(\omega_B^2-\omega_0^2\right)Q_B}{\omega_0\omega_B}\right] \\
\omega_0 &\approx \omega_B\sqrt{\frac{Q_B}{Q_B-\omega_B\tau}} \qquad (3.10)
\end{aligned}$$

with the caveat that $\omega_0 \approx \omega_B$. Utilizing 3.10 derivations of the bandwidth and quality factor of the resulting notch function are as follows:

$$BW = \omega_u - \omega_l \qquad (3.11)$$

$$Q_T = \frac{\omega_0}{BW} \qquad (3.12)$$

where ω_u, ω_l represent frequencies where $|H_T|^2 = \frac{1}{2}$ and specifically

$$\omega_u \cong \omega_B\left[\sqrt{\frac{Q_B-2\omega_B\tau+1}{Q_B-4\omega_B\tau}}\right] \qquad (3.13)$$

$$\omega_l \cong \omega_B\left[\sqrt{\frac{Q_B-2\omega_B\tau-1}{Q_B-4\omega_B\tau}}\right] \qquad (3.14)$$

and so

$$BW \cong \omega_B\left[\sqrt{\frac{Q_B-2\omega_B\tau+1}{Q_B-4\omega_B\tau}} - \sqrt{\frac{Q_B-2\omega_B\tau-1}{Q_B-4\omega_B\tau}}\right] \qquad (3.15)$$

$$Q_T \cong \frac{\sqrt{Q_B-4\omega_B\tau}}{\sqrt{Q_B-3\omega_B\tau+1}-\sqrt{Q_B-3\omega_B\tau-1}} \qquad (3.16)$$

3.3.2 Transfer Function Behavior

To verify the solution presented in the previous section a system model similar to the one used in the 2^{nd} order bandreject filter was built with Matlab and functionality studies were carried out. Two different conditions are studied:

1. Both ω_S and ω_J are on the same side of the filter's passband

2. ω_S and ω_J are on different sides of the filter's passband

These scenarios are depicted in Fig. 3.7. It is important to note that the time-delay network is implemented as a variable phase shifter that tracks the phase of the bandpass and consequently the phase of the interferer. A discussion may arise given the distinction between phase shifters and time-delay lines but for the purposes of the theory, which is developed only in a "narrowband-sense", such distinction disappears. SIR improvement as

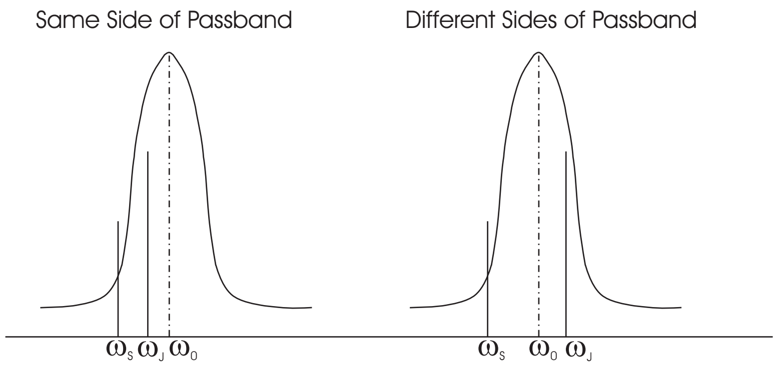

Figure 3.7: Signal and Interferer Scenarios in Relation to the Passband.

a function of proximity and accuracy is presented in Fig. 3.8(a) while Fig. 3.8(b) shows its contours; these are simulated for the case when both ω_S and ω_J are on the same side of the filter's passband. Compared to the second-order filter solution, this approach shows less dependency to the accuracy of interferer tracking, or setting $\omega_B \cong \omega_J$; from the plot a 1% accuracy setting may be sufficient, depending on proximity, to realize 40dB improvement. Figure 3.9 shows fixed (40dB) SIR contours for four Qs considered (Q = 10, 30, 50 and 100). The graph displays the limits placed on what can be achieved: for accurate setting of

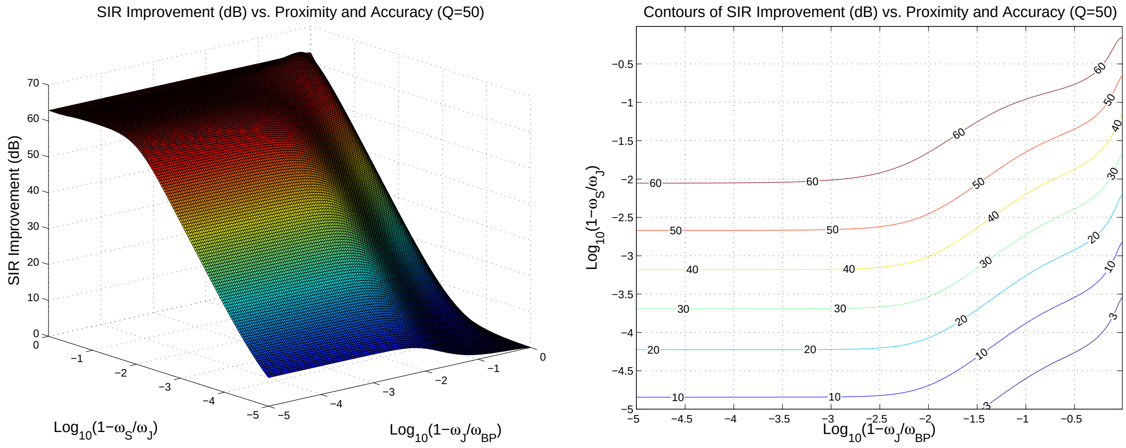

(a) 3D Surface (b) Contours

Figure 3.8: SIR Improvement vs. Proximity and Accuracy (Same-Sides of Passband)

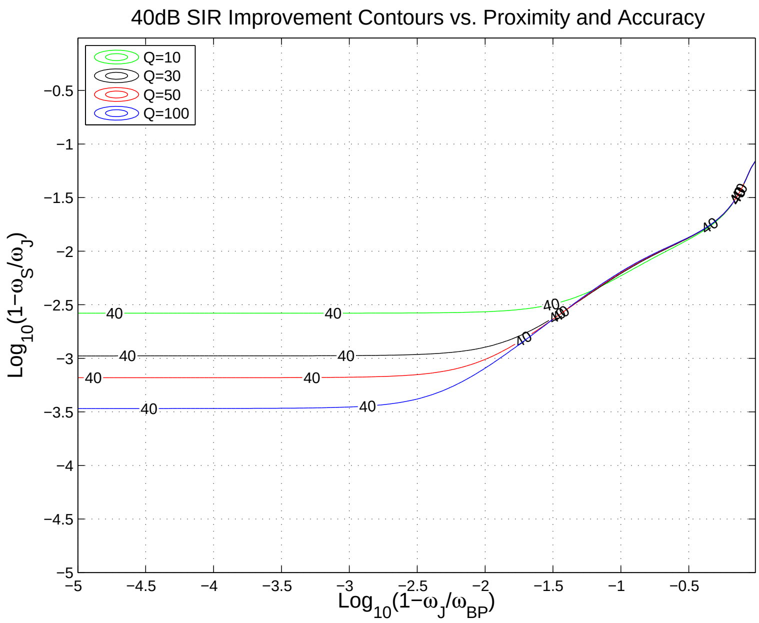

Figure 3.9: 40dB SIR vs. Quality Factor (Same-Sides of Passband)

the bandpass center frequency the limiting factor is proximity; being more selective higher Q filters tolerate interferers very close to the signal (Proximity $\approx 10^{-3.5}$). At low accuracy values all Qs perform similarly.

For the case when the interferer and SOI are on different sides of the passband, SIR as a function of proximity and accuracy is presented in Fig 3.10(a) while Fig. 3.10(b) shows its contours. A sharp jump in SIR is observed along the ridge of equal accuracy

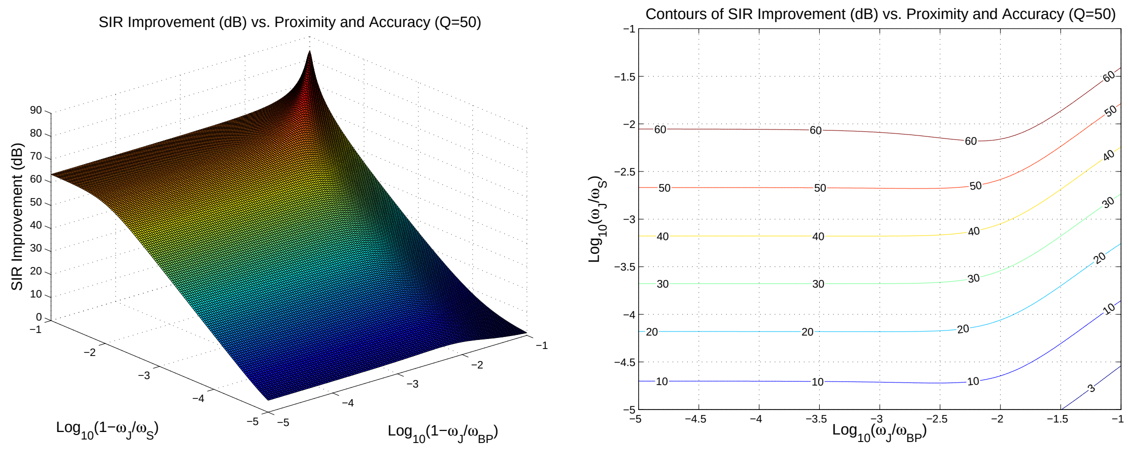

(a) 3D Surface

(b) Contours

Figure 3.10: SIR Improvement vs. Proximity and Accuracy (Different-Sides of Passband)

and proximity. This ridge defines the case when ω_B is set to the signal frequency while maintaining amplitude and phase lock to the interferer. While more optimal in terms of outcome, it is a sensitive solution and difficult to implement. With the noted exception the results are very similar to the same-side scenario.

3.4 Rejection Dependency on Mismatches

SINR improvement is derived as a function of amplitude, $\Delta\alpha$, and phase mismatches, $\Delta\phi$, in the two paths leading to the differential amplifier inputs.

3.4.1 Same Side of the Passband

Simulations arising from the scenario when ω_S and ω_J are on the same side of the filter's passband are conducted with varying proximity levels, where proximity is defined by the following: Proximity $= 1 - Log_{10}\left(\frac{\omega_J}{\omega_S}\right)$. The following cases are considered:

1. ω_S and ω_J are close with Proximity $= 10^{-2}$. SIR Improvement dependence on mismatches $\Delta\alpha$ and $\Delta\phi$ is presented in Fig. 3.11(a) with Fig. 3.11(b) being the contour plot.

2. ω_S and ω_J are further appart with Proximity $= 10^{-0.1}$; SIR Improvement dependence on mismatches $\Delta\alpha$ and $\Delta\phi$ is presented in Fig. 3.12(a) with Fig. 3.12(b) being the contour plot.

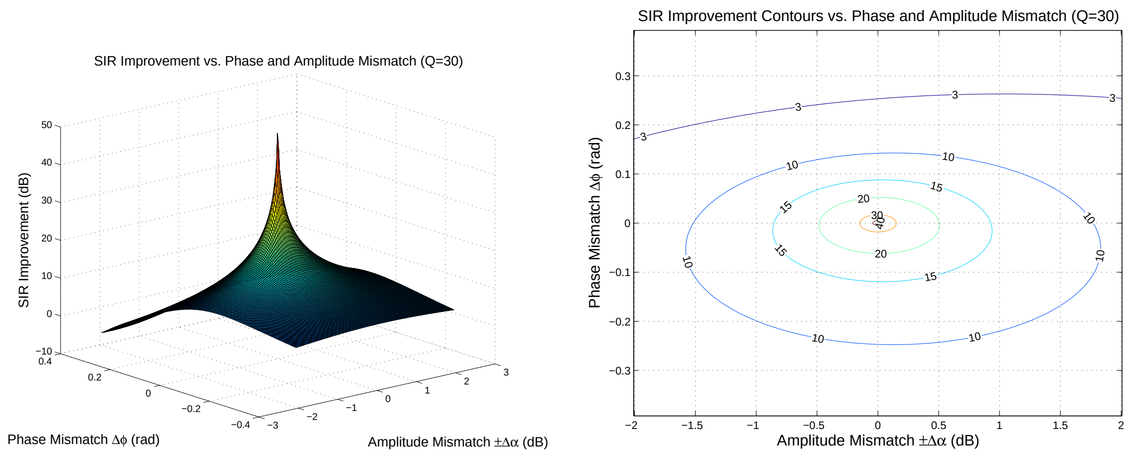

(a) 3D Surface

(b) Contours

Figure 3.11: SIR vs. Mismatches with Proximity $= 10^{-2}$ (Same Sides of Passband)

3.4.2 Different Sides of the Passband

Simulations arising from the scenario when ω_S and ω_J are on different sides of the filter's passband are shown below for the cases:

1. ω_S and ω_J are close with proximity 10^{-2} of between them; SIR Improvement dependence on mismatches $\Delta\alpha$ and $\Delta\phi$ is presented in Fig. 3.13(a) with Fig. 3.13(b) being the contour plot.

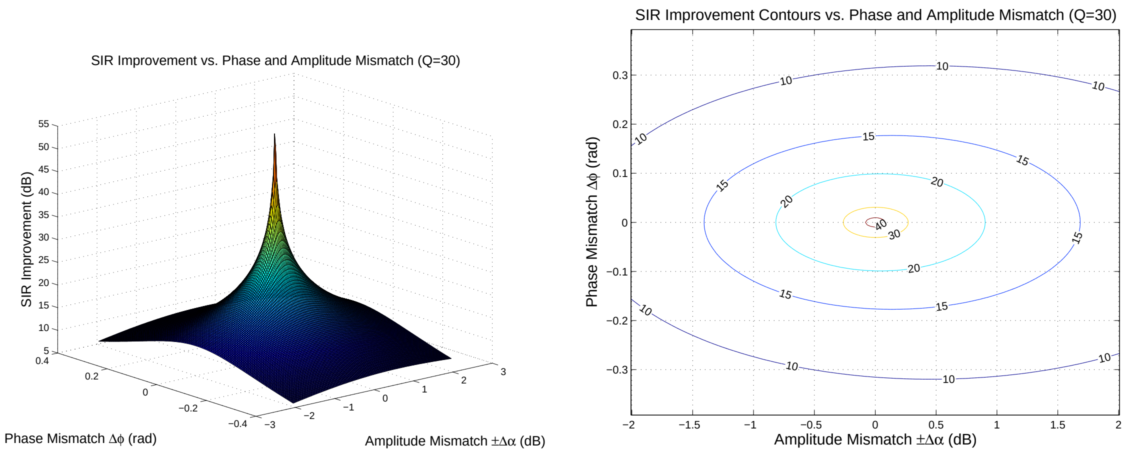

(a) 3D Surface (b) Contours

Figure 3.12: SIR vs. Mismatches with Proximity $= 10^{-0.1}$ (Same Sides of Passband)

2. ω_S and ω_J are further apart with proximity $10^{-0.1}$ of between them; SIR Improvement dependence on mismatches $\Delta\alpha$ and $\Delta\phi$ is presented in Fig. 3.14(a) with Fig. 3.14(b) being the contour plot.

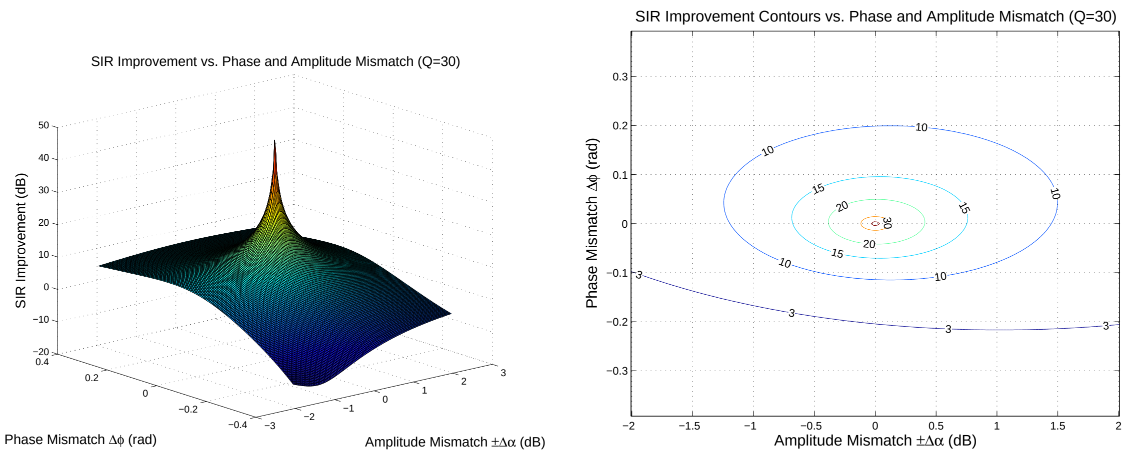

(a) 3D Surface (b) Contours

Figure 3.13: SIR vs. Mismatches with Proximity $= 10^{-2}$ (Different Sides of Passband)

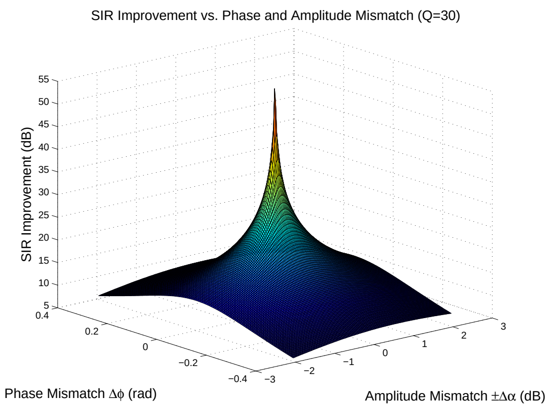

(a) 3D Surface

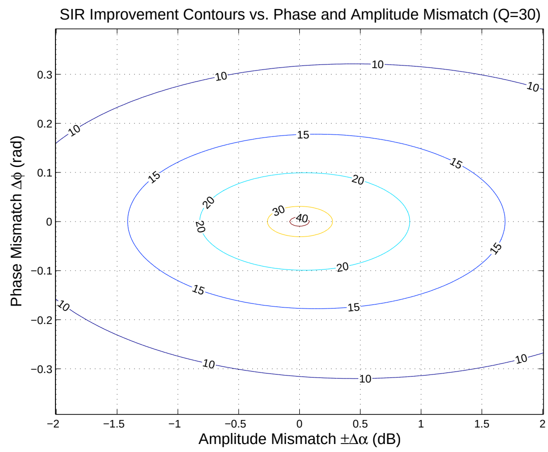

(b) Contours

Figure 3.14: SIR vs. Mismatches with Proximity = $10^{-0.1}$ (Different Sides of Passband)

3.5 Dynamic Range Behavior

The performance of the phase cancellation in terms of dynamic range follows the same procedure as that of the second order notch filter. Figure 3.15(a) shows a plot of SINR improvement contours as a function of noise figure, interferer and input noise power levels for a fixed Q, while Fig. 3.15(b) displays its contours. As channel noise becomes more

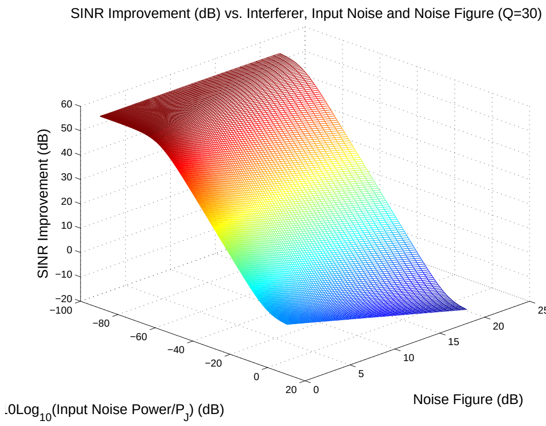

(a) SINR 3D Surface vs. NF, P_J and Noise Power

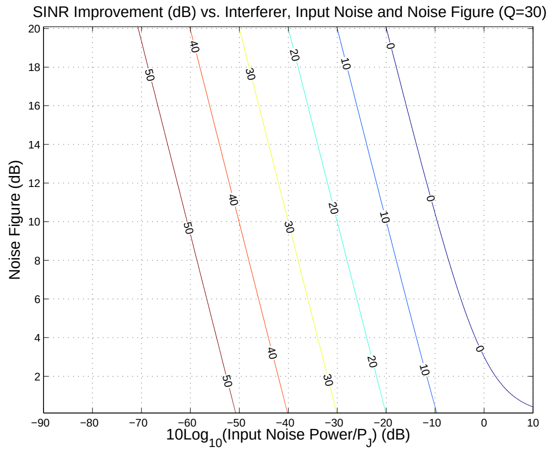

(b) SINR Contours vs. NF, P_J and Noise Power

Figure 3.15: SINR Dynamic Range Plots for $Q = 30$

dominant moving to the right, improvement in SINR is degraded; additionally in order to maintain a targeted improvement both noise figure, design dependent, and input noise power must be under certain values.

3.5.1 Noise Figure of Overall System

For cases when the proposed scheme is implemented to reject high power blockers at a recesiver's front-end then the derivation of the total noise figure (NF) of the system becomes an important system consideration. According to Friis formula for the NF of multiple stages, the first device's gain and NF dominate the total noise figure of the system; the noise factor of a cascaded network [142] with n-stages is calculated by:

$$F_{casc} = F_1 + \frac{F_2 - 1}{G_1} + \frac{F_3 - 1}{G_1 G_2} + \ldots + \frac{F_n - 1}{G_1 G_2 \ldots G_{n-1}} \tag{3.17}$$

with $NF_{casc} = 10Log_{10}(F_{casc})$. The derivation of the system's noise figure here assumes the amplifier has infinite CMRR and hybrids have no mismatches; the impact of finite CMRR and hybrids mismatches on noise figure measurements is considered in 4.3.2. In addition, the procedure followed here mirrors that presented in [78] with appropriate adjustments; first, the uncorrelated noise sources are identified and their powers are summed and second, voltages from uncorrelated noise sources are summed at the output port. The noise factor of the system is then calaculated as:

$$F = \frac{\text{Total Noise at Output Port}}{\text{Noise at Output Port due to Source Resistor}} \tag{3.18}$$

The system model for the purposes of noise figure calculations is presented in Fig. 3.16, below.

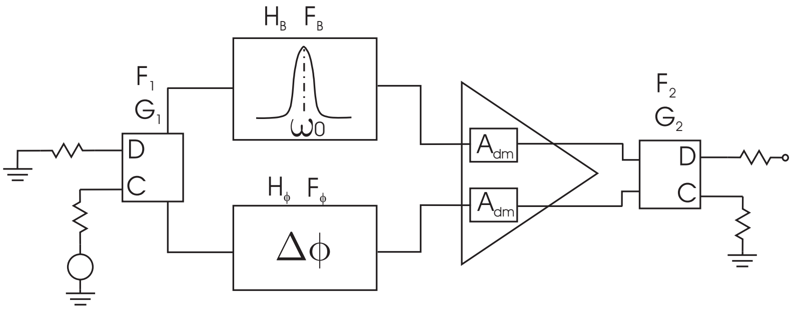

Figure 3.16: NF of Phase Cancellation System with Ideal Diff. Amp.

Uncorrelated Noise Sources

Consider the noise factor and power gain of the input hybrid to be, respectively, F_1 and G_1. The noise power spectral density at port 2, due to input source resistor is kTF_1G_1. This noise power sees "gains" in the filter, the amplifier and output hybrid. Modeling the differential amplifier as two single ended amplifiers with equivalent A_{dm} gains, the upper branch noise power at the output port is:

$$P_{u1} = kTF_1G_1|H_B|^2A_{dm}G_2 \tag{3.19}$$

where, H_B and G_2 are the transfer function of the bandpass and gain of the output hybrid, from port 2 to 1. Similarly, the lower branch noise power at output port, due to input hybrid is:

$$P_{u2} = kTF_1G_1\alpha^2A_{dm}G_2 \tag{3.20}$$

where α is the voltage gain of the phase delay network. The noise powers due to the filter and phase delay network are:

$$P_{u3} = kT|H_B|^2(F_B - 1)A_{dm}G_2 \tag{3.21}$$

$$P_{u4} = kT\alpha^2(F_\phi - 1)A_{dm}G_2 \tag{3.22}$$

where F_B and F_ϕ are the noise factors of the filter and phase delay network. The noise powers due to the amplifier and output hybrid are:

$$P_{u5} = 2kT(F_{dm-1})A_{dm}G_2 \tag{3.23}$$

$$P_{u6} = kTG_2(F_2 - 2) \tag{3.24}$$

Summing all the different contributions, the total uncorrelated noise power at the output port is:

$$\begin{aligned} P_u = kTG_2 \{ & A_{dm}F_1G_1 \left[|H_B|^2 + \alpha^2\right] + \\ & + A_{dm}\left[|H_B|^2(F_B - 1) + \alpha^2(F_\phi - 1) + 2(F_{dm} - 1)\right] + (F_2 - 2)\} \end{aligned} \tag{3.25}$$

Correlated Noise Power

A noise voltage at the input generates two equal magnitude and phase voltages at the outputs of the first hybrid. These voltages are summed in antiphase at the output of the second hybrid. Considering the noise voltage at the input to be $\sqrt{kTR}$ the upper and lower branch noise voltages at the output are, respectively:

$$V_{c1} = H_B\sqrt{kTG_1A_{dm}G_2} \tag{3.26}$$

$$V_{c2} = -\alpha e^{j\phi}\sqrt{kTG_1A_{dm}G_2} \tag{3.27}$$

The total noise voltage at the output is the sum:

$$V_c = \left(H_B - \alpha e^{j\phi}\right)\sqrt{kTG_1A_{dm}G_2} \tag{3.28}$$

Finally total correlated noise power at the output is:

$$P_c = kTG_1A_{dm}G_2|H_B - \alpha e^{j\phi}|^2 \tag{3.29}$$

Total Noise Figure

From definition presented in 3.18, total noise factor of the phase cancellation system is:

$$\begin{aligned} F_T = & \frac{F_1\left[|H_B|^2+\alpha^2\right]}{|H_B-\alpha e^{j\phi}|^2} + \frac{[F_2-2]}{G_1A_{dm}|H_B-\alpha e^{j\phi}|^2} + \\ & + \frac{\left[|H_B|^2(F_B-1)+\alpha^2(F_\phi-1)+2(F_{dm}-1)\right]}{G_1|H_B-\alpha e^{j\phi}|^2} \end{aligned} \tag{3.30}$$

Derivation of the phase cancellation system's NF is corroborated with MATLAB simulations; the total NF of the system is plotted versus amplifier NF and accuracy of filter's center frequency in Fig. 3.17(a) with corresponding contours in Fig. 3.17(b).

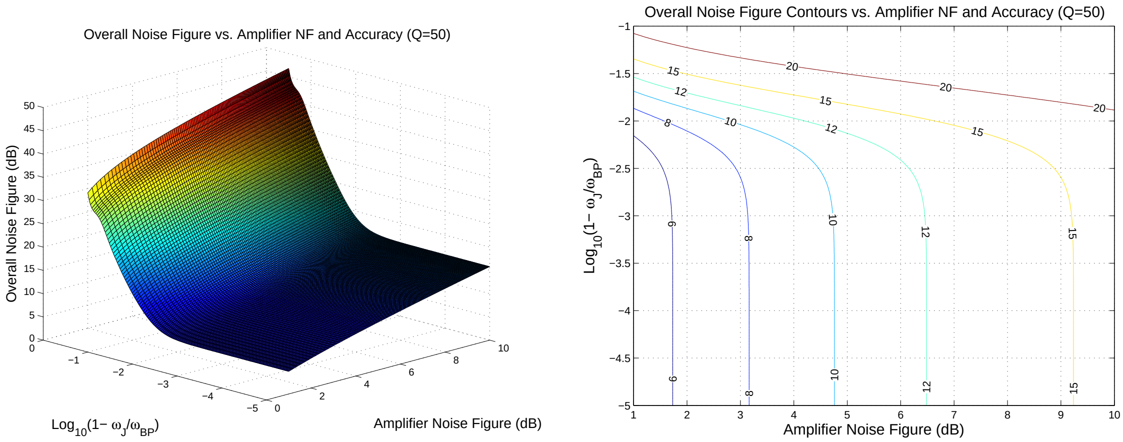

(a) NF 3D Plot vs. Amplifier NF and Accuracy (b) NF Contours vs. Amplifier NF and Accuracy

Figure 3.17: Total System NF vs. Amplifier NF and Accuracy ($CMRR_{AMP} \to \infty$)

The environment setup assumes the following:

- Interferer and SOI are significantly apart (Proximity $= 10^{-0.1}$)
- Amplifier has infinite CMRR
- The filter is lossy with Q=50
- Power splitting and combining is lossless

While the amplifier NF has an important effect on the overall NF of the system, most of the noise figure degradation comes from the fact that nearly half the signal is rejected in the bandpass filter branch. Practical system NF$\approx$ 6dB can be achieved narrowband with low noise amplifiers. Overall NF may degrade further with lower Q filters and lossy phase shifters or time delay networks. One way to minimize losses at the front-end is to utilize multiple or differential antennas.

3.6 Performance Area Exploration

SINR improvement was identified earlier as the figure of merit in determining the effectiveness of the phase cancellation system; the value of such improvement from similar work found from literature review varies depending on the implementation and application, typical measurable values fall in the range of $20-40$dB when implemented in the RF front-end. This work targets 40dB improvement for the entire frequency range when SOI and interferer are sufficiently appart; even for relatively low-Q bandpass filters (Q≈30) this is possible for a 10^{-3} proximity, which means SOI and interferer are 0.1% appart, say 1MHz away in a 1GHz band.

3.6.1 Design Parameter Specifications

Differential amplifier specifications were developed in conjunction with sponsor requirements; from the outset the goal was to design and test a subsystem operating in the 1-3GHz frequency range, which determines the bandwidth of the amplifier. One of the more important design parameters involves the CMRR since it ultimately sets the limit on SINR improvement; targeting 40dB of improvement determines CMRR≥ 40dB. Low noise operation is desired since it affects the dynamic range of the system as shown by Matlab simulations in this chapter. Additionally, high IP3 and good input match are desired; these were chosem to conform with requirements for different communication receivers, such as cellular standards, and generally accepted design performance reported in literature. A summary of design requirements for the LNA are presented in Table 3.1. To test the sys-

Specification	**Value**
Frequency Range	1-3GHz
CMRR	≥40dB
Differential Voltage Gain (s_{21}^{dd})	≥20dB
Differential Input Match (s_{11}^{dd})	≤-10dB
NF	≤5dB
OIP3	≥0dBm
Power Consumption	≤50mW
Stability	Unconditionally Stable

Table 3.1: Differential LNA Design Specifications.

tem functionality of the LNA several key peripheral devices are identified:

1. Bandpass Filter
2. Variable Attenuator
3. Variable Phase Shifter
4. Hybrid

High Q tunable bandpass filters are desired in terms of overall system performance, however, they require low dissipation factor ($\tan\delta$) for the pcb material. To circumvent higher manufacturing costs two bandpass filter designs are chosen:

1. High Q, fixed-frequency bandpass
2. Tunable bandpass

Their specifications are presented in Table 3.2 and 3.3, below.

Specification	**Value**
Center Frequency	$\approx$ 1.5GHz
Quality Factor	$\geq$30
Input Match (s_{11})	$\leq$-10dB
Insertion Loss	$\leq$3dB

Table 3.2: Fixed Frequency Bandpass Specifications.

To match the amplitudes of the interfering tones at the input of the differential amplifier demands use of variable attenuators that have to cover the entire frequency range. From the mismatch plots fine resolution is desired for amplitude tuning to find maximum CMRR of the system; variable attenuators with better than 0.1dB amplitude resolution should suffice. Specifications for the variable attenuators are presented in Table 3.4, below.
Matching the phases of the interfering tones at the input of the differential amplifier demands use of variable phase shifters that are broadband capable of up to 180° phase shift range.

Specification	**Value**
Center Frequency	$\approx$ 1GHz
Tunable Frequency Range	$\gtrapprox$ 30%
Quality Factor	$\geq$30
Input Match (s_{11})	$\leq$-10dB

Table 3.3: Tunable Bandpass Specifications.

Specification	**Value**
Frequency Range	1-3GHz
Minimum Attenuation Range	0-16dB
Minimum Required Attenuation Resolution	0.1dB
Input Match (s_{11})	$\leq$-8dB
Insertion Loss	$\leq$3dB

Table 3.4: Variable Attenuator Specifications.

Fine resolution is desired for phase tuning to find maximum CMRR of the system; variable phase shifters with better than 0.1°phase resolution should suffice. Specifications for the variable phase shifters are presented in Table 3.5, below.

Specification	**Value**
Frequency Range	1-3GHz
Minimum Phase Shift Range	0-180°
Minimum Required Phase Resolution	0.1°
Input Match (s_{11})	$\leq$-8dB
Insertion Loss	$\leq$3dB

Table 3.5: Variable Phase Shifter Specifications.

Chapter 4

Literature Review

This chapter conducts a literature review of port network theory, s-parameters, noise figure and nonlinear modeling; these concepts are incorporated in the design and testing of the components that comprise the proposed interference improvement technique.

4.1 S-Parameter Predictions

The scattering parameters for an n-port network are defined in terms of the respective normalized incident, a_n, and reflected, b_n, power waves with:

$$\mathrm{a_n} = \frac{\mathrm{V_n + I_n Z_n}}{2\sqrt{\mathrm{Re(Z_n)}}} \tag{4.1}$$

and

$$\mathrm{b_n} = \frac{\mathrm{V_n\text{-}I_n Z_n^*}}{2\sqrt{Re(Z_n)}} \tag{4.2}$$

where V_n and I_n are the voltage and current present at the n^{th} port and Z_n refers to the characteristic impedance of the port. The scattering matrix for a two port network (depicted in Fig. 4.1) is defined by:

$$\begin{pmatrix} b_1 \\ b_2 \end{pmatrix} = \begin{bmatrix} S_{11} & S_{12} \\ S_{21} & S_{22} \end{bmatrix} \begin{pmatrix} a_1 \\ a_2 \end{pmatrix} \tag{4.3}$$

where S_{11}, S_{22} are respectively the input and output return loss and S_{21}, S_{12} the forward voltage gain and reverse isolation.

Figure 4.1: Scattering parameters for a two port network.

4.1.1 Mixed-Mode S-Parameters

Since differential circuits respond to both common-mode (CM) and differential-mode (DM) stimuli, the scattering matrix that describes a differential two-port network (depicted in Fig. 4.2) involves common-mode and differential-mode responses, as well as, any mode conversions that may occur. The corresponding s-parameters are referred to as mixed mode s-parameters [96], the definition and derivation of which along with related concepts can be found in the literature [97] or [98]. According to [96] the mixed-mode s-parameter matrix

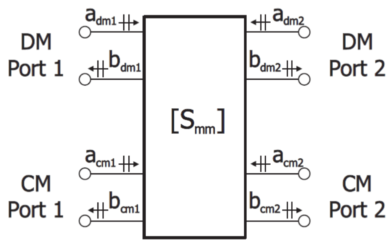

Figure 4.2: Scattering parameters for a four port network.

can be separated into four 2×2 quadrants:

$$\begin{bmatrix} b_{dm1} \\ b_{dm2} \\ b_{cm1} \\ b_{cm2} \end{bmatrix} = \begin{bmatrix} [\mathbf{S}_{dd}] & [\mathbf{S}_{dc}] \\ [\mathbf{S}_{cd}] & [\mathbf{S}_{cc}] \end{bmatrix} \begin{bmatrix} a_{dm1} \\ a_{dm2} \\ a_{cm1} \\ a_{cm2} \end{bmatrix} \tag{4.4}$$

where $\mathbf{S}_{dd}$, $\mathbf{S}_{cc}$ refer to the differential and common-mode s-parameters, $\mathbf{S}_{dc}$ and $\mathbf{S}_{cd}$ refer to differential-to-common mode and common mode-to-differential conversions. Mixed-mode s-parameters for a differential two-port network can be related to the standard s-parameters of a four-port network by the following similarity transformation [97]:

$$\mathbf{S}_{mm} = \mathbf{M}\mathbf{S}_{std}\mathbf{M}^{-1} \tag{4.5}$$

where $\mathbf{S}_{mm}$, $\mathbf{S}_{std}$ are respectively the mixed-mode s-parameters and the standard four-port s-parameters and:

$$\mathbf{M} = \frac{1}{\sqrt{2}} \begin{bmatrix} 1 & -1 & 0 & 0 \\ 0 & 0 & 1 & -1 \\ 1 & 1 & 0 & 0 \\ 0 & 0 & 1 & 1 \end{bmatrix} \tag{4.6}$$

By taking independent, single-ended s-parameter measurements on all four ports, equation 4.6 provides a basis for obtaining $\mathbf{S}_{MM}$ from $\mathbf{S}_{std}$. In addition, $\mathbf{S}_{MM}$ can be directly measured by providing separate stimuli for each mode. Three techniques are identified for characterizing the operation of a differential device:

1. Use a two port network analyzer (NA) and baluns/hybrids to provide differential and common-mode signals. Broadband hybrids must be chose and their insertion loss for different modes must be accounted for the frequency range of interest; accuracy may degrade due to mismatches between probe tips, cables and hybrids.

2. Employ a pure mode vector network analyzer (PMVNA), which generates differential and common-mode stimuli. This is the most accurate method for measuring mixed-mode s-parameters and generally the most expensive.

3. Use multiport VNAs to make single ended measurements at each port and convert them to mixed mode s-parameters by the similarity transformation previously mentioned; the associated linearity assumption and therefore superposition hold for small-signal s-parameters. There is more accrued error when measuring mode conversions with this method [99].

4.1.2 Stability of mixed mode designs

An important issue in dealing with active RF circuits is the stability of the design and commonly used stability analysis considers the Rollet factor:

$$K = \frac{1 - |S_{11}|^2 - |S_{22}|^2 + \Delta_S}{2|S_{12}| - |S_{21}|} > 1 \tag{4.7}$$

and either of the following auxiliary conditions [137], [143]:

$$\Delta_S = |S_{11}S_{22} - S_{21}S_{12}| < 1 \tag{4.8}$$

$$B = 1 + |S_{11}|^2 - |S_{22}|^2 - |S_{11}^*S_{22} - S_{21}S_{12}^*|^2 > 0 \tag{4.9}$$

in order to satisfy unconditional stability for all frequencies; typically, frequencies up to the F_t of the transistor are considered. Another derivative of the Rollet's stability conditions is the geometric stability factor [139], μ, which can be applied either towards the source or the load:

$$\mu_{source} = \frac{1 - |S_{11}|^2}{|S_{22} - \Delta_S(S_{11}^*)| + |S_{21}S_{12}|} \geq 1 \tag{4.10}$$

$$\mu_{source} = \frac{1 - |S_{22}|^2}{|S_{11} - \Delta_S(S_{22}^*)| + |S_{21}S_{12}|} \geq 1 \tag{4.11}$$

In several published works, an analogous situation has been reported in power amplifiers with the existence of additional modes in the internal nodes of the circuits, which are not visible to the outside stimuli. Even and odd-mode stability analysis [141] involves breaking up connections and inserting additional stimuli between internal nodes. Such analysis is not necessary here since differential and common modes are externally injected and therefore Rollett's conditions will be considered for both. In addition, parametric oscillations rising from the existence (or movement) of poles in the right-hand plane (RHP) [140] are not considered since the amplifier operates under linear conditions and not significant compression.

4.1.3 Coupled Transmission Line Filters

Combline filters form LC resonating structures via transmission-line elements and termination capacitors. The general idea of a combline filter is depicted in Fig. 4.3 [146]. The transmission line sections are chosen a particular electric length, θ_0, at the resonating

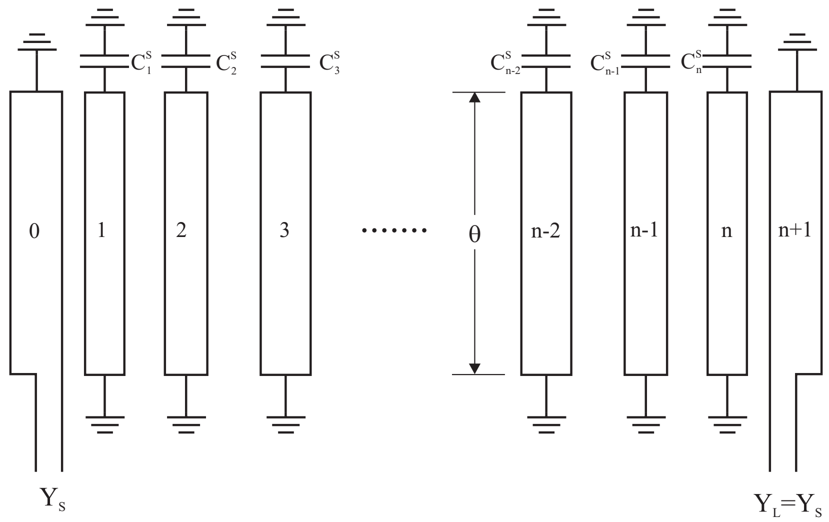

Figure 4.3: Multi Section Combline Filter

frequency, f_0, and terminated into their respective capacitances, C_n^S. In order to maximize the inductance of the transmission line, a nominal choice for length is $L = \lambda_0/8$, where $\lambda_0 = c/(f_0\sqrt{\epsilon_{eff}})$ with c being the speed of light in vacuum and ϵ_{eff} the effective permittivity of the dielectric medium.

The design equations start with the standard 50Ω choice for all port impedances, $Z_k = 50$, and corresponding admittances, $Y_k = 1/Z_k$; here the subscript k denotes the index of the resonating element. The lumped capacitances are then:

$$C_{lump(k)} = \frac{Y_k \cot\theta_0}{\omega_0} \tag{4.12}$$

where, $\theta_0 = 2\pi L/\lambda_0$ and $\omega_0 = 2\pi f_0$. The inverter elements are calculated by:

$$B_k = Y_k \frac{\cot\theta_0 + \theta_0(\csc\theta_0)^2}{2} \tag{4.13}$$

$$J_{kk} = w\sqrt{\frac{B_{k+1}B_k}{g_{k+1}g_k}} \tag{4.14}$$

where, $w = \dfrac{f_0}{BW_{3dB}}$ is the 3dB percent bandwidth and g_k the normalized filter coefficients; such coefficients are typically found in filter cookbooks for a given number of reactive elements and desired passband ripple, bandwidth, stopband rejection etc.

For an n element filter, the mutual admittances can then be calculated by:

$$Y_{01} = \frac{wB_1}{g_0 g_1} \tag{4.15}$$

$$Y_{n,n+1} = \frac{wB_n}{g_n g_{n+1}} \tag{4.16}$$

$$Y_{kk} = J_{kk} \tan\theta_0 \tag{4.17}$$

where, g_0, g_{n+1} denote the normalized filter coefficients of the input, output feed lines, which for symmetrical filters with odd-number of sections are $g_0 = g_{n+1} = 1$. Subsequently, the normalized self-capacitances per unit length of the lines are calculated by:

$$\frac{C_0}{\epsilon} = \frac{377Y_0\left(1-\sqrt{\frac{Y_{01}}{Y_0}}\right)}{\sqrt{\epsilon_{eff}}} \tag{4.18}$$

$$\frac{C_1}{\epsilon} = \frac{377Y_1\left[\left(\frac{Y_{01}}{Y_1}\right)-\left(\frac{J_{11}}{Y_1}\right)\tan\theta_0\right]}{\sqrt{\epsilon_{eff}}} + \frac{C_0}{\epsilon} \tag{4.19}$$

$$\frac{C_k}{\epsilon} = \frac{377Y_k\left[1-\frac{J_{(kk)-1}}{Y_k}\tan\theta_0-\frac{J_{kk}}{Y_k}\tan\theta_0\right]}{\sqrt{\epsilon_{eff}}} \tag{4.20}$$

$$\frac{C_n}{\epsilon} = \frac{377Y_n\left[\frac{Y_{n,n+1}}{Y_n}-\frac{J_{(nn)-1}}{Y_n}\tan\theta_0\right]}{\sqrt{\epsilon_{eff}}} + \frac{C_{n+1}}{\epsilon} \tag{4.21}$$

$$\frac{C_{n+1}}{\epsilon} = \frac{377Y_{n+1}\left[1-\sqrt{\frac{Y_{n,n+1}}{Y_{n+1}}}\right]}{\sqrt{\epsilon_{eff}}} \tag{4.22}$$

and in similar fashion the mutual capacitances per unit length are:

$$\frac{C_{01}}{\epsilon} = \frac{377Y_0}{\sqrt{\epsilon_{eff}}} - \frac{C_0}{\epsilon} \tag{4.23}$$

$$\frac{C_{kk}}{\epsilon} = \frac{377Y_k\left[\frac{J_{kk}}{Y_k}\tan\theta_0\right]}{\sqrt{\epsilon_{eff}}} \tag{4.24}$$

$$\frac{C_{nn}}{\epsilon} = \frac{377Y_n}{\sqrt{\epsilon_{eff}}} - \frac{C_{n+1}}{\epsilon} \tag{4.25}$$

Depending on the needs and capabilities, the designer has the freedom to take the calculated filter parameters and implement it in a technology of choice, such as microstrip, stripline, waveguide etc. In computing the physical parameters of the coupled transmission lines, such as widths or spacings, one can make use of the Getsinger's chart [147], [145].

4.1.4 Dielectric Filters

The dielectric filter technology is based on high dielectric constant ceramic material, such as crystal rutile (TiO_2). Mainly used in mobile communications, it has contributed to the lower cost and size of such devices since they can easily be miniaturized for use at lower microwave frequencies. Pure rutile has a very high dielectric constant, typically on the order of $K \sim 100$ for perpendicular polarization and $K \sim 200$ for parallel polarization [152], while exhibiting very low dielectric losses, $tan\delta \sim 10^{-4}$ [152]. This makes it possible to achieve unloaded Q factors on the order of several thousands at room temperature and 10^5 at liquid helium temperature [156]. High unloaded $Q \sim 100$ resonators [153] have been obtained with high dielectric constant materials, $\epsilon_r \sim 80$, which allows constructions of compact filters; typically, such filters utilize metal walls to provide shielding [154]. The inherent drawback of high ϵ_r resonators is the dependence of the dielectric constant and therefore the resonant frequency on temperature; thermal stabilization can remedy such dependence [154]. Advancements in dielectric filter manufacturing have enabled users to purchase commercial off-the-shelf parts at relatively low prices.

4.1.5 Variable Phase Shifter

Continually-variable phase can be obtained when using a 90° coupler with voltage-variable loads [161], [160]; the variable loads can be realized with varactor diodes, or transistor switches in the case of digital phase shifters. This is commonly referred to as a reflection-type phase shifter [159] with the general idea depicted in Fig. 4.4; the design utilizes a branchline coupler but Lange and rat-race couplers are also popular.

In Fig. 4.4, the RF signal enters the incident port, which produces voltage waves at the direct and coupled ports with 90° difference between the two; Z_S and Z_L denote the incident and isolated port impedances, respectively. These waves are subsequently reflected according to the load terminations; in the case of lossless, highly-reflective loads, such as an ideal open or short, all of the energy is reflected towards the incident and isolated ports. Assuming an ideal quadrature coupler with high directivity, there is perfect cancellation of the travelling wave vectors at the incident port and perfect summation at the isolated port.

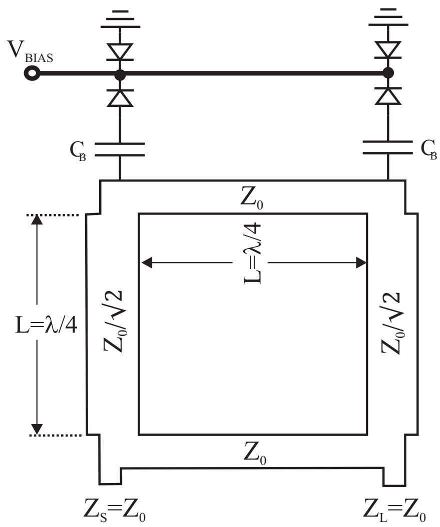

Figure 4.4: Topology of the Reflection Type Phase Shifter

Hence, all of the energy is transferred to the isolated (output) port. The relative phase shift between the input and output voltage waves changes as the reflective terminations are varied. By employing varactor diodes as reflective loads, the load capacitance and consequently the phase shift of the transmission coefficient can be varied in a continuous manner with reverse bias voltage.

In reference [161], continually variable 180° phase shift has been simulated $\approx 5-25$GHz by using multi-section Lange couplers and varactor diodes. In [160], continually variable 360° has been obtained $\approx 16-18$GHz by cascading three MMICs that utilize a branchline coupler design. Nonlinearity impact of varactor diodes on the performance of reflection-type phase shifters have been studied in [162] and with hyperabrupt junction diodes in reference [164]; impedance requirements for matching the diode's reactance to a tangent function have been proposed. High linearity and 30° phase shift has been obtained at 1GHz by the use of a time-delay line with anti-series and anti-parallel diodes [163].

4.2 Nonlinear Predictions

Methods for analyzing the nonlinear behavior of a circuit have evolved over the years and a short summary of strengths and weaknesses is included in this section.

4.2.1 Power Series Representation

Nonlinear components, such as harmonics and other mixing products, are generated due to the nonlinear I-V relationship of active devices, such as transistors or diodes. The nonlinear I-V relationship model can be considered as a power series representation:

$$i(t) = \sum_{n=1}^{N} a_n v^n(t) \tag{4.26}$$

where the current $i(t)$ is represented as a linear combination of different powers of the driving voltage, $v(t)$, each scaled by the corresponding coefficient, a_n. If the driving voltage comprises of a single frequency then the nonlinear relationship predicts many harmonics of the fundamental are generated. If the input voltage, $v_{in}(t)$, comprises of two or more tones, intermodulation products appear, in addition, at the output. For example, lets assume that the input consists of two tones at nearby frequencies ω_1 and ω_2 with equal amplitudes:

$$v_{in}(t) = A\cos(\omega_1 t) + A\cos(\omega_2 t) \tag{4.27}$$

Furthermore, assuming a linear relationship between output current, $i_o(t)$, and output voltage, $v_o(t)$, yields:

$$i_o(t) \cdot Z_o = v_o(t) = Z_o\left(a_1 v_{in} + a_2 v_{in}^2 + a_3 v_{in}^3 + \ldots\right) \tag{4.28}$$

where the output impedance, Z_o, is linear and the DC component is not shown. Ignoring higher-order powers the output voltage due to the two tones can be written as:

$$\begin{aligned} v_o(t) \quad = \quad & Z_o\Big\{a_1 A\left[\cos\left(\omega_1 t\right) + \cos\left(\omega_2 t\right)\right] + a_2 A^2\left[\cos\left(\omega_1 t\right) + \cos\left(\omega_2 t\right)\right]^2 + \\ & + a_3 A^3\left[\cos\left(\omega_1 t\right) + \cos\left(\omega_2 t\right)\right]^3\Big\} \end{aligned} \tag{4.29}$$

Expanding the polynomials and using trigonometric identities the output becomes:

$$\begin{aligned} v_o(t) \quad = \quad & Z_o \Big\{ a_1 A \left[\cos\left(\omega_1 t\right) + \cos\left(\omega_2 t\right)\right] + \frac{a_2 A^2}{2} \left[\cos(2\omega_1 t) + \cos(2\omega_2 t)\right] + \\ & + a_2 A^2 + a_2 A^2 \Big[\cos\Big((\omega_1 + \omega_2)t\Big) + \cos\Big((\omega_1 - \omega_2)t\Big)\Big] + \\ & + \frac{9 a_3 A^3}{4} \left[\cos(\omega_1 t) + \cos(\omega_2 t)\right] + \frac{a_3 A^3}{4} \left[\cos(3\omega_1 t) + \cos(3\omega_2 t)\right] + \\ & + \frac{3 a_3 A^3}{4} \Big[\cos\Big((2\omega_1 + \omega_2)t\Big) + \cos\Big((\omega_1 + 2\omega_2)t\Big)\Big] \\ & + \frac{3 a_3 A^3}{4} \Big[\cos\Big((2\omega_1 - \omega_2)t\Big) + \cos\Big((2\omega_2 - \omega_1)t\Big)\Big] \Big\} \end{aligned} \tag{4.30}$$

A simplified depiction of the resulting spectrum was shown in Fig. 2.3 on page 6. For balanced designs, third-order intermodulation products are usually the most problematic since they are located very close to the frequencies of interest and rise 3dB for every 1dB increase in fundamental tone; this relationship generally holds in the weak nonlinear region (no significant compression). Specifications used as measures of a devices nonlinear behavior are the second-order intercept point, or IP2, and the third-order intercept point, or IP3. IP2 is the power level where the linear and second-order lines intersect and IP3 is the power level where the linear and third-order lines intersect; these are purely mathematical extrapolations as the actual gain curve will start to compress at much lower input power levels. Gain compression is often characterized by the 1dB point, which measures the power level (input or output) where the gain is 1dB lower than the extrapolated linear line; this is depicted in Fig. 4.5. For most processes and amplifier designs, the relationship between 1dB compression and third order intercepts can be approximated by: $\mathrm{P_{1dB}} - \mathrm{IP3} \approx -10\mathrm{dB}$ [130]. Following the power series analysis example, above, the intercept points (output-referred) are [82]:

$$\mathrm{OIP2(dBm)} = 10 \log_{10}\left(\frac{Z_o}{2} \frac{a_1^4}{a_2^2}\right) + 30 \tag{4.31}$$

$$\mathrm{OIP3(dBm)} = 10 \log_{10}\left(\frac{2Z_o}{3} \frac{a_1^3}{a_3}\right) + 30 \tag{4.32}$$

Albeit simple to conceptualize, the power series failure to address the frequency dependence of transistor distortion is its inherent drawback; such weakness can be cicumvented by using

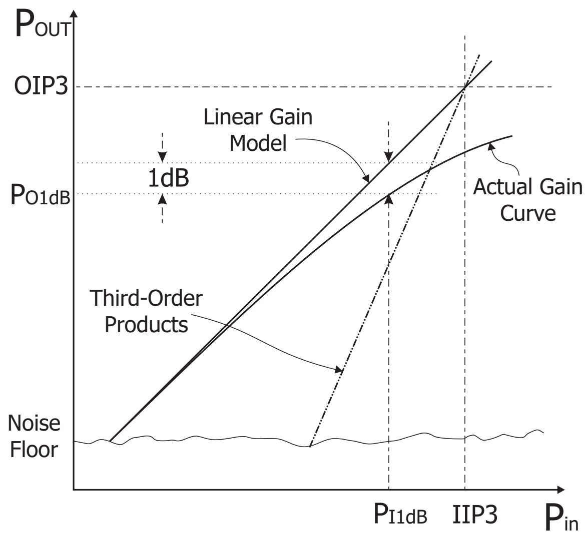

Figure 4.5: Gain Compression and Third Order Intercept Point

a Volterra series representation, which is in fact a generalization of the power series, one that includes memory effects. The theory of nonlinear analysis via Volterra series was pioneered by Wiener [83] and further developed by Bose [84], applied to transistor circuit analysis [90] and later to MESFET circuits [91]. The popularity of the method has waned over the years due to several reasons. First, the method is used primarily to describe weak-nonlinearities by use of Volterra kernels; whenever higher order kernels are necessary, such as in the case of hard-nonlinearities, the method has difficulty converging. Second, it can't be used to determine the stability of a nonlinear network and it is difficult to transform its representation to the time domain [90].

4.2.2 Advanced Nonlinear Analysis Tools

Contemporary nonlinear analysis tools can be divided into two major subgroups: harmonic balance and shooting methods.

Shooting Methods

Shooting methods employ iterative procedures for solving boundary value problems. They are typically subdivided into periodic and quasi-periodic steady-state analyses. Periodic analyses first compute the large signal operating point about which the behavior of the circuit is linearized. The fundamental equation considers the fact that a circuit driven with stimulus of period T, will satisfy the following time-domain equation when steady-state is reached [94]:

$$f(t_0 + T) = f(t_0) \tag{4.33}$$

Mixed frequency-time domain analyses can accomodate two large sinusoid stimuli in calculating a quasi-periodic steady state, one in which a large signal acts a high frequency carrier and the other as a low frequency envelope; small signal analyses are subsequently performed around this quasi-periodic operating point. In solving the ensuing nonlinear equations periodic or quasi-periodic analyses typically employ a Newton iteration.

Since shooting methods are formulated in the time domain, they have an inherent difficulty in handling distributed elements such as transmission lines; such elements in theory require an infinite number of lumped elements to correctly represent them. In general, shooting methods are best suited for analyzing hard-nonlinear networks, such as switched-capacitor circuits, oscillators or power converters [93].

Harmonic Balance

Harmonic balance is a nonlinear analysis tool that directly computes the steady-state solution of a nonlinear differential equation. It describes nonlinear components, like transistors or diodes, in the time domain and linear components, like transmission lines, in the frequency domain; here the term Harmonic Balance is differentiated from Spectral Balance, which only uses a frequency domain formulation [89]. The method subdivides a circuit into nonlinear and linear parts and applies the Kirchhoff current laws at the corresponding nodes. Procedures that equate the current values from the linear and nonlinear parts are implemented and iteratively solved. Since Fourier transforms are required for the frequency domain formulation of nonlinear elements, sufficient number of harmonics and mixing products can ensure convergence but also demand more computational resources. Harmonic Balance is most efficient for weak-nonlinearities but can also be applied to hard-nonlinear circuits, such as compressed power amps. Since linear elements are described in the frequency domain, it can easily incorporate distributed components. The method has the most difficulty with networks that generate incommensurate frequency components, like oscillators or switched capacitor circuits.

4.3 Noise Figure Analysis and Measurement

The spot noise factor (F) at a specified frequency is defined as the ratio of the total output noise power per unit bandwidth available at the output port to the portion due to the source termination at the standard temperature T_0 [75].

$$F = \frac{P_{no}}{G_a(f)kT_0} \tag{4.34}$$

where P_{no} is the total output noise power, $G_a(f)$ is the available power gain of the device and kT_0 is the noise power due to the source resistor at temperature T_0. The spot noise figure (NF) is the dB representation of the noise factor:

$$\mathrm{NF} = 10 \times \log_{10}(F) \tag{4.35}$$

Equivalently, the noise figure indicates the degradation of the signal-to-noise ratio [74]:

$$\mathrm{NF} = 10 \times \log_{10}\left\{\frac{S_i/N_i}{S_o/N_o}\right\} \tag{4.36}$$

where S_i/N_i and S_o/N_o are the input and output signal to noise ratios at the input and output, respectively. The noise figure of a circuit can be optimized by careful selection of the source impedance resulting in the minimum noise figure, NF_{min}, attainable. The process, often referred to as noise matching, does not, in general, coincide with choosing an input impedance that provides maximum power gain. This corresponds to one of the trade-offs between maximum power gain, input return loss and $\mathrm{NF_{min}}$ designs in low noise applications. For a two port network, noise figure can be expressed in terms of $\mathrm{NF_{min}}$ and terminating conditions by the following:

$$F = F_{min} + \frac{G_n}{R_S}|Z_S - Z_{opt}|^2 \tag{4.37}$$

where, F is the actual noise factor, F_{min} the minimum noise factor, G_n is the equivalent noise conductance of the device, R_S the source resistance, Z_S the impedance of the device and Z_{opt} the optimum source impedance that provides minimum noise figure.

4.3.1 Noise Figure Measurement

The following techniques can be used for evaluating the noise figure of a two-port network:

1. Noise Figure meter
2. The Gain method
3. The Y-factor method

Table 4.1 lists a summary of advantages and disadvantages for each technique. Anticipating a $3-5$dB NF, accurate measurements can be achieved with either an NF meter or Y-factor Method.

Method	Application	Advantage	Disadvantage
NF Meter	Measuring wide range of NF values	Accurate for low NF; easy setup	Expensive equipment
Gain	High NF characterization	Accurate for high NF; Broadband	Poor accuracy for low gain or NF
Y-Factor	Measuring wide range of NF values	Wide range; Gain independent; Broadband	Poor accuracy for high NF

Table 4.1: Summary of Pros and Cons of Different NF Measurement Techniques.

The Y-factor method is the most common technique for measuring NF, whether applied manually or automatically by a noise figure analyzer; the noise figure is calculated by measuring the difference in power spectral density when the noise source is on and when it is off:

$$\mathrm{NF} = 10 \times \log_{10}\left\{\frac{10^{\frac{\mathrm{ENR_{dB}}}{10}}}{10^{\frac{\mathrm{Y_{dB}}}{10}} - 1}\right\} \tag{4.38}$$

where $\mathrm{ENR_{dB}}$ is the excess noise ratio (in dB), specified for the noise source and Y_{dB} is the dB difference in power spectral density when the noise source is on and when it is off.

Mathematical definitions are as follows:

$$\mathrm{ENR} = \frac{T_S^{ON} - T_S^{OFF}}{T_0} \tag{4.39}$$

$$Y = \frac{P_N^{ON}}{P_N^{OFF}} \tag{4.40}$$

where T_S^{ON}, T_S^{OFF}, T_0, P_N^{ON} and P_N^{OFF} are respectively the noise temperature of the source when its on, noise temperature of the source when its off, reference temperature (usually 290K), noise power with the source on and with the source off. Noise temperature is defined as the equivalent temperature that generates the same thermal noise power as the one added by the DUT. One would measure P_N^{ON} and P_N^{OFF} multiple times by switching the noise source on and off to obtain an average value for the noise figure. Calibration can correct for cases when T_S^{OFF} differs from T_0.

4.3.2 Differential Noise Figure Measurement Error

Prior work has focused on differential NF characterization techniques using differential stimuli [78] or extraction from single ended measurements [79]. There is a lack, however, in quantifying and predicting measurement errors due to offsets. While such errors can arise from many sources such as unbalanced inputs or finite CMRR of the amplifier, it would be beneficial to attach a number to the level of confidence in making such measurements. This work first considers an ideal amplifier (i.e. CMRR $\rightarrow \infty$) with unbalanced inputs and then a finite CMRR amplifier with unbalanced inputs. These scenarios are depicted in Fig. 4.6 below. It is also important to keep in mind that mismatches in these analyses represent noiseless imbalances.

Ideal Differential Amplifier

Following the same procedure as in Section 3.5.1, both uncorrelated and correlated noise sources are identified and their total noise contributions summed; noise factor is then calculated according to equation 3.18. The uncorrelated noise sources are represented by the noise introduced by the hybrids and the amplifier; while the source resistor generates correlated noise voltages at the output. The noise powers introduced by the input hybrid

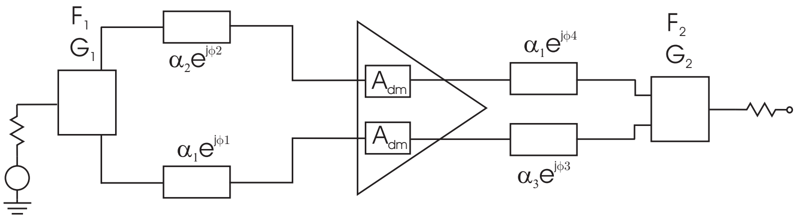

Figure 4.6: Mismatches in Differential NF Measurement with Ideal Diff. Amp.

at the lower and upper branches are, respectively, at the output:

$$P_{u1} = kTF_1G_1\alpha_2^2A_{dm}\alpha_4^2G_2 \tag{4.41}$$

$$P_{u2} = kTF_1G_1\alpha_1^2A_{dm}\alpha_3^2G_2 \tag{4.42}$$

The noise powers from the differential amplifier and output hybrid are, respectively:

$$P_{u3} = kTA_{dm}\left(F_{dm}-1\right)G_2\left(\alpha_4^2\alpha_3^2\right) \tag{4.43}$$

$$P_{u4} = kT\left(F_2-2\right)G_2 \tag{4.44}$$

The total noise power from uncorrelated sources is therefore:

$$P_u = kTG_2\left[F_1G_1A_{dm}\left(\alpha_2^2\alpha_4^2+\alpha_1^2\alpha_3^2\right)+\left(F_{dm}-1\right)\left(\alpha_4^2+\alpha_3^2\right)+\left(F_2-2\right)\right] \tag{4.45}$$

With the source resistor being the only correlated noise source, the upper and lower branch noise voltages at the output are, respectively:

$$V_{c1} = \sqrt{kTRG_1A_{dm}G_2}\alpha_2e^{j\phi_2}\alpha_4e^{j\phi_4} \tag{4.46}$$

$$V_{c2} = \sqrt{kTRG_1A_{dm}G_2}\alpha_1e^{j\phi_1}\alpha_3e^{j\phi_3} \tag{4.47}$$

When these voltages are added they produce an equivalent noise power:

$$P_c = kTRG_1A_{dm}G_2\left|\alpha_2e^{j\phi_2}\alpha_4e^{j\phi_4}+\alpha_1e^{j\phi_1}\alpha_3e^{j\phi_3}\right|^2 \tag{4.48}$$

Noise factor is then:

$$F_t = \frac{F_1\left(\alpha_2^2\alpha_4^2+\alpha_1^2\alpha_3^2\right)}{\left|\alpha_2 e^{j\phi_2}\alpha_4 e^{j\phi_4}+\alpha_1 e^{j\phi_1}\alpha_3 e^{j\phi_3}\right|^2}+\frac{\left(F_{dm}-1\right)\left(\alpha_4^2+\alpha_3^2\right)}{G_1\left|\alpha_2 e^{j\phi_2}\alpha_4 e^{j\phi_4}+\alpha_1 e^{j\phi_1}\alpha_3 e^{j\phi_3}\right|^2}+$$
$$+\frac{F_2-2}{G_1 A_{dm}\left|\alpha_2 e^{j\phi_2}\alpha_4 e^{j\phi_4}+\alpha_1 e^{j\phi_1}\alpha_3 e^{j\phi_3}\right|^2} \tag{4.49}$$

For the ideal differential amplifier case (i.e. $CMRR \to \infty$), NF measurement error due to mismatches is shown for $NF_{DUT} = 1dB$ in Fig. 4.7(a) and $NF_{DUT} = 5dB$ in Fig. 4.8(a) with the respective contour plots in Fig. 4.7(b) and 4.8(b). For $NF = 1$dB the plots show

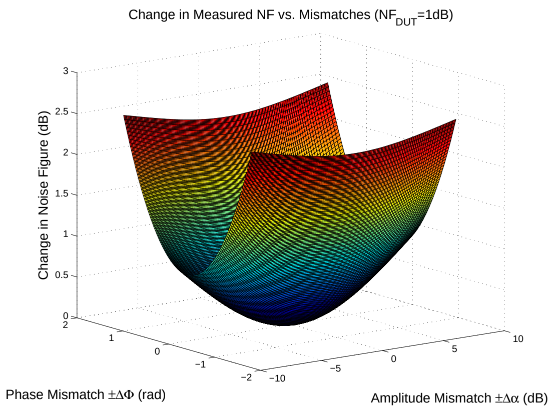

(a) NF Measurement Error 3D Surface

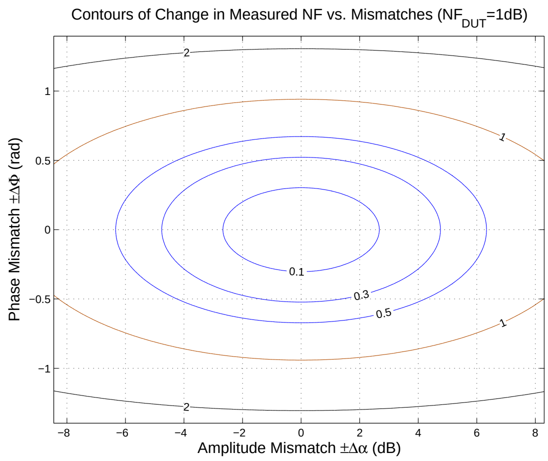

(b) NF Measurement Error Contours

Figure 4.7: NF Measurement Errors due to Mismatches for Ideal Diff. Amp. ($NF_{DUT} = 1dB$)

that reasonable hybrid mismatches ($|\Delta\alpha| \leq 2$dB and $|\Delta\phi| \leq 15°$ result in at most 0.1dB error in measuring differential noise figure. For $NF = 5$dB the plots show that for reasonable hybrid mismatches ($|\Delta\alpha| \leq 2$dB and $|\Delta\phi| \leq 15°$ the error in measuring differential noise figure is even less than in the case of $NF = 1$dB, but practically indistinguishable.

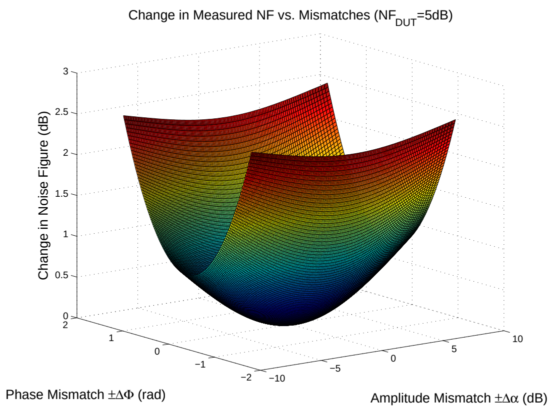

(a) NF Measurement Error 3D Surface vs. Mismatches

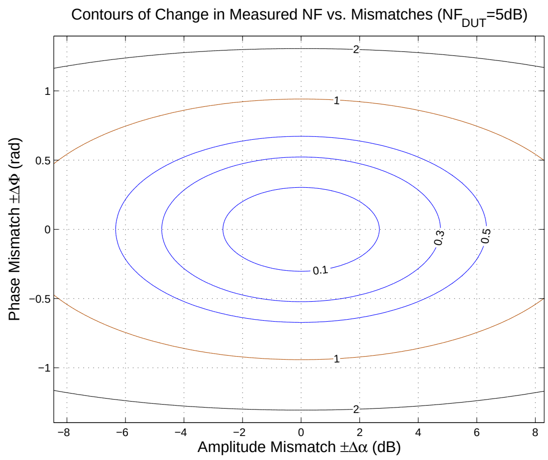

(b) NF Measurement Error Contours vs. Mismatches

Figure 4.8: NF Measurement Errors due to Mismatches for Ideal Diff. Amp. ($NF_{DUT} = 5dB$)

Finite CMRR Differential Amplifier

Amplifier non-idealities, such as finite CMRR along with hybrid mismatches are included in the following analysis; uncorrelated and correlated noise sources are identified and the sum of their total noise contributions is evaluated. The uncorrelated noise sources are represented by the noise introduced by the hybrids and the amplifier; while the source resistor generates correlated noise voltages at the output. The noise powers introduced by the input hybrid at the lower and upper branches are, respectively, at the input of the amplifier:

$$P_{u1} = kTF_1G_1\alpha_2^2 \tag{4.50}$$

$$P_{u2} = kTF_1G_1\alpha_1^2 \tag{4.51}$$

Being independent and uncorrelated sources they can be analyzed using superposition and their powers add up at the output of the amplifier. Devising the same upper and lower differential mode, A_{dm}, and common mode, A_{cm}, gain blocks at the output the noise contributions are:

$$P_{u1} = kTF_1G_1\alpha_2^2 \tag{4.52}$$

$$P_{u2} = kTF_1G_1\alpha_1^2 \tag{4.53}$$

The noise powers from the differential amplifier and output hybrid are, respectively:

$$P_{u3} = kTA_{dm}\left(F_{dm}-1\right)G_2\left(\alpha_4^2\alpha_3^2\right) \tag{4.54}$$

$$P_{u4} = kT\left(F_2-2\right)G_2 \tag{4.55}$$

The total noise power from uncorrelated sources is therefore:

$$P_u = kTG_2\left[F_1G_1A_{dm}\left(\alpha_2^2\alpha_4^2+\alpha_1^2\alpha_3^2\right)+\left(F_{dm}-1\right)\left(\alpha_4^2+\alpha_3^2\right)+\left(F_2-2\right)\right] \tag{4.56}$$

With the source resistor being the only correlated noise source, the upper and lower branch noise voltages at the output are, respectively:

$$V_{c1} = \sqrt{kTRG_1A_{dm}G_2}\alpha_2e^{j\phi_2}\alpha_4e^{j\phi_4} \tag{4.57}$$

$$V_{c2} = \sqrt{kTRG_1A_{dm}G_2}\alpha_1e^{j\phi_1}\alpha_3e^{j\phi_3} \tag{4.58}$$

When these voltages are added they produce an equivalent noise power:

$$P_c = kTRG_1A_{dm}G_2 \left| \alpha_2 e^{j\phi_2} \alpha_4 e^{j\phi_4} + \alpha_1 e^{j\phi_1} \alpha_3 e^{j\phi_3} \right|^2 \tag{4.59}$$

Noise factor is then:

$$\begin{aligned} F_t &= \frac{F_1\left(\alpha_2^2\alpha_4^2 + \alpha_1^2\alpha_3^2\right)}{\left|\alpha_2 e^{j\phi_2} \alpha_4 e^{j\phi_4} + \alpha_1 e^{j\phi_1} \alpha_3 e^{j\phi_3}\right|^2} + \frac{\left(F_{dm} - 1\right)\left(\alpha_4^2 + \alpha_3^2\right)}{G_1\left|\alpha_2 e^{j\phi_2} \alpha_4 e^{j\phi_4} + \alpha_1 e^{j\phi_1} \alpha_3 e^{j\phi_3}\right|^2} + \\ &+ \frac{F_2 - 2}{G_1A_{dm}\left|\alpha_2 e^{j\phi_2} \alpha_4 e^{j\phi_4} + \alpha_1 e^{j\phi_1} \alpha_3 e^{j\phi_3}\right|^2} \end{aligned} \tag{4.60}$$

For nonideal differential amplifier with finite CMRR, two cases are presented:

1. For $CMRR = 30dB$, NF measurement error due to mismatches is shown for $NF_{DUT} = 1dB$ in Fig. 4.9(a) and $NF_{DUT} = 5dB$ in Fig. 4.10(a) with the respective contour plots in Fig. 4.9(b) and 4.10(b).

2. For $CMRR = 45dB$, NF measurement error due to mismatches is shown for $NF_{DUT} = 1dB$ in Fig. 4.11(a) and $NF_{DUT} = 5dB$ in Fig. 4.12(a) with the respective contour plots in Fig. 4.11(b) and 4.12(b).

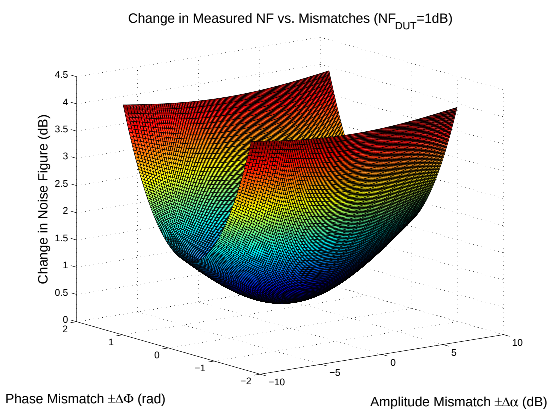

(a) NF Measurement Error 3D Surface

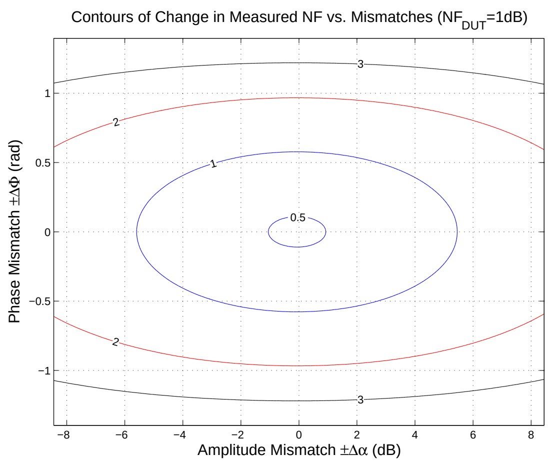

(b) NF Measurement Error Contours

Figure 4.9: NF Measurement Errors due to Mismatches, Diff. Amp. $CMRR = 30dB$ $(NF_{DUT} = 1dB)$

For $NF = 1$dB and CMRR= 30dB the plots show that significant hybrid mismatches ($|\Delta\alpha| \leq 2$dB and $|\Delta\phi| \leq 15°$ introduce a relatively large error ≈ 0.7dB or for lower mismatches ≈ 0.5dB, in measuring differential noise figure. For $NF = 5$dB and CMRR=

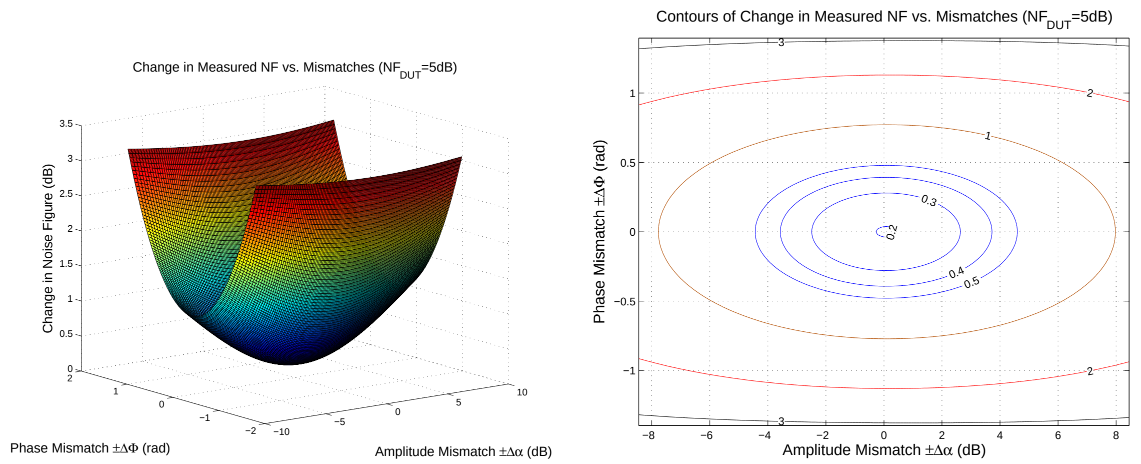

(a) NF Measurement Error 3D Surface

(b) NF Measurement Error Contours

Figure 4.10: NF Measurement Errors due to Mismatches, Diff. Amp. $CMRR = 30dB$ $(NF_{DUT} = 5dB)$

30dB the plots show that reasonable hybrid mismatches ($|\Delta\alpha| \leq 2$dB and $|\Delta\phi| \leq 15°$ introduce at most an error of 0.3dB, almost guaranteed to be 0.2dB, in measuring differential noise figure. For $NF = 1$dB and CMRR= 45dB the results are very close to that of an ideal amplifier with and CMRR$\rightarrow \infty$, reasonable hybrid mismatches ($|\Delta\alpha| \leq 2$dB and $|\Delta\phi| \leq 15°$ result in at most 0.1dB error in measuring differential noise figure. Similar to the ideal amplfier case, CMRR$\rightarrow \infty$, for $NF = 5$dB and CMRR= 45dB reasonable hybrid mismatches ($|\Delta\alpha| \leq 2$dB and $|\Delta\phi| \leq 15°$ result in at most 0.1dB error in measuring differential noise figure. Hence, for practical hybrids and ampifier with $CMRR \gtrsim 40dB$ the errors introduced in measuring the differential NF of an amplifier are expected to be $\lesssim 0.2 - 0.4dB$.

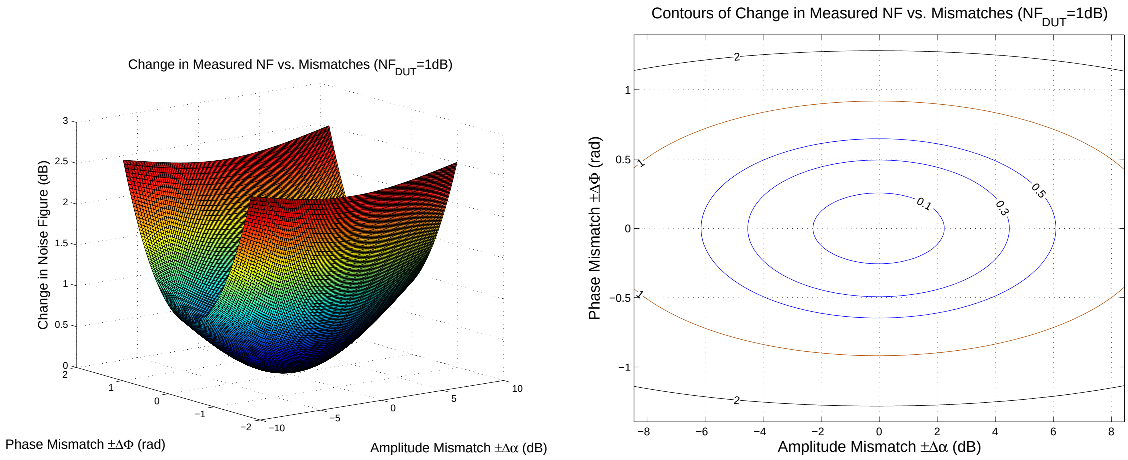

(a) NF Measurement Error 3D Surface (b) NF Measurement Error Contours

Figure 4.11: NF Measurement Errors due to Mismatches, Diff. Amp. $CMRR = 45dB$ $(NF_{DUT} = 1dB)$

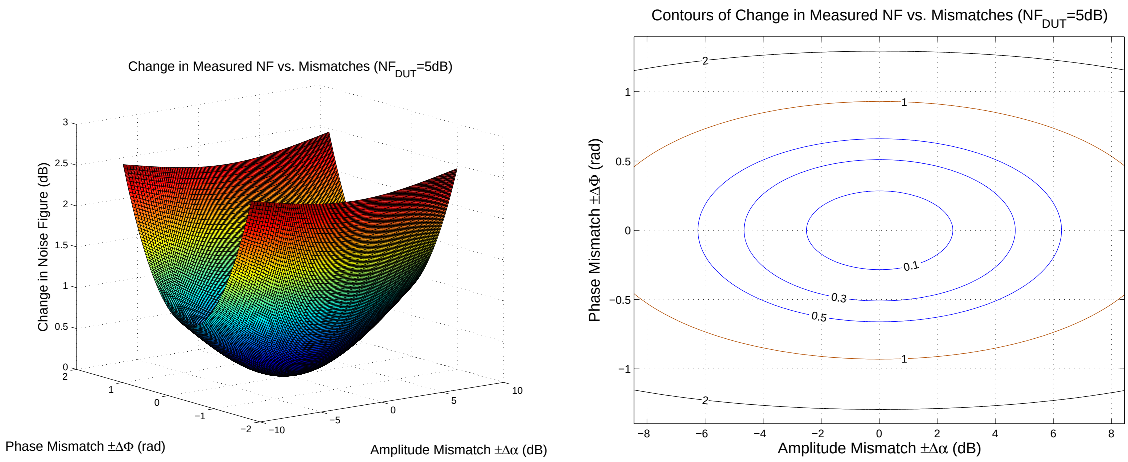

(a) NF Measurement Error 3D Surface (b) NF Measurement Error Contours

Figure 4.12: NF Measurement Errors due to Mismatches, Diff. Amp. $CMRR = 45dB$ $(NF_{DUT} = 5dB)$

Chapter 5

Component Design, Layout and Simulation

5.1 Background on LNA Design

One significant aspect of the LNA design deals with noise analysis and balancing noise performance versus other design parameters such as gain, linearity, bandwidth, matching and stability. Exploring different amplifier topologies and balancing their pros and cons against a series of prioritized requirements facilitates in choosing a particular configuration. The design is analyzed and findings are supported with software simulations in Agilents Advanced Design System (ADS).

5.1.1 Commonly-Used Topologies

There is a wealth of literature material with regard to the performance, optimization and implementation of different LNA configurations [111]- [127]. Popular LNA design architectures include:

1. Common-emmiter (CE) stage with inductive degeneration

2. Common-emmiter stage with shunt feedback

3. Common-base (CB) stage

4. Distributed amplifiers

In their simplified, differential-ended version, commonly used topologies at L or S-band frequencies are presented in Fig. 5.1. The common emitter stage, depicted in 5.2, with

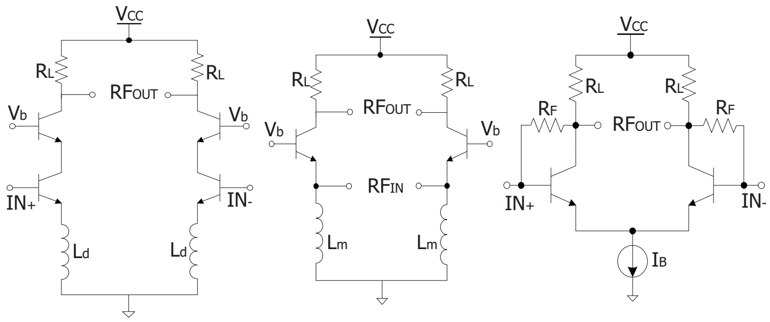

Figure 5.1: Commonly-Used Topologies.

inductive degeneration is very popular in low noise applications presenting an essentially "noiseless" input match, albeit over a narrow band [110], [111]. On-chip LC-ladder match-

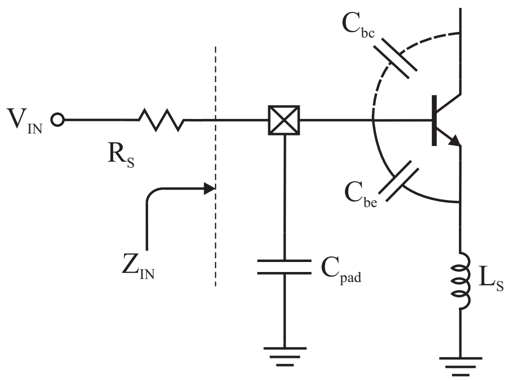

Figure 5.2: Common-Emmitter Stage.

ing networks are employed for broadband designs [112], [113] at the expense of added circuit complexity and size and increased noise figure due to losses in the matching inductors. In addition, the performance of the common-emitter stages is significantly affected by parasitics [114] and consequently by process variations; in differential pairs small circuit imbalances affect the CMRR [115].

Conventional shunt resistive feedback LNAs [116] offer a broadband input match and solid linear performance but suffer from high noise figure and low gain. The combination of weak resistive feedback, applied between the input and output nodes, and inductive degeneration [117], [118] offers trading-off between broadband matching and improvements in noise figure and gain. Alternatively, noise cancelling techniques have been applied to lower the noise figure [119]; the noise cancelling technique relies on exact phase matching and may be difficult to implement broadband, especially at high frequencies.

Traditionally common-base input LNAs, depicted in 5.3, are in general robust when it comes to parasitics and process variations and offer excellent reverse isolation and consequently stability. By proper choice of the bias current the common base stage can be matched to practically any source resistance over a wide-band frequency range, but since it is not a "noiseless" match it tends to have a high noise figure [120] and suffers from relatively low gain; a simple G_m-boosting technique improves gain, noise figure and linearity [122]. Distributed amplifiers offer high IP3 and broadband operation but suffer from a high noise

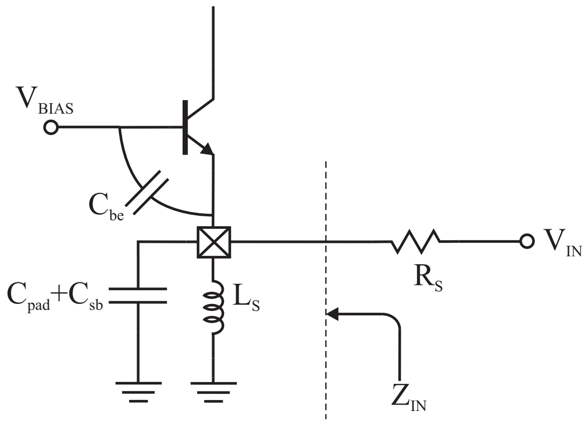

Figure 5.3: Common-Base Stage.

figure [124]- [125] and low reverse isolation [126], which in turn can be of concern in stability determination [127]; in [126] a neutralization technique that employs mixed-mode s-parameter analysis reduces the value of reverse isolation to improve broadband stability. In addition, distributed amplifiers are often applied at high frequencies where transmission line lengths are more appropriate for on-chip implementation.

Cross-modulation analysis of the different transitor amplifier stages has shown [128] that in the matched case, the common base stage performs fundamentally better than a common emitter stage when common-base current gain, $\alpha = \frac{I_C}{I_E} = \frac{\beta_F}{\beta_F + 1} > 0.94$; with current SiGe HBT technologies surpassing such value, common base stages are expected to have fundamentaly lower intermodulation distortion. A comparison of intermodulation distortion in SiGe HBT amplifier stages has been simulated and experimentally verified up to 10GHz with the CB having significantly lower IMD3 products than the CE stage [131]. Noise analysis, on the other hand, shows that common emitter has fundamentally lower noise figure than a common base stage [123]. A short list of strengths and weakness for different LNA architectures is summarized in Table 5.1.

Characteristic	**Inductive Degeneration**	**Common Base**	**Shunt Feedback**	**Distributed**
Gain	Highest	Low	Medium	Low
Broadband Match	Difficult	Easy	Easy	Difficult
Linearity	Medium	High	High	High
Noise Figure	Low	High	High	High
Parasitic Sensitivity	Poor	Robust	Robust	Poor
Reverse Isolation	Medium	High	High	Low
Power Consumption	Medium	Low	High	High

Table 5.1: Strengths and Weaknesses of Common LNA Topologies

5.2 Differential Low Noise Amplifier Design

From the Matlab level simulations in Chapter 3 certain amplifier design parameters take a higher priority in the overall system's performance, albeit *all* affect it in different ways and must be appropriately weighted. For example, ensuring a high CMRR is the most essential since it directly affects the amount of achievable improvement. A broadband input match is also important since it affects the operation of preceeding stages, such as the filter. Low noise and high IP3 are desired to ensure a high dynamic range but rank a bit lower in the scale of priorities. In addition, robustness to parasitics and consequently process variations must be taken into account when choosing a particular topology. For the reasons mentioned above a common-base LNA with G_m boosting technique described in [121] has been chosen as shown in Fig. 5.4. This technique has shown to improve the effective G_m by a factor of

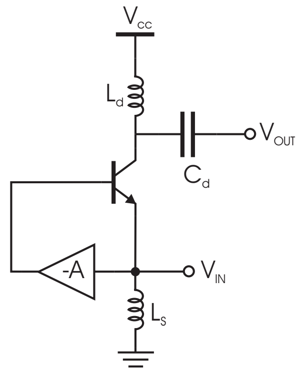

Figure 5.4: Common-Base LNA with FeedBack.

$(1 + A)$, or $G_{m,eff} = (1 + A)g_m$, where $-A$ is the gain from emitter to base [122]. In this design, L_S is used to resonate the junction capacitance, C_{BE} and L_d is an RF choke. The RF output is taken on the other side of the DC blocking capacitor, C_d.

5.2.1 Capacitively Cross-Coupled Common-Base (CCCB)

A key detail and challenge in the G_m-boosted architecture is the implementation of the inverting gain stage between the emitter and base. Since this work makes use of a differential amplifier for rejecting common-mode signals, inverting signals are readily available at the input of a differential pair. To realize the inverting gain stage(s), a natural approach would then be to cross-couple the emitter inputs to the opposite bases; this technique is highlighted in Fig. 5.5. The cross-coupling capacitors C_C are shorts at signal frequencies and therefore realize a gain of $\approx (-1)$. Hence, the effective G_m is doubled $G_{m,eff} = (1 + A)g_m = 2g_m$. As in the single-ended case, the L_S inductors are used to resonate the junction and pad capacitances. Typical common-base amplifiers have transistors with virtual shorts at their

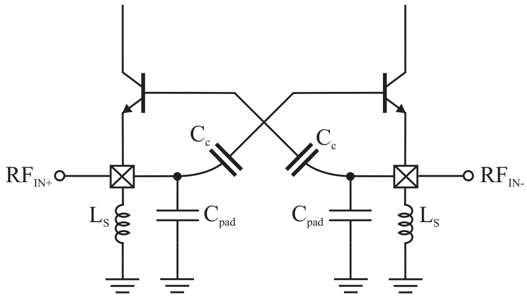

Figure 5.5: Capacitively Cross Coupled Common-Base

bases, however, with the use of cross-coupling this is not possible. The fact that the bases of the differential pair are floating and fed-back to the inputs may present a problem with stability by lowering reverse isolation. In order to improve reverse isolation, cascode devices have been added; the idea is shown in Fig. 5.6. The cascode is biased with a constant voltage

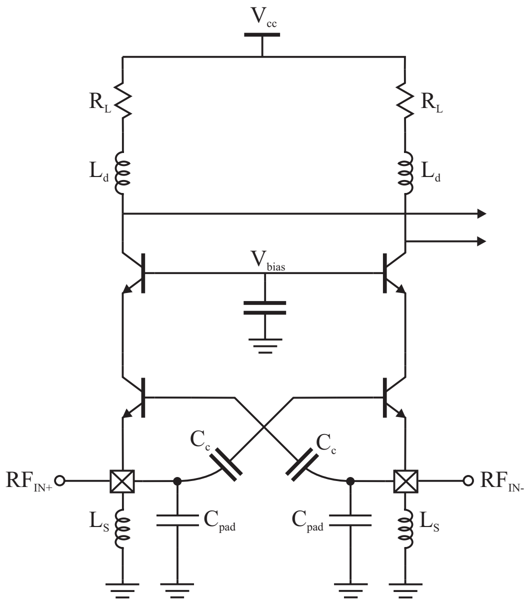

Figure 5.6: Differential CCCB with Cascode.

source, V_{bias}, and a bypass capacitor that is a short at signal frequencies. The supply, V_{cc} is decoupled from the outputs by using a large inductor, L_d, as an RF choke; resistors, R_L can provide additional rejection and act as level shifters to an output stage.

5.2.2 Implementation with BiCMOS 8HP process

IBM's BiCMOS 8HP design kit was chosen to implement the amplifier IC utilizing the ICFB 5.1 (Cadence) environment for schematic, layout, verification and extraction. The BiCMOS 8HP technology features 130nm lithography, $1.7V$ collector-emitter breakdown voltage (V_{CE0}) and 200GHz f_T, enabled by the use of a "raised extrinsic base" structure [136]. The design kit has the option of 5 or 7 metal layers, parametrized cell libraries of passive and active devices and their corresponding models. The 8HP npn transistor model employs the VBIC model [132] which is an improvement over the traditional Gummel-Poon charge-control model [134]; issues that are addressed include impact ionization, self-heating, quasi-saturation and improved Early effect [135].

The aforementioned, capacitively cross-coupled differential LNA topology with cascode has been constructed with the 8HP kit elements and the Virtuoso schematics are presented in Fig. 5.7. In addition to the emitter inductors and the cross-coupling capacitors, the design

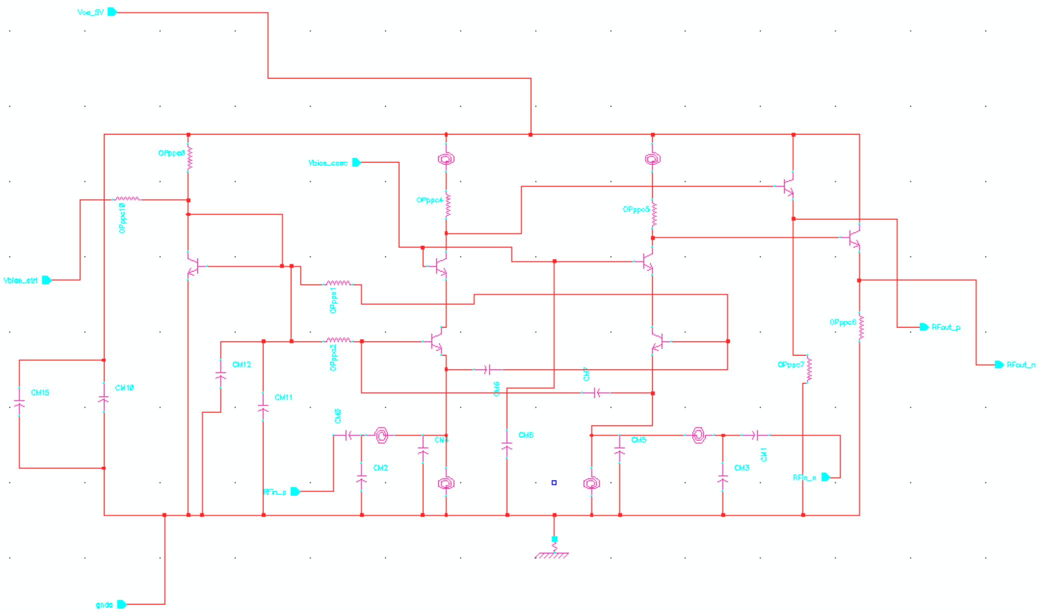

Figure 5.7: Schematics of the Differential LNA Implemented in the BiCMOS 8HP Process

includes matching networks and blocking capacitors at the differential inputs. The bias is supplied via an $\approx 2:1$ current mirror for the differential pair and constant voltage source for the cascode devices; on-chip bypass capacitors are also included. A bondpad connected through a series resistor to the current mirror is used as a tuning knob for the purpose of varying the differential pair's quiescent current. The amplifier includes emitter-followers at the output so as to provide low output impedance; the initial thinking was to be able to drive low impedance circuits, however, this capability was not ultimately tested.

A second set of tuning knobs are inserted at the outputs of the emitter-followers by varying the DC voltage or inserting variable resistors. The idea behind these knobs is to vary the output impedance for either optimal TOI or P_{1dB}, however, the chip was only tested with a fixed 300Ω output resistor. The followers are minimally biased with emitter resistors and do not completely rely on external biasing. Since the output is DC-coupled, a bias-T or blocking capacitor is necessary for testing. "De-Q'ing" the RF chokes (inductors) at the cascode collectors helps with stability and provides biasing for the output followers. Values for key components of the LNA are documented in Table 5.2. While working at sufficiently

Component	**Device Parameter Description**	**Value**
Diff. Pair NPN	Emitter Length	4.8μm
Cross-Coupling Capacitors	Capacitance	9.6pF
Bypass Capacitors	Capacitance	10pF
RF Choke	Inductance	13nH
Current Mirror NPN	Emitter Length	3μm
Current Mirror Resistor	Resistance	3kΩ
Tuning Knob Resistor	Resistance	5kΩ
Emitter Follower NPN	Emitter Length	12μm

Table 5.2: Key Device Parameter Values

low frequencies the amplifier can be biased with the purpose of lowering noise figure rather than achieving peak F_t. Quiescent current was initially chosen by extrapolating limited minimum noise figure data from the manual and further optimized during simulations. Differential pair and emitter follower devices are biased at ≈ 20% of peak F_t. Table 5.3 lists a summary of supply values and device quiescent currents. Most of the quiescent current is

Design Parameter	**Value**
Power Supply	2.5V
Total LNA Quiescent Current	9.75mA
Bias Tuning Knobs	2.5V (nominal)
Diff. Pair Quiescent Current	1.86mA Total (0.93mA Each Device)
Current-Mirror Quiescent I_C	0.89mA
Output Follower Current	3.5mA Each Device (7mA Total)

Table 5.3: LNA Bias Information

consumed by the output followers and if providing low output impedance is not necessary such devices can be completely removed for a drastic reduction in power consumption.

5.3 Simulations with RFIC Dynamic Link to Cadence

Agilent's Advanced Design System (ADS), which can directly interpret spectre models, was employed for RF simulation via RFIC Dynamic Link [171]. The choice of ADS as a simulation tool was primarily made because of user friendly worksheet programming, design templates and harmonic balance; initial simulations showed better convergence and significantly lower simulation times over the shooting methods, especially at higher input power levels.

The small signal ADS simulation environment is indicated in Fig. 5.8, utilizing ideal broadband baluns that convert the differential and common mode to balanced stimuli [101]. The Cadence design is included as a spectre netlist which is interpreted through a "Netlist Include" component for the 8HP models. The S-parameter simulation setup involves a sweep from 500MHz to 4GHz in steps of 10MHz, voltage sources, terminations, display templates, measurement equations and convergence options. The terminations for the common mode and differential mode are chosen [97] to be 25Ω and 100Ω, respectively.

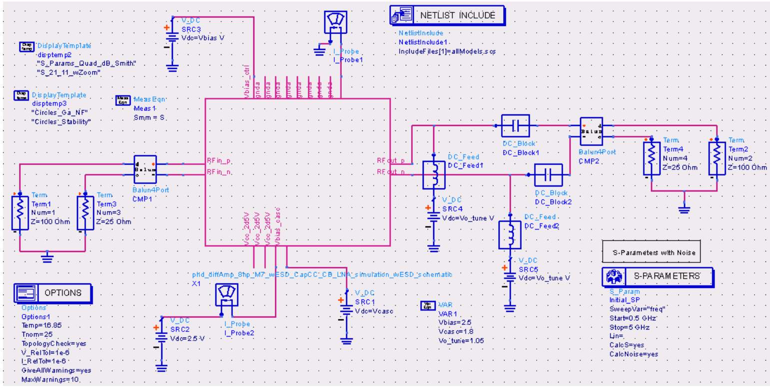

Figure 5.8: Dynamic Link Small-Signal S-Parameter Setup

5.3.1 Small-signal S-Parameters and Noise

The differential and common mode gains are presented in Fig. 5.9 with the resulting CMRR superimposed on the same plot. CMRR is predicted to be better than 40dB

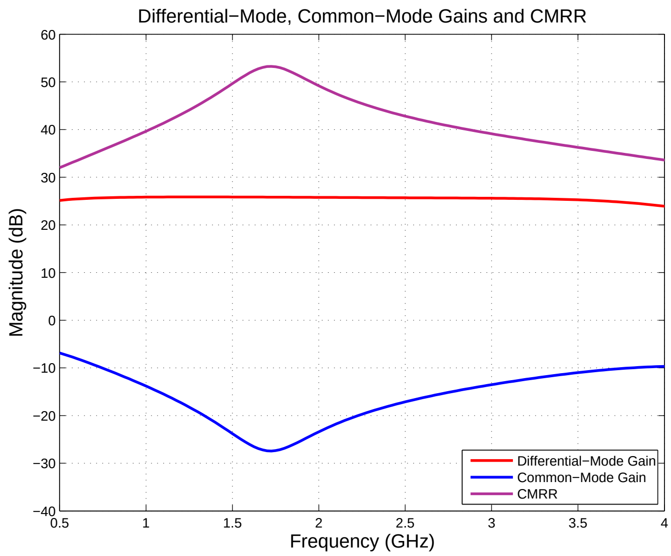

Figure 5.9: Differential and Common-Mode Gains (Schematic)

throughout the band, however, it can be affected by layout parasitics. Return losses and reverse isolation for the differential and common mode are shown in Fig. 5.10. The input

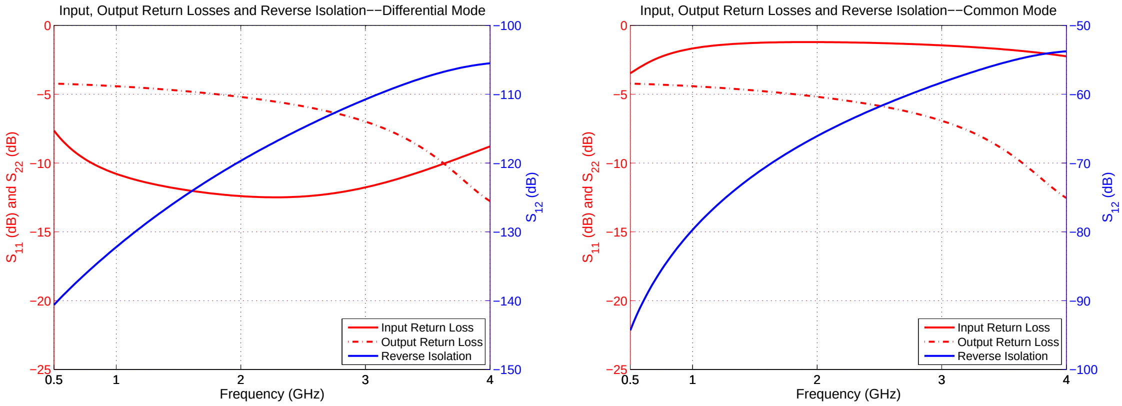

(a) Differential Mode

(b) Common Mode

Figure 5.10: Input, Output Return Losses and Reverse Isolation (Schematic)

match satisfies broadband requirements with S_{11} better than -12dB and reverse isolation < -60dB. Mode conversion gains, an important factor in maintaining high CMRR, are shown in Fig. 5.11 and appear to be below -23dB. Linear noise analysis is conducted via

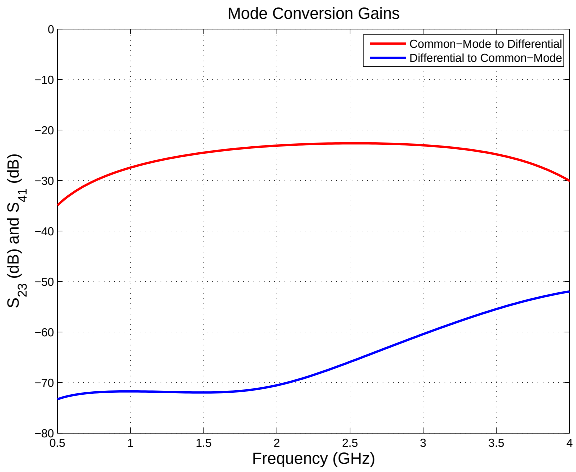

Figure 5.11: Mode Conversions (Schematic)

noisy 50Ω ports that inject wideband thermal noise; noise figure is then computed as the ratio (in dB) of the total noise at the output port to the transmitted input noise. The minimum and actual noise figure values are plotted in Fig. 5.12. Minimum noise figure refers to

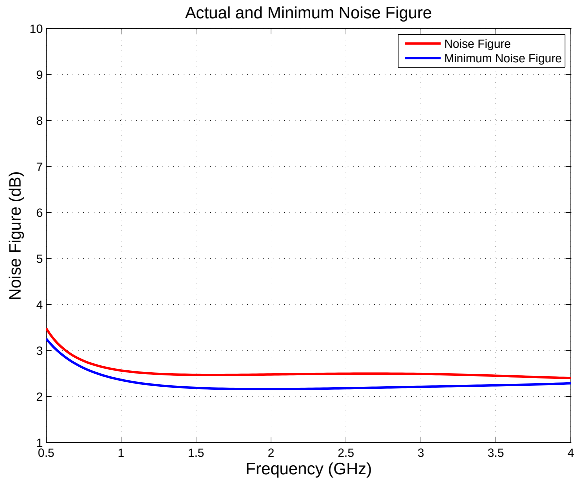

Figure 5.12: Noise Figure of the CCCB LNA (Schematic)

input matching for optimum NF; since the input match is a compromise between conjugate match and minimum NF, actual NF is a bit higher. Actual noise figure appears to be flat $\simeq$ 2.5dB throughout the band of interest, however, it could be affected by higher input network loss and overall parasitics; such parasitics are captured during layout extraction and re-simulation.

5.3.2 Stability

Following the theory presented in Section 4.1.2 differential and common mode stabilities are analyzed separately by looking at the Rollet stability factor. An uncoditionally stable design would require for each mode that $K > 1$ and $B > 0$; these are shown in Figure 5.13(a). Another way to ensure unconditional stability is to compute μ_{load} and μ_{source}; both are plotted in Fig. 5.13(b). Unconditional stability is ensured [139] when either is greater than unity. It is important to note that the simulation band covers frequencies up to F_t. In a standard Smith Chart plot an unconditionally stable design manifests itself in having the load impedance circle lie completely outside of the $|\Gamma_{in}| < 1$ region of the Smith Chart, or vice-versa have the source impedance circle lie outside of the $|\Gamma_{out}| < 1$

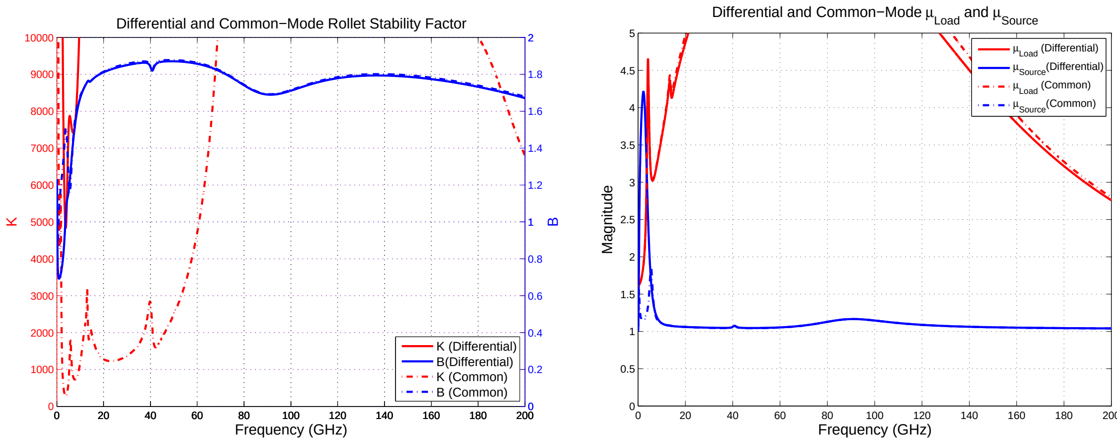

(a) Rollet Stability Factor (b) Geometric Stability Factor

Figure 5.13: Rollet and Geometric Stability Factor (Schematic)

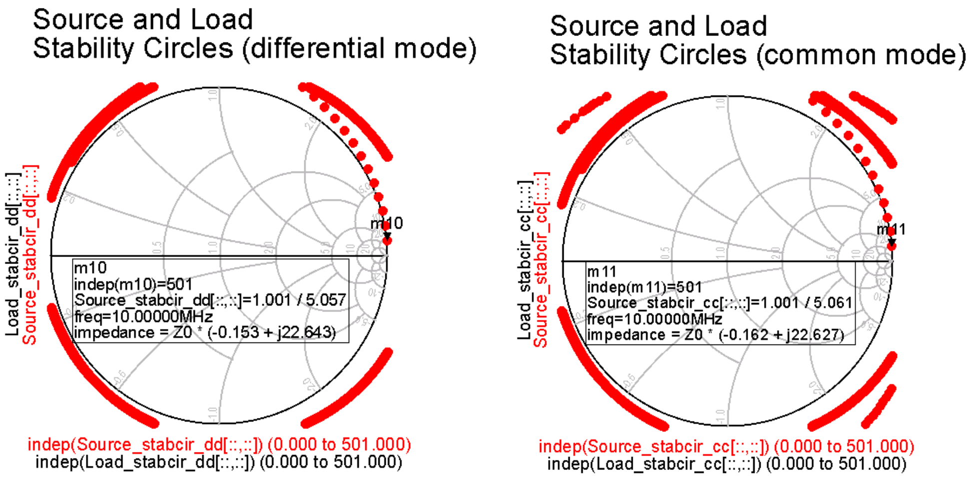

(a) Differential Mode (b) Common Mode

Figure 5.14: Source and Load Stability Circles (Schematic)

region [142], where $|\Gamma_{in}|$ and $|\Gamma_{out}|$ are the magnitudes of the input and output reflection coefficients. The source and load stability circles are plotted in Fig. 5.14, these circles lie outside the standard Smith Chart ensuring unconditional stability. Even at low frequencies where the load and source stability circles seemingly touch the edge of the standard Smith

Chart, the resistive part is negative (as indicated in the Figure) which cannot be realized with passive terminations.

5.3.3 Nonlinear Performance

Nonlinear analysis is carried out with the harmonic balance tool in ADS using single tone and two tone stimuli.

Single Tone Simulations

The large signal gain of the amplifier is investigated at fixed frequency points while sweeping the input power. Large signal gain is simulated at 1GHz, 2GHz and 3GHz with the results plotted in Fig. 5.15(a). In addition, output powers of the main tone, second and third harmonis are shown in Fig. 5.15(b), 5.16(a) and 5.16(b) for the three aforementioned frequency points. From the graphs it can be deduced that the input P_{1dB} (IP_{1dB}) is

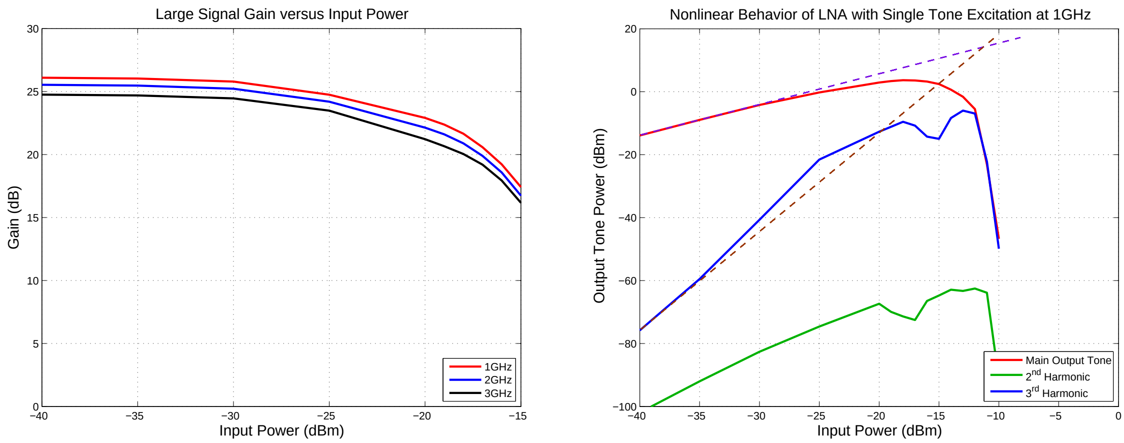

(a) Large Signal Gain

(b) Harmonic Content at 1GHz

Figure 5.15: Large Signal Gain and Harmonic Content at 1GHz (Schematic)

around -25dBm corresponding to output P_{1dB} (OP_{1dB}) of $\simeq 0$dBm.

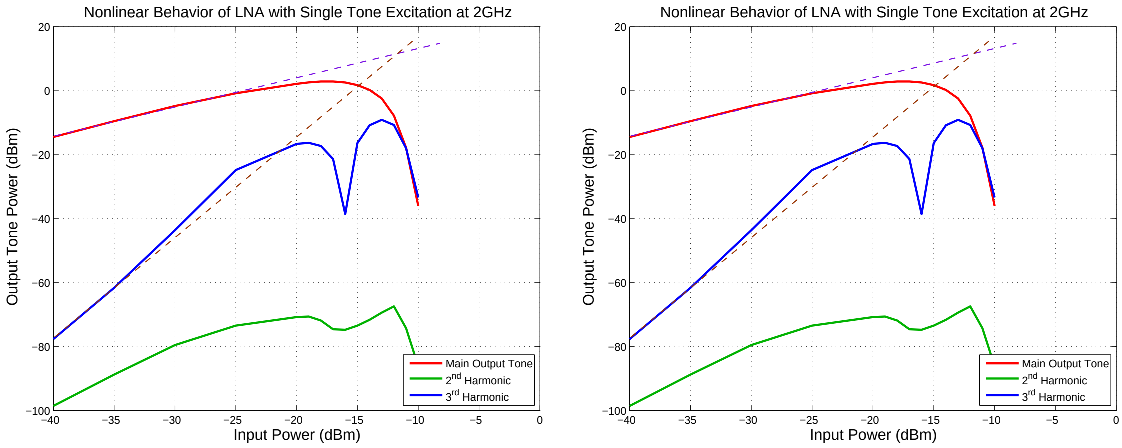

(a) Harmonic Content at 2GHz (b) Harmonic Content at 3GHz

Figure 5.16: Harmonic Content at 2 and 3GHz (Schematic)

Two Tone Simulations

Setup for fixed-frequency two tone simulations with swept power is given in Fig. 5.17. Simulations are carried out at 1, 2 and 3GHz while sweeping the input tone power −50dBm

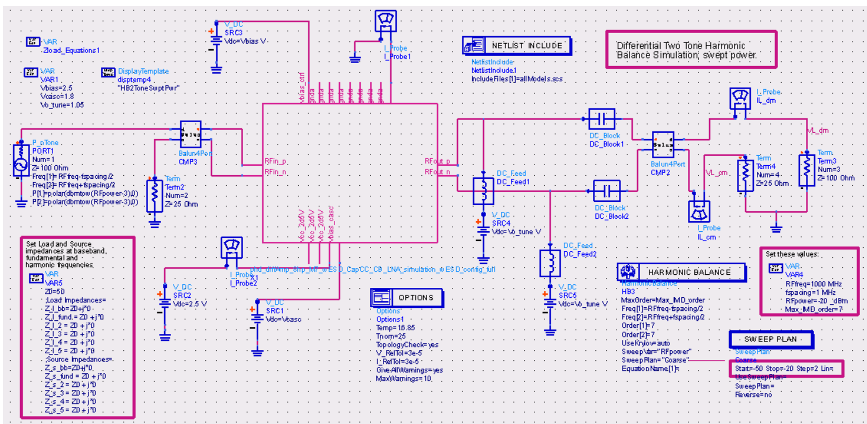

Figure 5.17: Two Tone Intercept Point Simulation Environment

to −20dBm. Output thid order intercept points are plotted in Fig. 5.18. As seen in the graph OTOI, is > 12dBm throughout the band; this value adheres to the rule of thumb

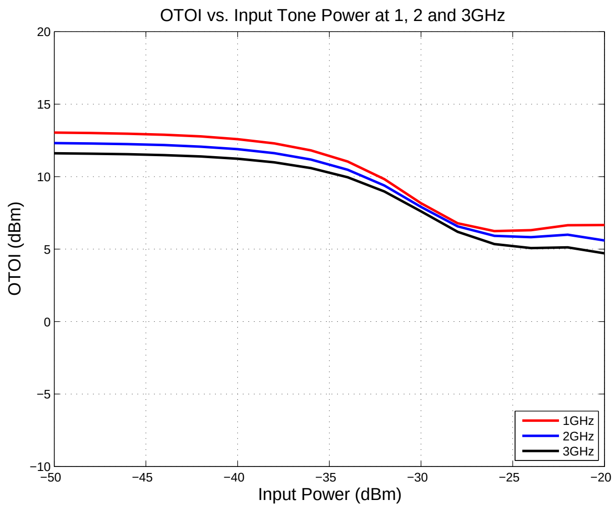

Figure 5.18: Output TOI with Swept Input Power (Schematic)

OTOI$\approx OP_{1dB} + 10$, where OP_{1dB} was estimated to be $\simeq$ 0dBm from one tone simulations.

5.3.4 Rejection Investigation with Harmonic Balance

ADS Harmonic Balance was employed to investigate the large signal common mode rejection ratio of the amplifier; the simulation environment is shown in Fig. 5.19. Two

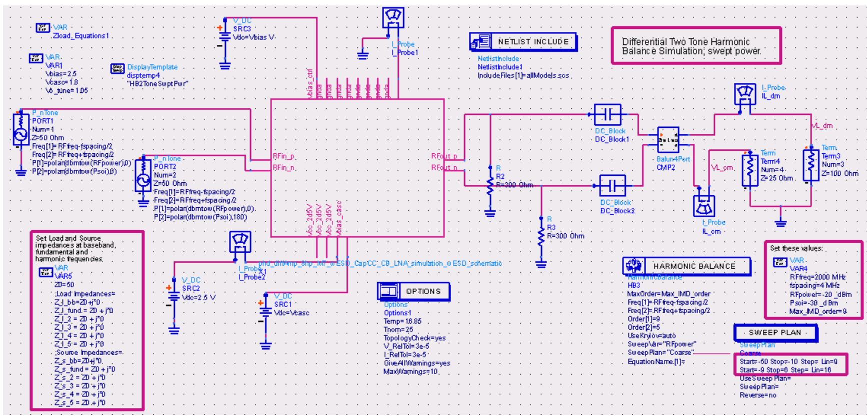

Figure 5.19: Rejection Investigation with Harmonic Balance

separate tones, representing the interferer and SOI, are independently injected at the differential inputs of the amplifier. While the interfering tones are presented as common-mode, the SOI tones are differential. The signals are 4MHz apart and the SOI tone is fixed at −30dBm. Two cases are observed:

1. Balanced interferer levels, representing the case when the system implementation achieves perfectly balanced interfering tones at the differential amplifier inputs.

2. Unbalanced interferer levels, representing the case when interfering tones at the differential inputs have amplitude or phase mismatches, or both.

Balanced Levels

Figures 5.20(a) and 5.20(b) show the harmonic output due to interferer power levels of −30dBm and 0dBm, respectively. The simulations show that with balanced levels the

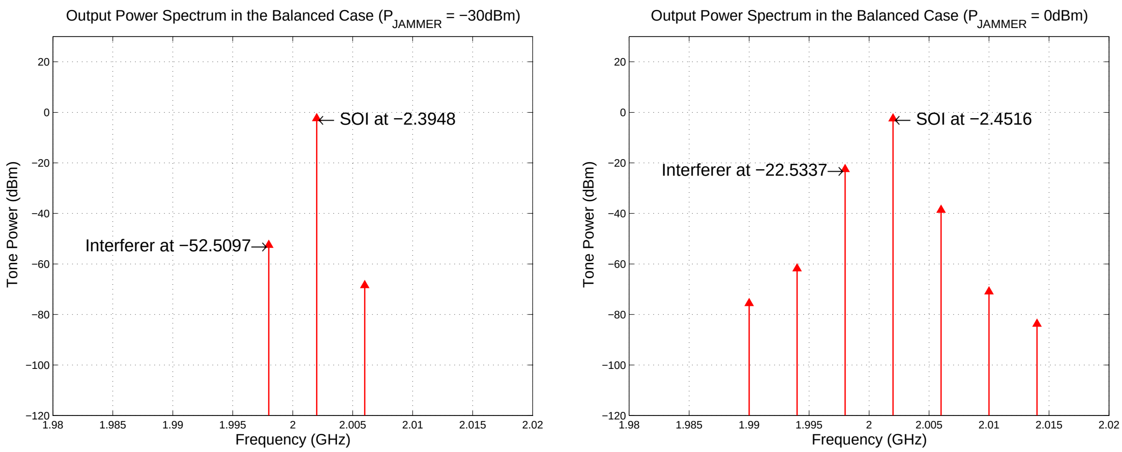

(a) $P_{\text{Interferer}} = -30\text{dBm}$ (b) $P_{\text{Interferer}} = 0\text{dBm}$

Figure 5.20: Spectrum with Balanced Interfering Tones (Schematic)

amplifier maintains its rejections ability beyond 0dBm and the differential gain is virtually unaffected; an SINR $\approx$ 50dB is achieved. Although the jammer is rejected, at higher power levels, such as 0dBm, the linearity suffers due to substantial mixing products.

Unbalanced Levels

In these scenarios mismatches are presented in the amplitude or phase of the interfering tones in each branch. Figures 5.21(a), and 5.21(b) show the effect on output spectrum due to amplitude imbalances of 0.5dB with interferer power levels of −30dBm and −10dBm, respectively. The simulations show that moderate amplitude mismatches between branches

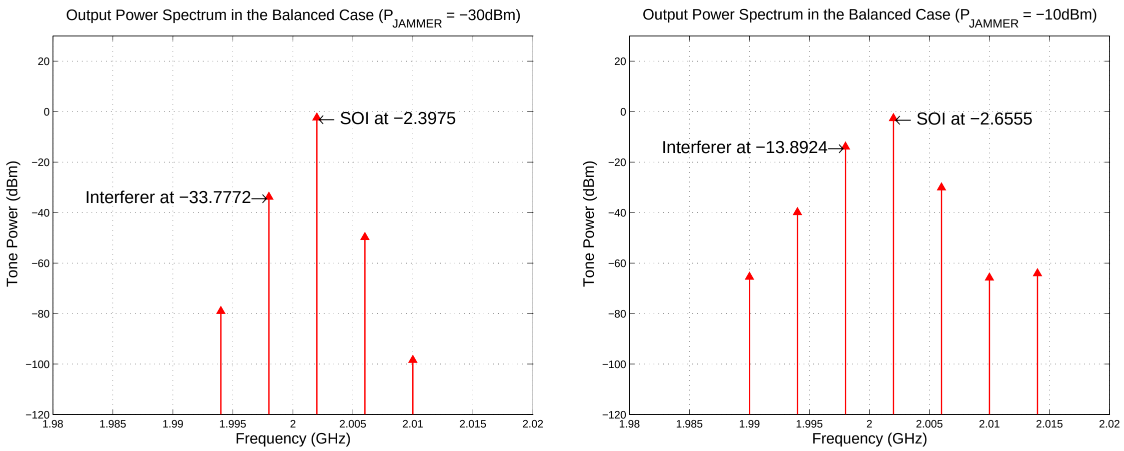

(a) $\mathrm{P_{Interferer}} = -30\mathrm{dBm}$

(b) $\mathrm{P_{Interferer}} = -10\mathrm{dBm}$

Figure 5.21: Spectrum with Amplitude Mismatches (Schematic)

significantly degrade the amplifier's ability to reject interfering tones; as compared to the balanced case rejection has degraded by ≈ 19dB to an SINR ≈ 31dB. Linearity is visibly impacted, as well.

Figures 5.22(a), and 5.22(b) show the effect on output spectrum due to phase imbalances of 10° with interfering tones of −30dBm and −10dBm, respectively.

As seen in the graphs, the effect on rejection and linearity is even more pronounced with large phase mismatches; SINR ≈ 23dB at low input power levels.

Figures 5.23(a), and 5.23(b) show the effect on output spectrum due to amplitude imbalances of 0.5dB and phase imbalances of 10° between interfering tones of −10dBm and −10dBm, respectively. The rejection and linearity degradation is maximized with relatively large amplitude and phase imbalances. Seemingly, this degradation does not differ substan-

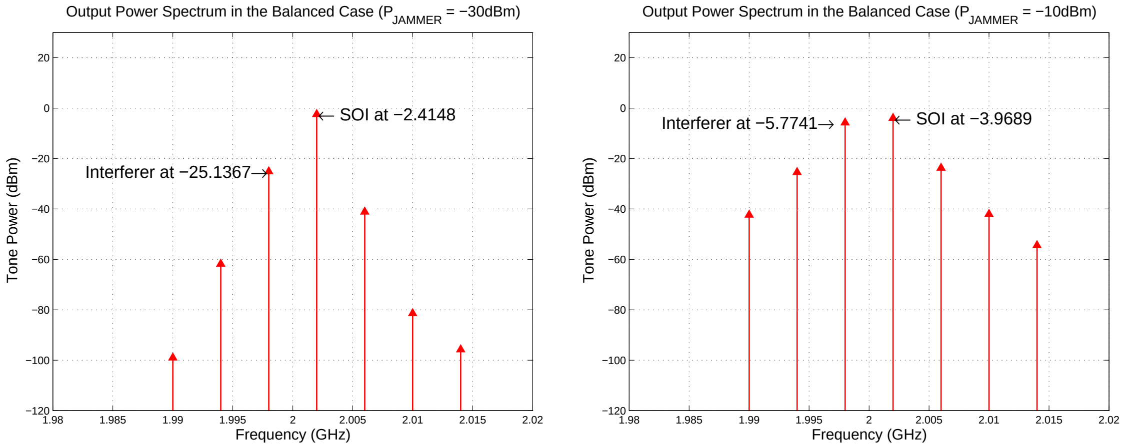

(a) $P_{\text{Interferer}} = -30\text{dBm}$ (b) $P_{\text{Interferer}} = -10\text{dBm}$

Figure 5.22: Spectrum with Phase Mismatches (Schematic)

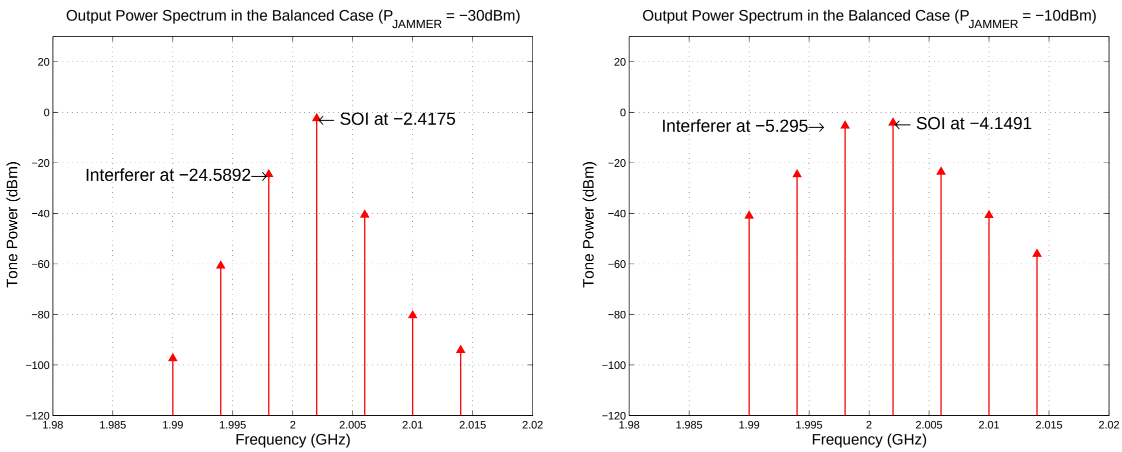

(a) $P_{\text{Interferer}} = -30\text{dBm}$ (b) $P_{\text{Interferer}} = -10\text{dBm}$

Figure 5.23: Spectrum with Amplitude Phase Mismatches (Schematic)

tially from the phase-imbalanced condition; this can be seen from the large signal gain versus interferer power for the balanced and the aforementioned unbalanced cases in Fig. 5.24. These results represent worst-case scenarios in degradation of rejection and linearity, yet they underscore the need to finely tune signals so that mismatches are minimized through

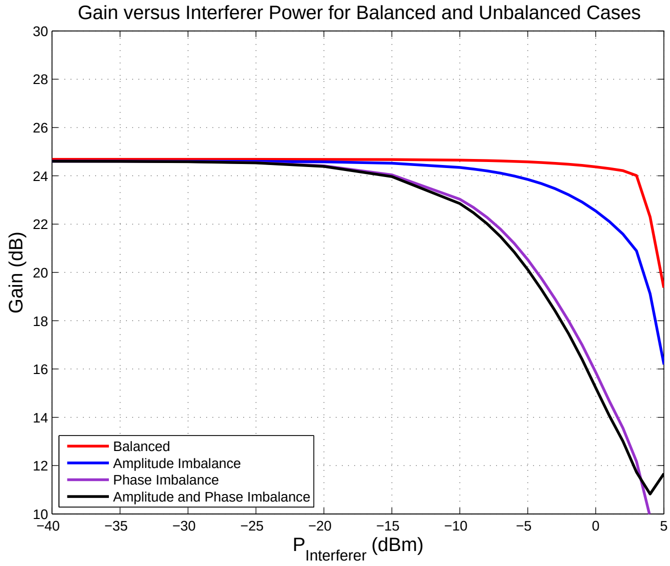

Figure 5.24: Large Signal Gain Versus Interferer Power (Schematic)

phase shifters and variable attenuators. The system implementation assumes a feedback mechanism that minimizes these imbalances.

5.4 IC Layout of the Amplifier

This section presents the amplifier layout, rule checking, extraction and re-simulation using ADS.

5.4.1 Layout Design Checks

Starting with the amplifier schematics the layout procedure involves the folowing major steps:

1. Generation of passive and active device layout utilizing parametrized cells.
2. Arrangement and interconnections between different devices paying close attention to layout design rules. This part is done manually by the designer.
3. A variety of design rule checks to comply with guidelines provided in the design kit.
4. Modification of layout until all design rule checks are satisfied.

Prior to manufacturing, the IC has to undergo a series of rule checks to comply with technology limitations, ensure reliability and reduce poor yields, as well as increase structural integrity [133]. These design rules are categorized as follows:

1. DRC (design rule checks): to comply with technology limits and necessary for the layout to be manufactured. A series of switches, most notably GridCheck, can be set. GridCheck makes sure the design conforms to the minimum allowed grid spacing and that no vertices are "off-grid".
2. Floating gate/Floating Metals/Antenna: to prevent build-up of charge and electrical overstress, tie-downs (resistors or small diodes) are required. These checks prevent ESD damage to Metal-Insulator-Metal (MIM) capacitors and gates of CMOS devices during chip manufacturing.
3. Density checks: to ensure structural integrity of the IC (explained further below).
4. Layout versus schematic (LVS): ensures layout and schematic match; not absolutely required to manufacture part but necessary for proper operation.

Density checks are put in place to balance out the material density throughout the chip so as to ensure mechanical integrity. Whenever there is a high density ratio between more dense areas to less dense areas manufacturing yields have proven to be poor. In order to equalize the density of certain areas, dummy metal “fill” is manually added. All metal layers and certain active layers, such as RX and PC, have minimum and maximum density percentages that must be met. Density checks are conducted both locally and globally. Problems inherently exist in the area of inductors; local density checks are almost guaranteed to fail since additional metal would alter the behavior of the inductors, however, these can be waived by IBM. In addition, electrostatic discharge (ESD) protection circuits, comprising of fast diodes, were added at the RF input. The layout was completed using Cadence Virtuoso XL and rule checking with Assura, which is integrated into the Cadence design environment. The complete LNA IC layout area is 2×1mm and is presented in Fig. 5.25. The differetial inputs are on the left and outputs on the right; the 50Ω lines were kept

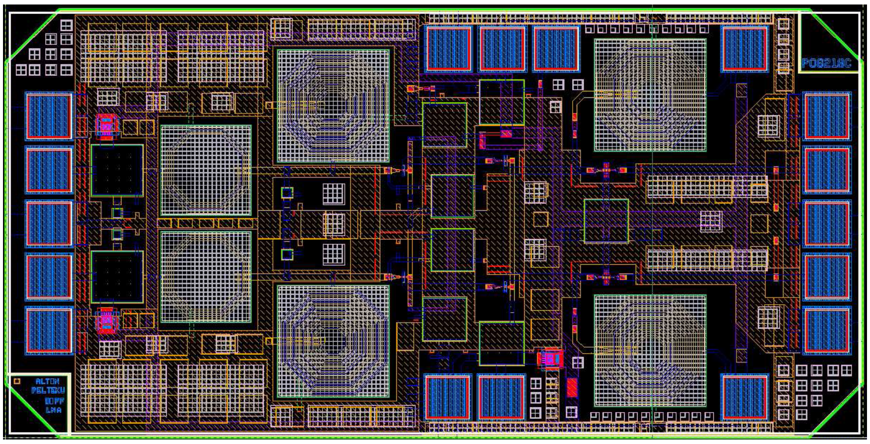

Figure 5.25: Photo of the LNA IC Layout.

as straight as possible to minimize losses. In addition, elements have been arranged as to preserve the symmetry between the upper and lower branches of the amplifier.

IC Manufacturing

The differential LNA was manufactured using the 7-metal layer version of the IBM 8HP, 130nm, BiCMOS process. A grayscale picture of the manufactured IC die is presented in Fig. 5.26.

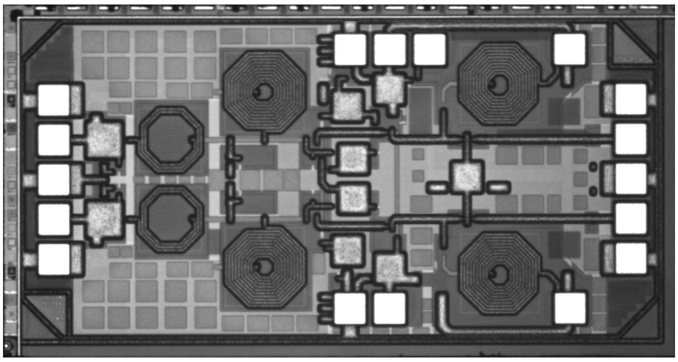

Figure 5.26: Photo of the LNA IC Die

5.4.2 Extraction and Re-simulation

After passing DRC/LVS checks, full-chip RLC parasitic extraction of the layout was undertaken using a 5μm grid. Several switches were set to minimize netlist size: minimum resistor value was set to $R_{min} = 0.05\Omega$ and capacitor value to $C_{min} = 0.1fF$. A benefit of the ADS dynamic link is the switching of the netlist views "on the fly", results can be obtained with the same worksheet by prioritizing the extracted view in the switch-view list.

Small Signal Performance and Noise

The differential and common mode gains along with input return losses are presented in Fig. 5.27. The resulting CMRR with the overlaid schematic results is shown in Fig. 5.28. The input match satisfies broadband requirements with S_{11} better than -13dB, which is slightly better than the schematic simulations. The differential gain shows roll-off with frequency, which can be due to layout asymmetries and parasitics, as well as a lack of distributed elements in the schematic design. CMRR varies $33-38$dB throughout the band

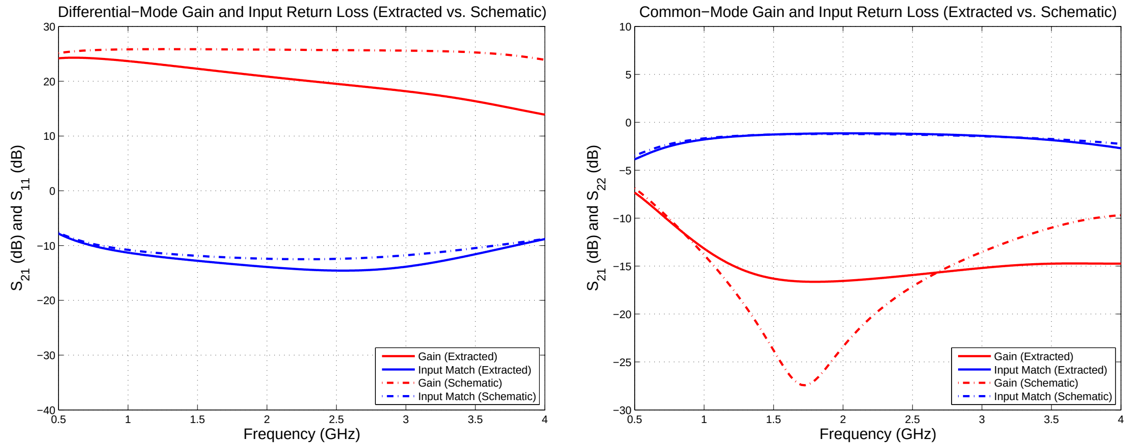

(a) Differential Mode

(b) Common Mode

Figure 5.27: Gain and Input Return Loss (Extracted)

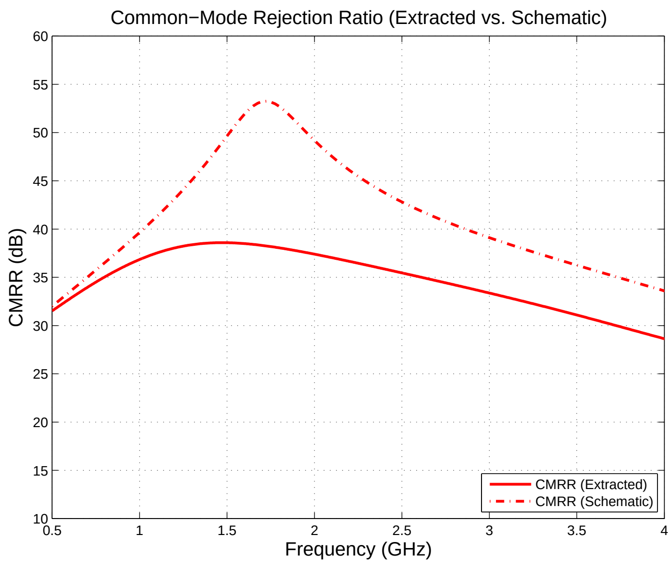

Figure 5.28: CMRR for the Extracted CCCB LNA (Extracted)

and it has been affected by parasitics and mismatches in the layout. Output return loss and reverse isolation are shown in Fig. 5.29. Disregarding slight differences, it can safely be concluded that the output match and reverse isolation results line up well with the

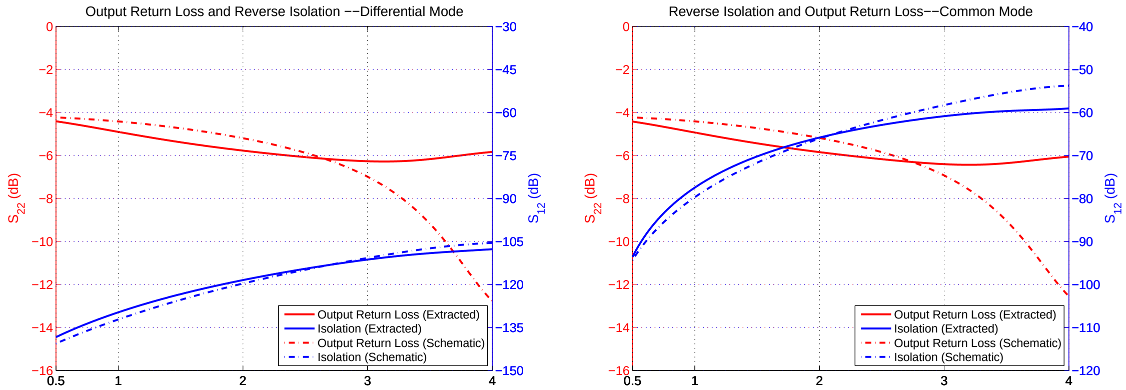

(a) Differential Mode

(b) Common Mode

Figure 5.29: Output Return Loss and Reverse Isolation (Extracted)

schematic design. Mode conversion gains are shown in Fig. 5.30. Common-to-differential

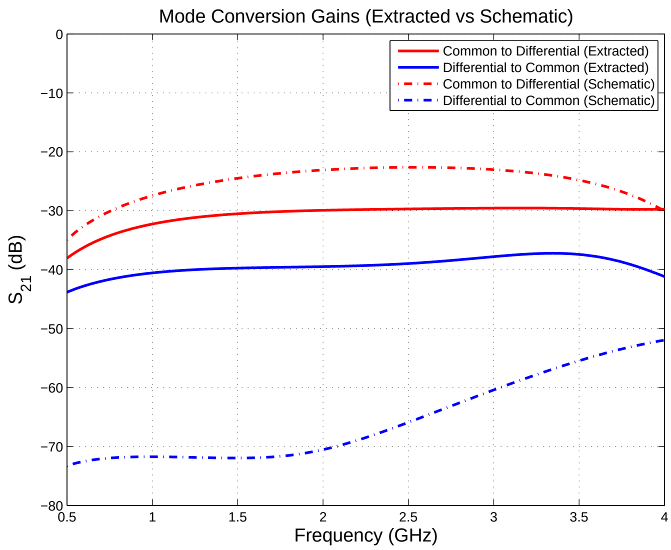

Figure 5.30: Mode Conversion Gains (Extracted)

gain has improved versus the schematic design and is below -30dB; both conversions are significantly lower than the common-mode gain and can be safely ignored in the computation of the common-mode rejection ratio. The minimum and actual noise figure values for the extracted view are plotted in Fig. 5.31. Actual noise figure appears to be below 3dB

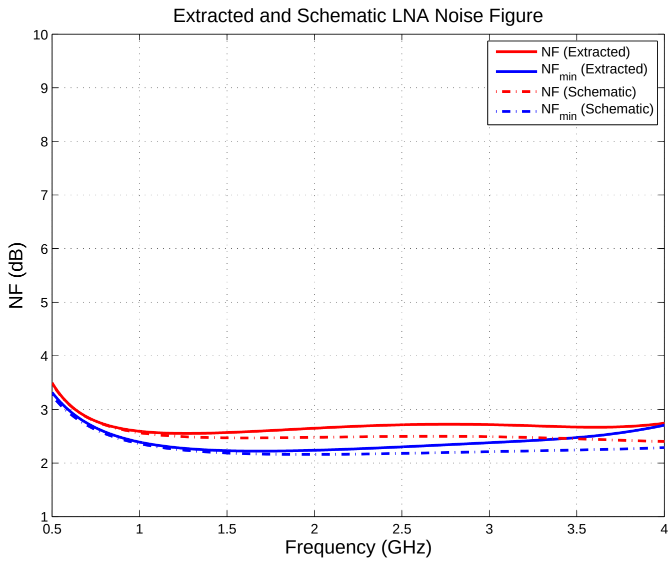

Figure 5.31: Noise Figure of the LNA (Extracted)

throughout the band of interest and remains nearly unchanged from schematic simulations.

Stability

Similar to the schematic case differential and common mode stabilities are observed by looking at the Rollet and Geometric stability factors, shown in Fig. 5.32. There are healthy

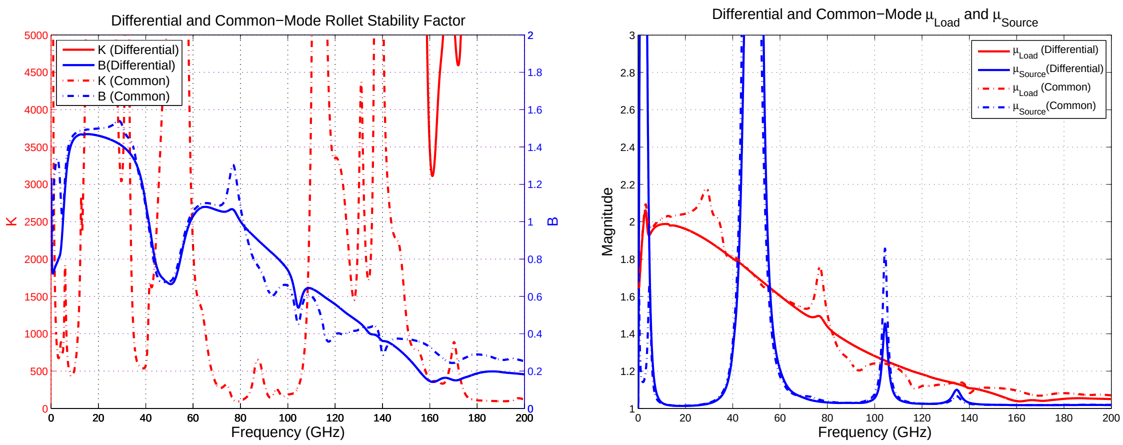

(a) Rollet Stability Factor

(b) Geometric Stability Factor

Figure 5.32: Rollet and Geometric Stability Factor (Extracted)

margins in both differential and common mode Rollet factors due to several factors. First, the cascode isolates the input from output so reverse isolation is very low. Second, there is enough loss in the input matching networks so that no additional stability networks are necessary. Stability is verified by the μ_{source} and μ_{source} graphs with values > 1 for all frequencies up to F_t. In short, the design should be unconditionally stable.

Single and Two Tone Results

The large signal gain of the amplifier is simulated at 1GHz, 2GHz and 3GHz with the results plotted in Fig. 5.33(a). In addition, output powers of the main tone, second and third harmonis are shown in Fig. 5.33(b), 5.34(a) and 5.34(b) for the three aforementioned frequency points.

While gain at low input powers is lower at higher frequencies versus schematic simulations, the results remain largely unchanged in terms of input compression point, that is $IP_{1dB} \approx$

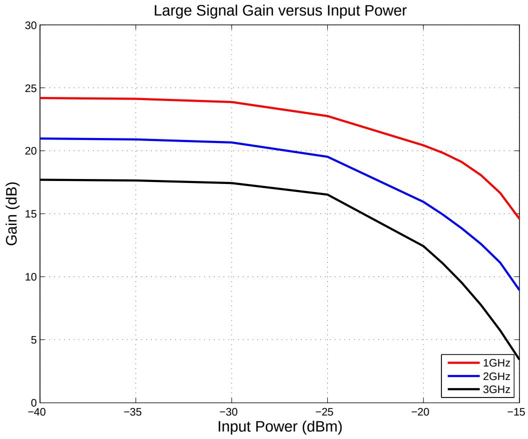

(a) Large Signal Gain

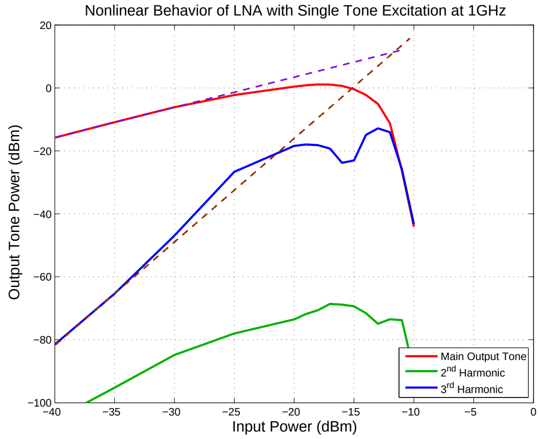

(b) Harmonic Content at 1GHz

Figure 5.33: Large Signal Gain and Harmonic Content at 1GHz (Extracted)

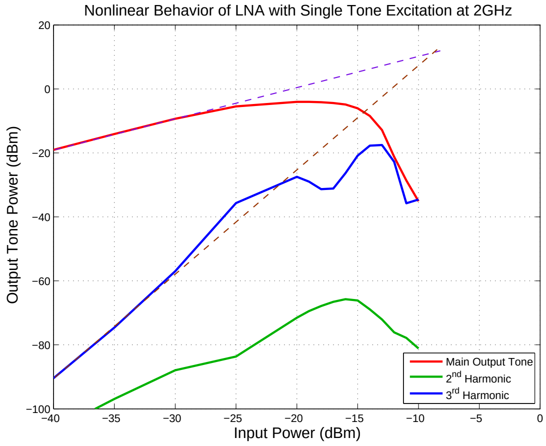

(a) Harmonic Content at 2GHz

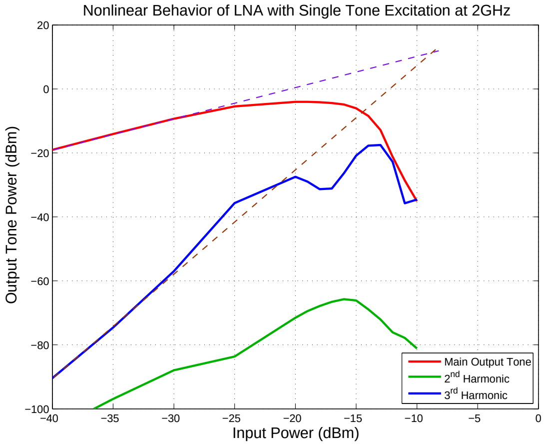

(b) Harmonic Content at 3GHz

Figure 5.34: Harmonic Content at 2 and 3GHz (Extracted)

-25dBm. Since there is greater variation in gain the OP_{1dB} varies ≈ -7 to -1dBm. Output thid order intercept points, centered around 1, 2 and 3GHz, are plotted in Fig. 5.35. As seen in the graph, OTOI is > 7dBm throughout the band; the values are lower

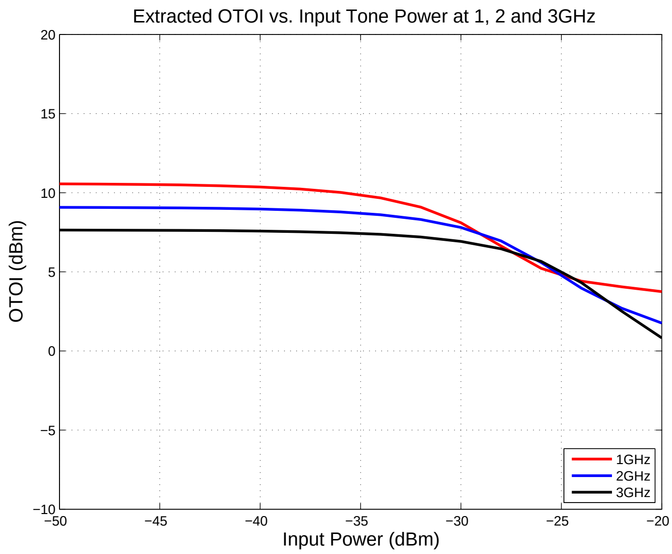

Figure 5.35: Output TOI with Swept Input Power (Extracted)

when compared to schematic simulations due to the degradation of the small-signal gain at the high-end of the frequency band.

Performance Distribution with Monte Carlo Analysis

8HP models make use of the "process model" which allows for observation of circuit performance under random variations in device parameters. These variations, listed in the design manual [133], are captured by statistical distributions that are enabled during Monte Carlo (MC) analysis. The devices varied include transistors, resistors, capacitors, inductors and transmission lines. The designer can then focus on certain critical performance parameters and their variability over process. For example, Fig. 5.36(a) shows the variability in differential and common mode gains as well as CMRR over 150 Monte Carlo trials; a histogram plot at 3GHz over the same trials is given in Fig. 5.36(b). Figures 5.37(a) and 5.37(b) are histogram plots of CMRR at 1GHz and 3GHz over 150 Monte Carlo trials.

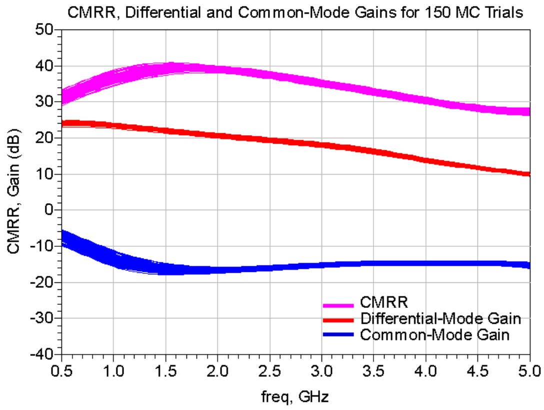

(a) Gain and CMRR over 150 Trials

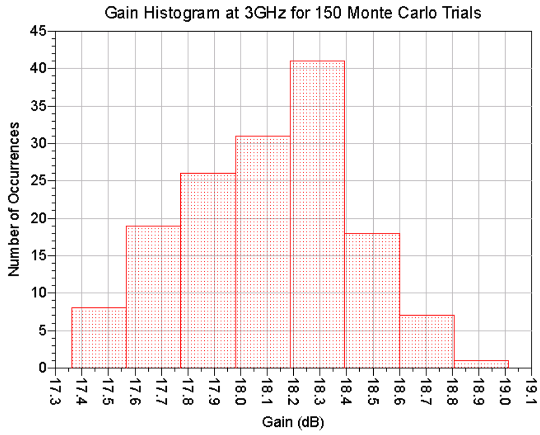

(b) Histogram Plot of Gain at 3GHz

Figure 5.36: Gain and CMRR over 150 Monte Carlo Trials (Extracted)

The plots show there is reasonable performance spread over process and the mean of some

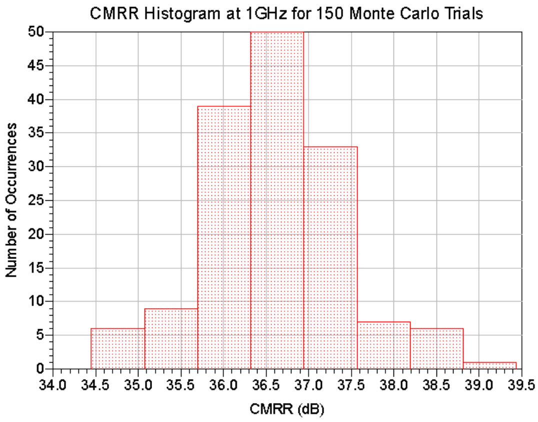

(a) Histogram Plot of CMRR at 1GHz

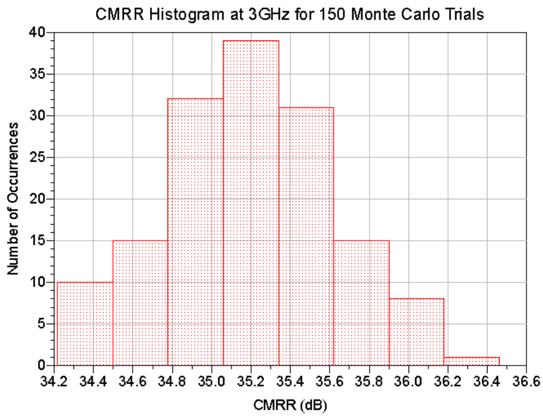

(b) Histogram Plot of CMRR at 3GHz

Figure 5.37: Histogram Plots of CMRR over 150 Monte Carlo Trials (Extracted)

parameters, most notably gain at 3GHz, trends toward lower values. Since Monte Carlo analysis randomnly picks parameter values according to their distribution within $\pm 3\sigma$, a Monte Carlo graph should represent the full range of the expected performance.

5.5 Custom Test Fixture Design

This section describes the design procedure of the different RF subsystems and peripherals used in the testing of the differential LNA. The peripherals described below have been implemented onto a PCB, manufactured by Advanced Circuits, using the Mentor Graphics software PADS.

5.5.1 Fixed and Tunable Combline Filters

The tunable combline filter is used to demonstrate the ability to track and nullify the interfering tone. The main idea of the combline filter was introduced in Section 4.1.3. In order to implement a tunable combline filter, varactors were arranged in an anti-series topology so as to minimize nonlinear distortion [165]. The simplified construction of the filter is depicted in Fig. 5.38.

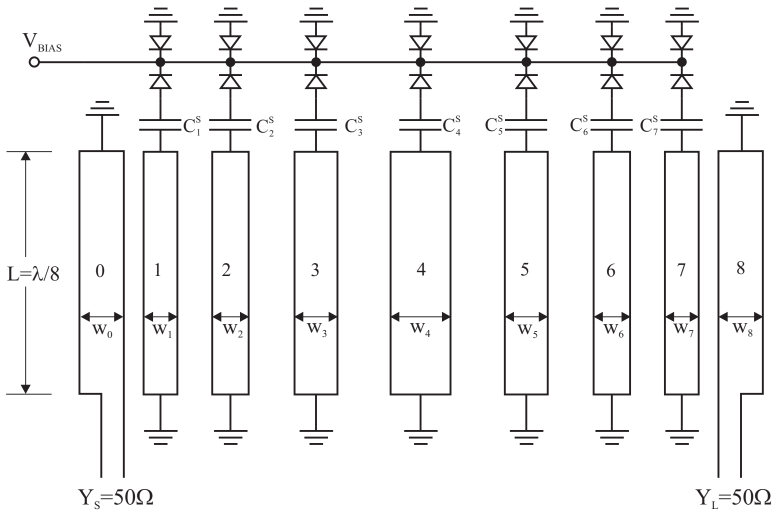

Figure 5.38: Tunable Combline Filter.

5.5.2 FEM Prediction of the Combline Filter

A fixed frequency combline filter was constructed with HFSS, realizing capacitive terminations as lumped impedance boundary conditions enabled by the following equation:

$$\vec{E}_{tan} = Z_s(\hat{n} \times \vec{H}_{tan}) \tag{5.1}$$

where, $\hat{n}$ is the normal unit vector to the surface, $\vec{E}_{tan}$, $\vec{H}_{tan}$ the tangential components of the $\vec{E}$-field and $\vec{H}$-field and Z_s the surface impedance of the boundary.
The HFSS geometry, ports and terminating capacitors are depicted in Fig. 5.39. FEM results for the insertion, input return loss and transmission phase are shown in Fig. 5.40.

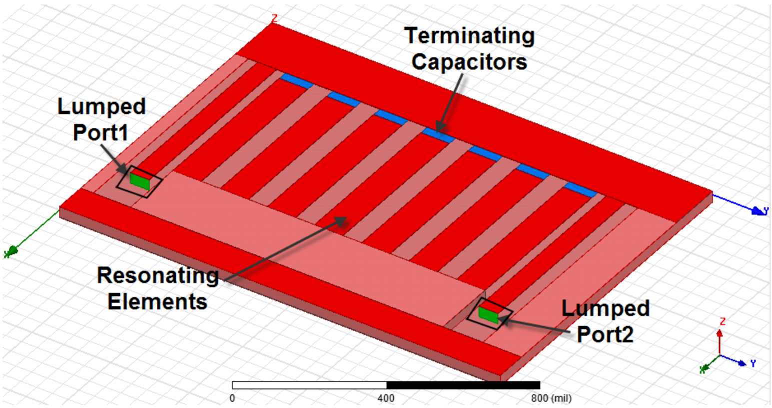

Figure 5.39: HFSS Construction of the Combline Filter

The filter exhibits 7 modes with the first resonance occuring around 1.4GHz; this is the lowest frequency mode and it occurs as the currents in the resonating elements are flowing in the same direction.
The dimensions of the filter were computed using the formulas presented in Section 4.1.3 via a simple Matlab routine, listed in Appendix D. Key filter design parameters are documented in Table 5.4. The PCB layout and corresponding schematics for the fixed-frequency combline filter are presented in Fig. 5.41.

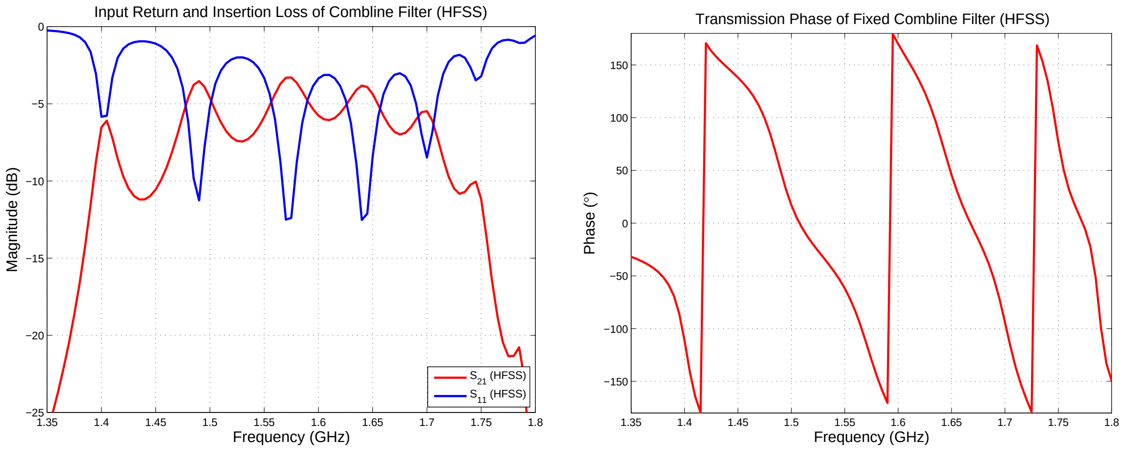

(a) Insertion and Input Return Loss (b) Transmission Phase

Figure 5.40: Magnitude and Phase Response of the Combline Filter (HFSS)

Filter Parameter	**Value**
Resonator Element Length	456 mils
Resonator Element Width	90 mils
Intra-Resonator Spacing	60 mils
Feed Width	60 mils
Feed-Resonator Spacing	30 mils
Copper Trace Thickness	1.4 mils
Board Dielectric Thickness	35.4 mils
Board Dielectric ε_r	4.4

Table 5.4: Combline Filter Parameters

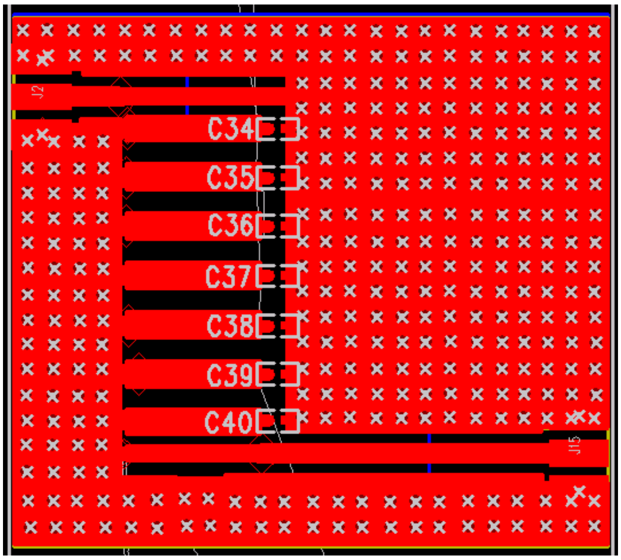

(a) PCB Layout

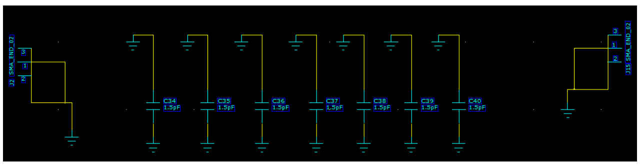

(b) PCB Schematics

Figure 5.41: PCB Implementation of the Fixed Frequency Combline Filter

The tunable combline filter is implemented with the M/A-COM MA4ST1230 [166] varactor diodes. The PCB layout and corresponding schematics for the tunable combline filter are presented in Fig. 5.42. The maximum capacitance value of each diode at low bias is

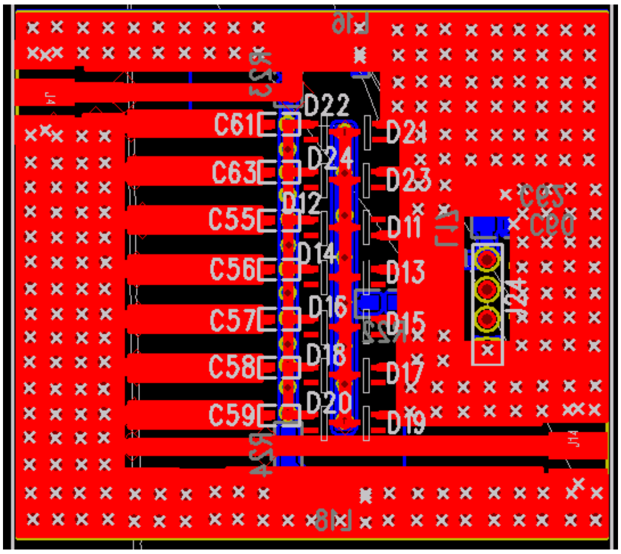

(a) PCB Layout

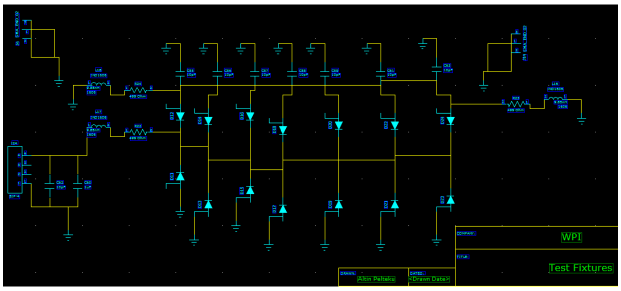

(b) PCB Schematics

Figure 5.42: PCB Implementation of the Tunable Combline Filter

$\approx$ 10pF, while the minimum capacitance value, achieved with higher reverse bias, is specified to be $\approx$ 2.5pF. In series with a blocking capacitor of 10pF, the combined capacitance range can be $3.33 \rightarrow 1.11$pF.

5.5.3 Dielectric Filter

In addition to the combline filter presented above, a bandpass dielectric filter is utilized to provide a sharper phase response around the center frequency. Two commercial off-the-shelf filters, namely TOKO's 4DFA-1575B [158], have been mounted onto a PCB with layout and corresponding schematics shown in Fig. 5.43.

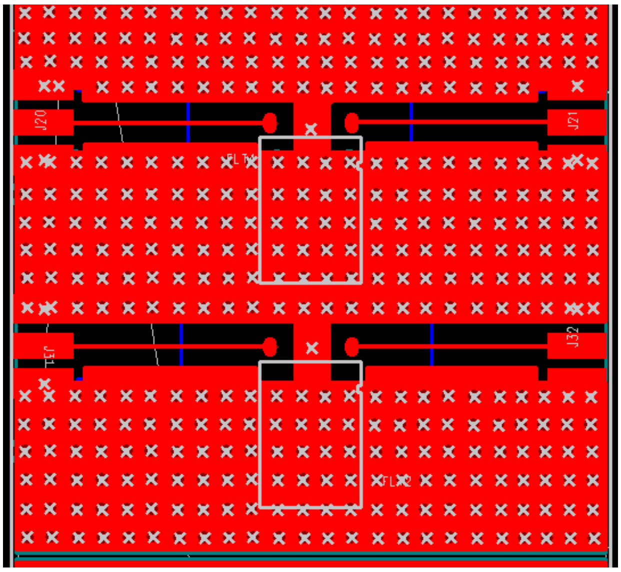

(a) PCB Layout

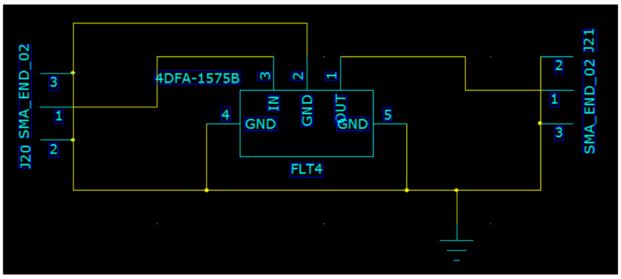

(b) PCB Schematics

Figure 5.43: PCB Implementation of the Dielectric Filter

5.5.4 Design of Voltage Variable Attenuators

The chosen voltage variable attenuator design is based on the Hittite part HMC346MS8G and much of the analysis is summarized from reference [168]. The GaAs absorption type attenuator makes use off-chip components to maintain constant 50Ω impedance matching. The attenuator IC along with the off-chip circuitry is depicted in Fig. 5.44. A traditional,

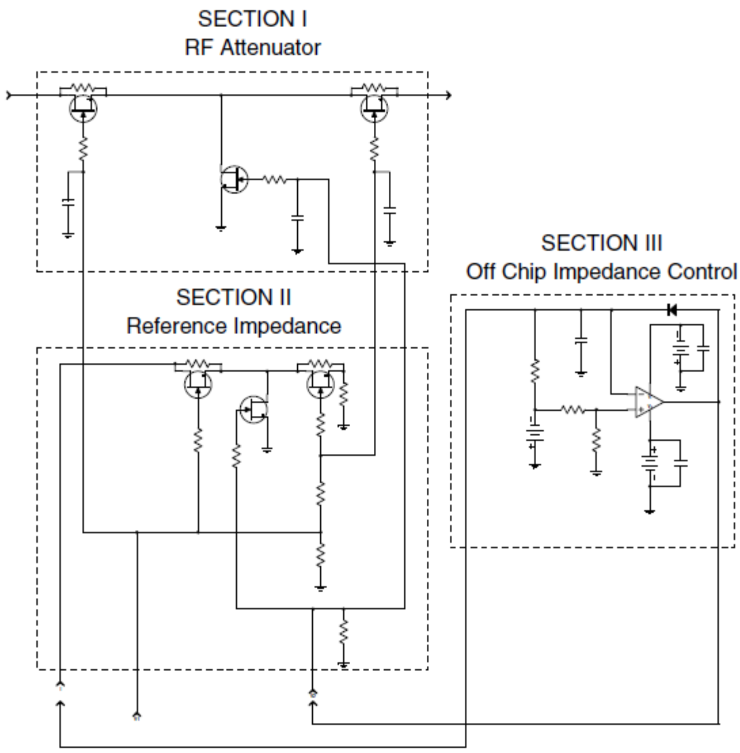

Figure 5.44: Variable Attenuator Design (Reproduced from [168])

series-shunt, T-type network utilizes GaAs FETs to vary the attenuation of an incoming signal; fixed 50Ω parallel to the FET devices improve matching at higher attenuation states. The internal reference section, with a characteristic impedance of 500Ω, helps in maintaining an optimal ratio between the control voltages to the series and shunt FETs of the RF attenuator. An impedance control circuitry uses an OpAmp with negative feedback that adjusts the voltage of the shunt FET devices, to both the RF and reference attenuators, so as to maintain a 500Ω impedance looking into its inverting input. The 10 : 1 impedance ratio between the reference and RF attenuator enables the RF attenuator to maintain 50Ω matching for all attenuation states. The HMC346MS8G part and devices have been mounted on a PCB with layout and corresponding schematics shown in Fig. 5.45. The off-chip THS4031 high-speed OpAmps [169] operate with ±5V supplies which are filtered by various bypass capacitors.

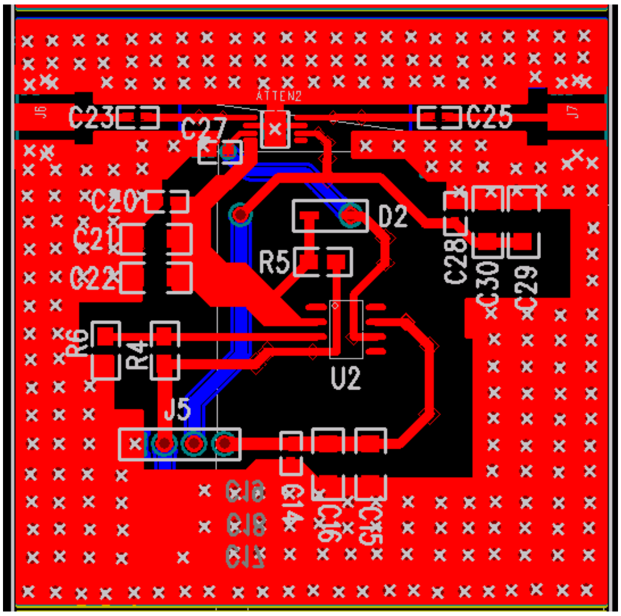

(a) PCB Layout

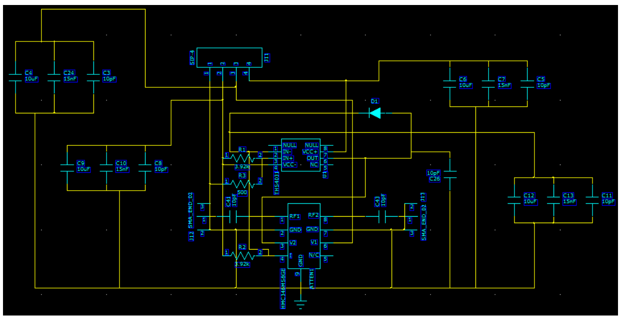

(b) PCB Schematics

Figure 5.45: PCB Implementation of the Voltage Variable Attenuator

5.5.5 Reflection Type Phase Shifters

The phase shifter utilizes a microstrip branchline coupler and anti-series varactor diodes, MA4ST1230, as reflective loads. The varactors are biased by connecting the center tap to a tuning voltage via an RF choke and resistor. The reflection type phase shifter PCB layout and corresponding schematic are shown in Fig. 5.46. The varactors achieve a maximum to

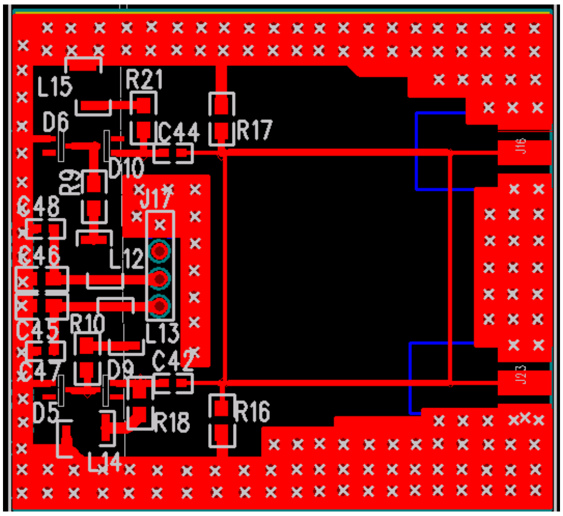

(a) PCB Layout

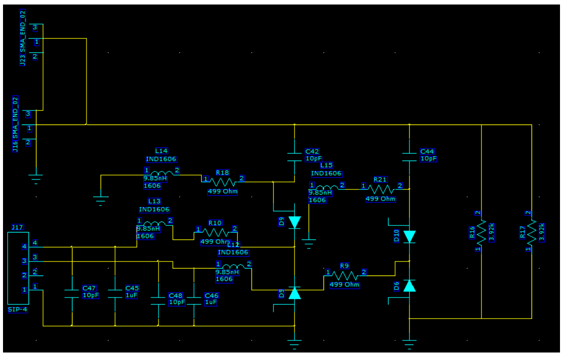

(b) PCB Schematics

Figure 5.46: PCB Implementation of the Reflection Type Phase Shifter

minimum capacitance ratio of $\approx 4:1$ and are connected to the coupler terminals via 10pF capacitors. A DC path to ground for all varactor terminals is provided via large resistors.

Chapter 6

Test Results

In order to evaluate the LNA and the phase-cancellation system three test categories are recognized:

1. Functionality tests of the LNA. The device operates under optimum biasing conditions and its performance is evaluated in terms of typical measurements such as s-parameters, noise figure and nonlinearities.

2. LNA IC system performance tests. Common mode rejection is studied as a function of amplitude and phase mismatches and measurements are performed while varying system parameters.

3. Complete system tests. The performance of the system, including the bandpass filter and the phase delay network, is recorded while emulating suitable interferer and SOI scenarios.

In addition, peripheral devices connected to the LNA IC in system level tests are separately evaluated. The following sections present the system configuration and equipment used, as well as a discussion of test results.

6.1 Peripherals

A general depiction of the test equipment and configuration for measuring S-parameter response of the peripherals is shown in Fig. 6.1 utilizing the HP8722ET Network Analyzer

(NA). The network analyzer has been calibrated up to the sma connectors using SOLT

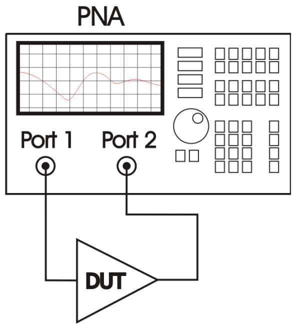

Figure 6.1: S-parameter Measurement of the Peripherals

standards from Agilent's 85052D calibration kit. The list of equipment used to evaluate the performance of the different peripherals is shown in Table 6.1.

Part Number	**Equipment Description**	**Purpose**
HP8722ET	Two Port Network Analyzer	S-parameter Characterization
85052D	NA Calibration Kit	S-parameter Calibration
PS2521G	Power Supply	Up to 6V and 12V Voltage Supplies

Table 6.1: Equipment used for Testing Peripheral Devices

6.1.1 Variable Attenuators

The magnitude and phase responses of the voltage variable attenuators (VVAs) are shown in Fig. 6.2 and Fig. 6.3. The phase response is evaluated based on the absolute and relative phase shift, which uses minimum attenuation as the baseline measurement. Maximum variation on the magnitude response is $<$ 4dB over the frequency range. The variation is highest at low control voltage levels which indicates that the response is affected by the parasitics and input match of the board and at higher attenuation levels it flattens out and approaches the response of the attenuator ICs that can be found in the datasheet for the HMC346MS8G [167]. The relative phase shift between different voltage levels tracks

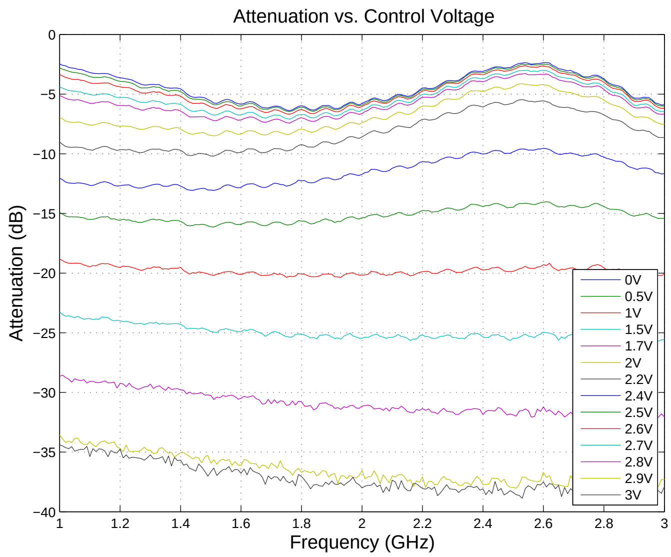

Figure 6.2: Magnitude Response for Different Control Voltages

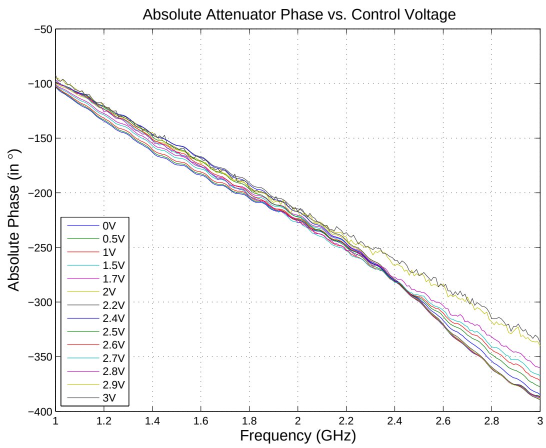

(a) Absolute Phase Shift vs. Control Voltage

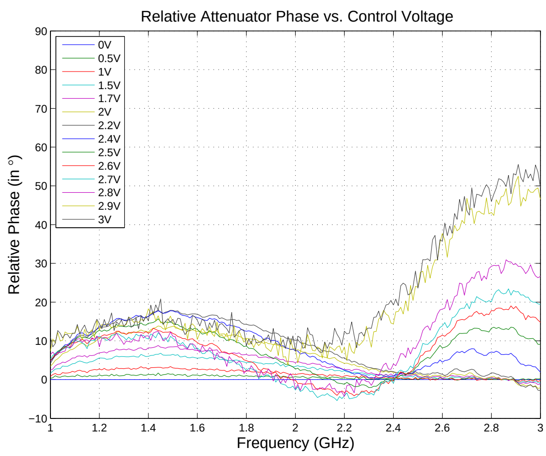

(b) Relative Phase Shift vs. Control Voltage

Figure 6.3: Voltage Variable Attenuator Phase Response

well that of the attenuator ICs. The attenuators are not phase compensated so there are significant differences between low and high attenuation levels, however, the system implementation anticipates low amplitude mismatches, which should not cause significant phase imbalances. Since two variable attenuators were employed during testing, it is important to observe differences between their S_{21} responses. Magnitude and phase differences at minimum and maximum attenuation are presented in Fig. 6.4(a) and 6.4(b). The two

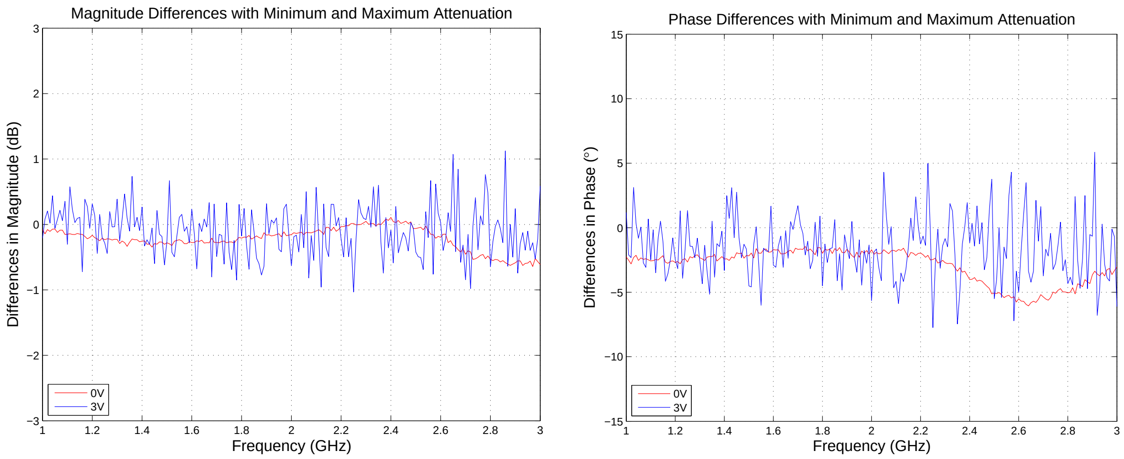

(a) Mag. Differences at Min and Max Attenuation (b) Phase Differences at Min and Max Attenuation

Figure 6.4: Differences in $|S_{21}|$ and $\angle S_{21}$ between two Attenuators

attenuators agree within $\pm 1dB$ and $\pm 7°$ throughout the frequency range with worst case mismatches occuring at high attenuation levels. Within a narrow band these mismatches are overcome by fine tuning the control voltages of the attenuators and phase shifters.

6.1.2 Phase Shifters

Measurements of the magnitude and phase response, respectively, are shown in Fig. 6.5 and 6.6 for the reflection type phase shifter. Relative phase shift using 0V control voltage as the baseline is shown in Fig. 6.6(b). As observed from the plots, certain frequency bands, such as between $2 - 2.4$GHz, are more optimal in providing a wider phase shift range. The behavior exhibits a small resonance starting around 1.8GHz and shifting to higher frequencies when higher control voltages are applied; this introduces relatively high insertion

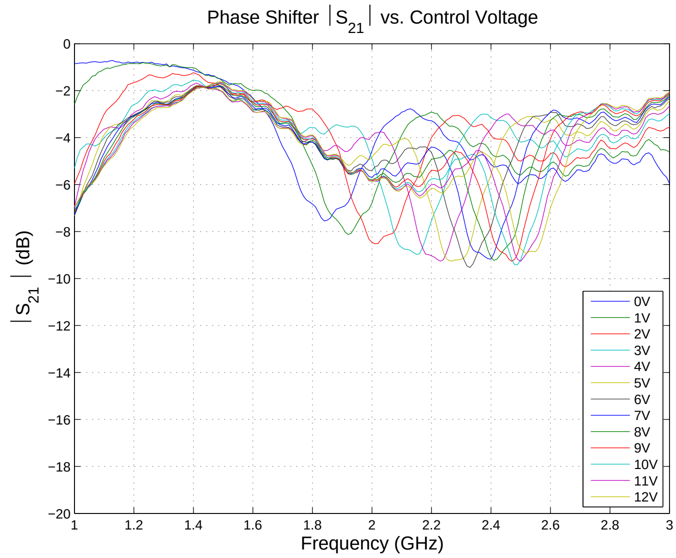

Figure 6.5: Voltage Variable Phase Shifter Magnitude Response

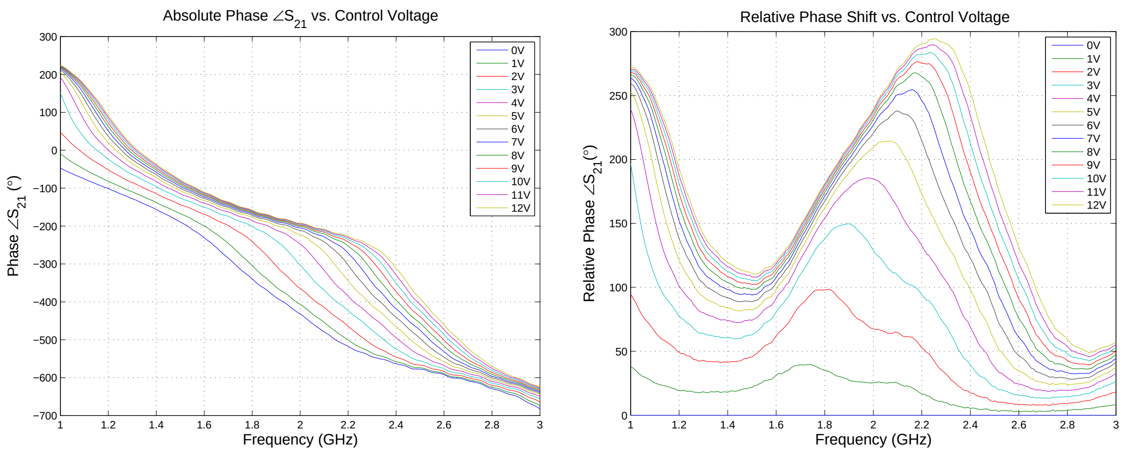

(a) Absolute Phase Shift

(b) Relative Phase Shift

Figure 6.6: Voltage Variable Phase Shifter Phase Response

loss $|S_{21}| \simeq 8dB$ in transmission. Ideally, the phase shifter would provide flat broadband magnitude and phase response; more broadband implementations introduce more complexity to the circuit and may require significantly more PCB area [161]. Nevertheless, the phase shifter can be utilized to provide moderate phase shifts within a narrow band with limited control voltage range applied. In addition, with more modeling and careful layout techniques the resonance can be eliminated.

6.1.3 Hybrids

The input and output reflection coefficients for the 180° hybrid, model 4010180, are shown in Fig. 6.7(a) and 6.7(b), respectively. The plots show all four ports of the hybrid

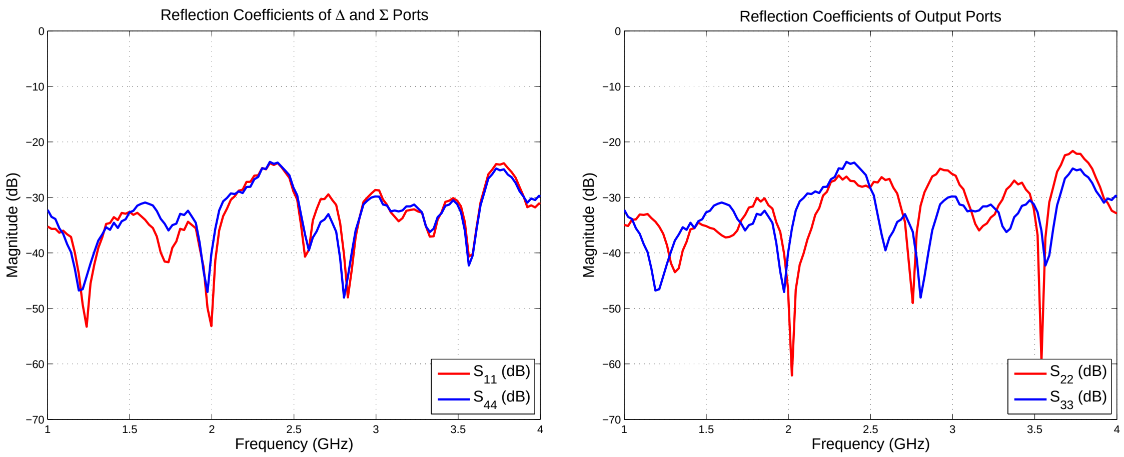

(a) Differential (Δ) and Common-Mode (Σ) Ports (b) Output Ports

Figure 6.7: Return Losses of all four Hybrid Ports

are well-matched to 50Ω; all reflection coefficients are measured to be below -20dB for the band of interest. Figure 6.8(b) shows the amplitude and phase mismatches between the two outputs with the hybrid driven differentially, while Fig. 6.8(a) shows the amplitude responses of each differential port. Plots show that within the band of interest amplitude mismatches are expected to be below ± 0.6dB and phase mismatches below $\pm 2.5°$ with one large exception at 1GHz where phase imbalance approaches $\sim 6.5°$. This imbalance reflects the lower end of the operating band for the hybrid, specified as $1 - 18$GHz in the datasheet [170].

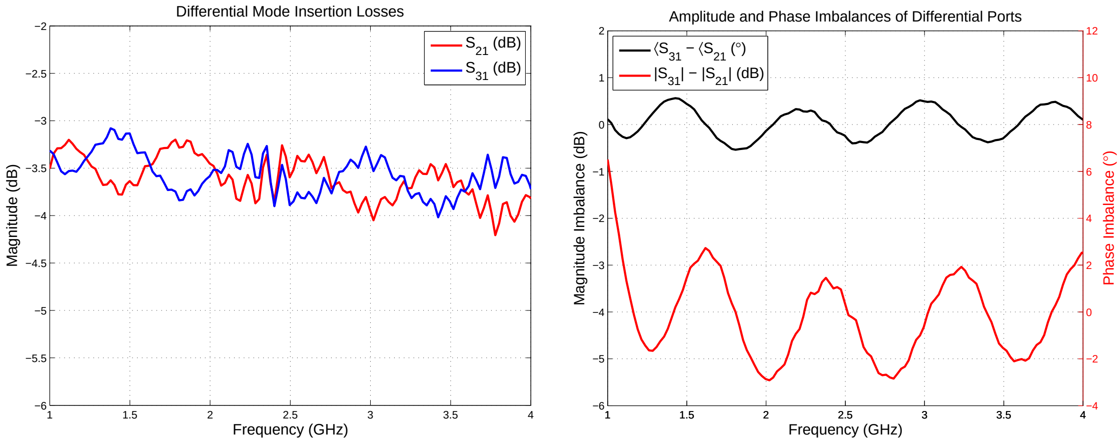

(a) Insertion Losses, each Port

(b) Amplitude and Phase Imbalances

Figure 6.8: Insertion Losses and Imbalances with Differential Stimuli

6.1.4 Filters

Magnitude and phase response for the fixed combline filter are presented respectively in Fig. 6.9 and 6.10. As can be seen from the plots, there is a slight shift in frequency in

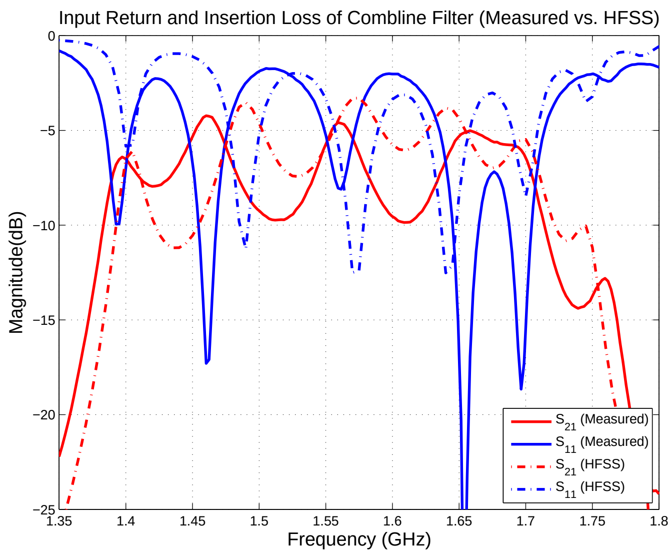

Figure 6.9: Magnitude Response of the Fixed Combline Filter (Measured vs. Model)

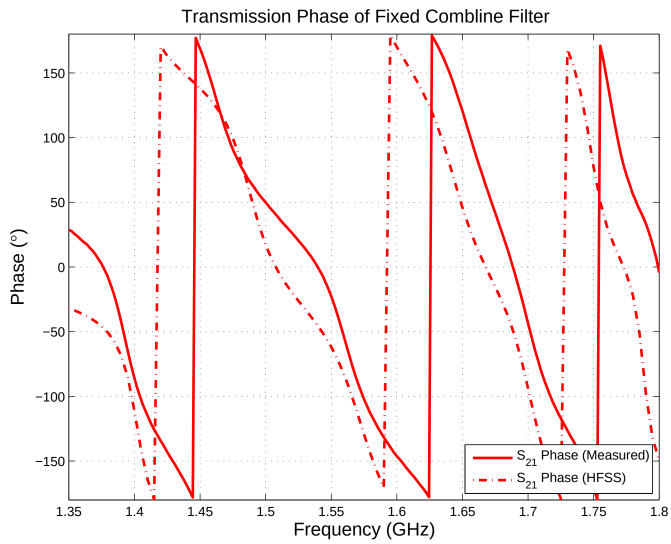

Figure 6.10: Phase Response of the Fixed Combline Filter (Measured vs. Model)

measured data as compared to the model; this shift can be attributed to an increase in either the resonator inductance or terminating capacitance. Possible sources of such discrepancy include the multitude of parasitics present, departures from ideal modeling due to capacitor tolerances as well as imperfect PCB manufacturing.

Magnitude and phase response for the tunable combline filter are presented, respectively, in Fig. 6.11(a) and 6.11(b). The loaded quality factor of the filter is estimated from these plots to be, depending on tuning voltage, $Q_L \approx$ 25-30. The quality factor has been significantly affected by parasitics, such as the varactor loss and transmission line losses. Typical loss for the MA4ST1230 is on the order of $R_S \sim 0.5\Omega$, according to the datasheet; a quick estimate at 1GHz and 1V reverse bias results in a quality factor for the varactor alone of: $Q_{VAR} \equiv \frac{1}{R\omega_0 C} \cong \frac{1}{0.5\Omega \times 2\pi \times 10^9 Hz \times 8 \times 10^{-12} F} \cong 40$. In addition, transmission line losses are significant when considering the loss tangent of the FR-4 material to be $tan\delta \simeq 0.0165$ [149] at around 1GHz; this results in a dielectric quality factor of $Q_d = \frac{1}{tan\delta} \simeq 60.6$. The varactor losses and transmission line losses fundamentally limit the maximum quality factor that can be obtained with such type of resonator. One marked improvement can be achieved by using varactors with lower series resistance and dielectric material with a lower

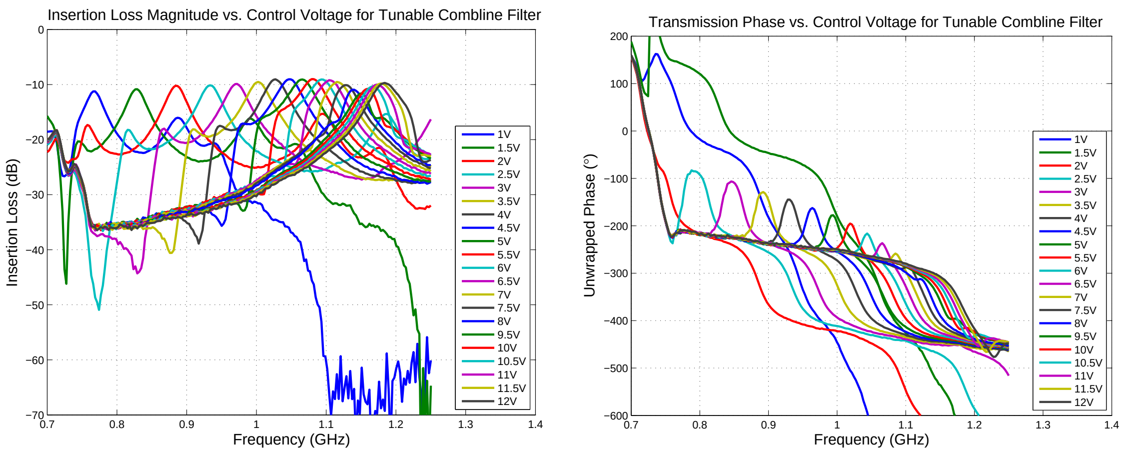

(a) Magnitude Response

(b) Phase Response

Figure 6.11: Magnitude and Phase Response of the Tunable Combline Filter

$tan\delta$; both options result in higher PCB manufacturing cost.

The magnitude and phase responses for the dielectric filter are shown in Fig. 6.12 and 6.13. The center frequency of the filter is estimated from measured data to be $f_0 \cong 1565$MHz, while the upper and lower -3dB breakpoints are $f_u \cong 1589$MHz and $f_l \cong 1521$MHz, respectively. Hence, the estimated bandwidth is $BW \cong 68$MHz, resulting in a loaded quality factor of the filter $Q_L \approx 23$. From the corresponding datasheet [158] loaded Q is estimated to be $Q_L \approx 30$ so there may be slight degradation due to transmission line losses, similar to the combline filter case.

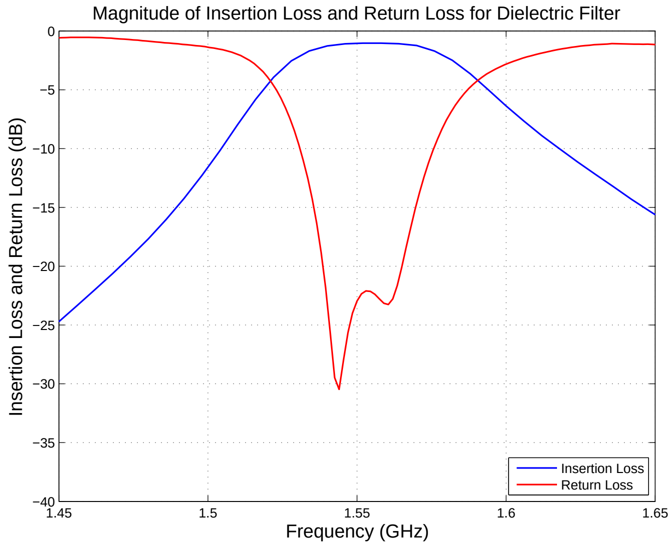

Figure 6.12: Magnitude Response of the Dielectric Filter

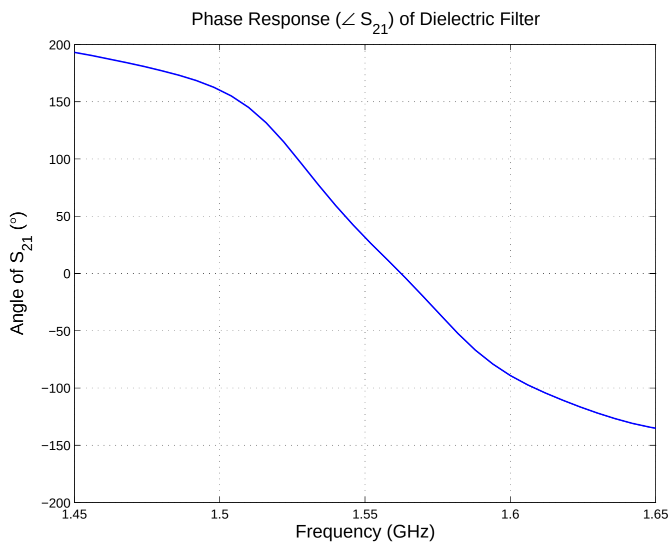

Figure 6.13: Phase Response of the Dielectric Filter

6.2 LNA IC Functionality Tests

This section presents de-embedded LNA IC performance results obtained with a Cascade Microtech Summit 12000 probe station. The various instruments used in testing the LNA are shown in Table 6.2.

Part Number	**Equipment Description**	**Purpose**
Summit 12000	Cascade Probe Station	On-wafer Probing
E8364B	Two Port Network Analyzer	S-parameter Characterization
E4446A	PSA Spectrum Analyzer	Spectrum Measurement
E8257D	PSG Signal Generator	RF Signal Source
N8975A	NF Analyzer	Noise Figure Measurement
4010180	1-18 GHz Hybrid	Differential, Common-Mode Stimuli
40A-GSG-125 -D-250	125um Pitch, Dual RF Probe	On-wafer Probing
N4681-60001	ECal Module	Electronic Calibration
CS-2-125	GSGSG Calibration Kit	On-wafer Calibration

Table 6.2: Equipment used for Functionality Tests of the LNA IC

The layout of the differential LNA with overlaid bondpad names is shown in Fig. 6.14; bondpad names are described in Table 6.3.

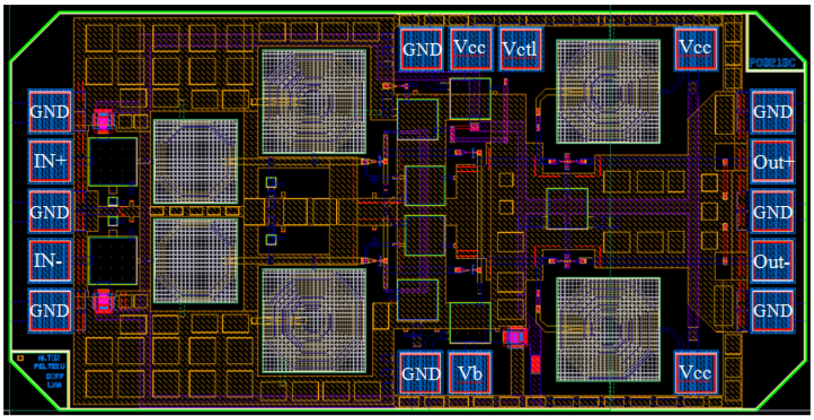

Figure 6.14: LNA IC with Overlaid Bondpad Names

Pad Name	**Description**	**DC Voltage (nominal)**	**Requires DC Block**
GND	Global Ground (input)	0V	No
Vcc	Power supply (input)	2.5V	No
Vb	Cascode Bias (input)	1.8V	No
Vctrl	Bias Control (input)	2.5V	No
IN+	Positive RFin Reference (input)	N/A	No
IN-	Negative RFin Reference (input)	N/A	No
OUT+	Positive RFout Reference (output)	N/A	Yes
OUT-	Negative RFout Reference (output)	N/A	Yes

Table 6.3: Differential LNA with Overlaid BondPad Names

6.2.1 Small Signal S-parameters

On-wafer, mixed-mode s-parameters were measured with a two port network analyzer and 180° hybrids with the measurement setup depicted in Fig. 6.15. A snapshot of the

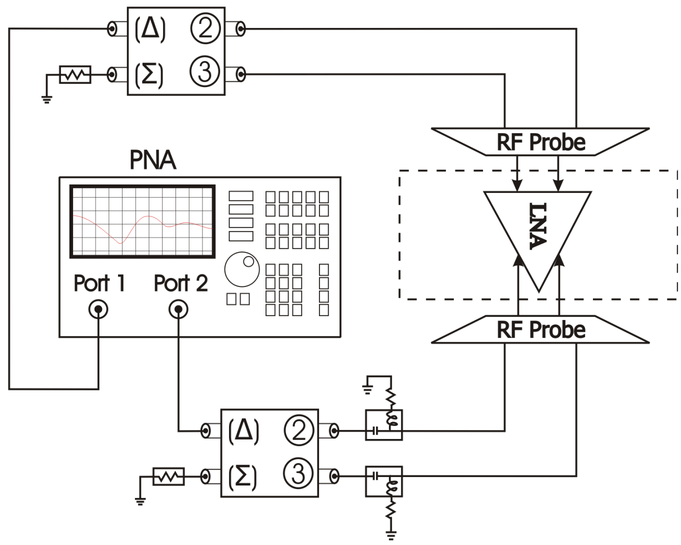

Figure 6.15: Mixed Mode S-parameter Experimental Setup

IC die being probed is shown in Fig. 6.16. The RF probes are situated on the left and the right bondpads, while the DC probes are positioned on the top and bottom pads. The probe pitch used throughout is 125μm and the RF probes use the dual ground-signal-ground (GSG) configuration or GSGSG. Making contact with the 125um, GSGSG dual RF probes in the passivation opening area is illustrated in Fig. 6.17. In order to deembed experimental data, an SOLT (short-open-load-thru) calibration with Ecal module was performed up the hybrids. Data was then normalized using on-wafer thru standards, which takes into account losses due to hybrids, probes and the connection between them.

Gain and input return loss for the differential-mode and common-mode, respectively, are shown in Fig. 6.18(a) and 6.18(b); RLC extracted (simulated) results are overlaid for comparison. As compared to extracted results the gain has degraded on-average $\approx 1 - 2$ dB, with the highest discrepancy occuring at 3GHz while matching well up to 1GHz. Considering no electromagnetic (EM) package, such as Momentum, was employed at the

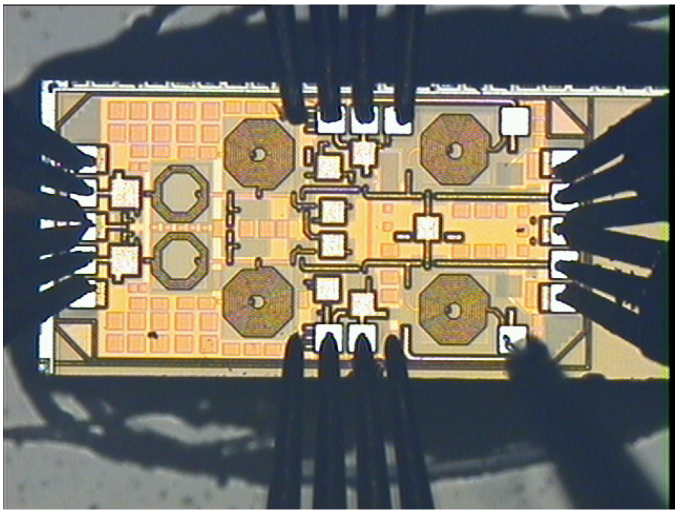

Figure 6.16: Probing of the LNA Die

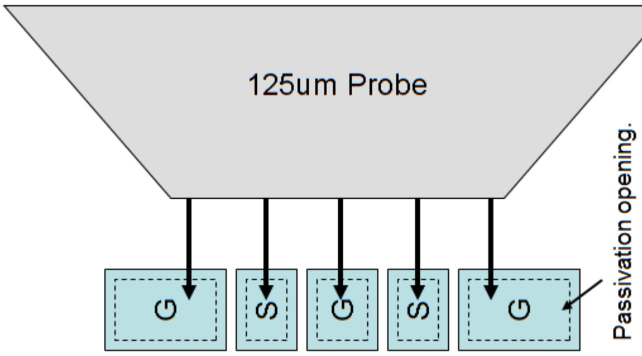

Figure 6.17: Illustration of Contacting the BondPad with the Dual RF Probe

time of modeling this amplifier relatively moderate to significant discrepancies are expected. The extracted results use a lumped-element RLC representation so no wave effects are accounted for. In addition, mutual inductance and substrate losses were not considered either due to prohibitively large netlists or package availability. In addition, the model closely tracks the measured data with regard to input return losses and common-mode gain; one notable discrepancy appears at low frequencies in the common-mode response which degrades due to the operating band of the hybrid.

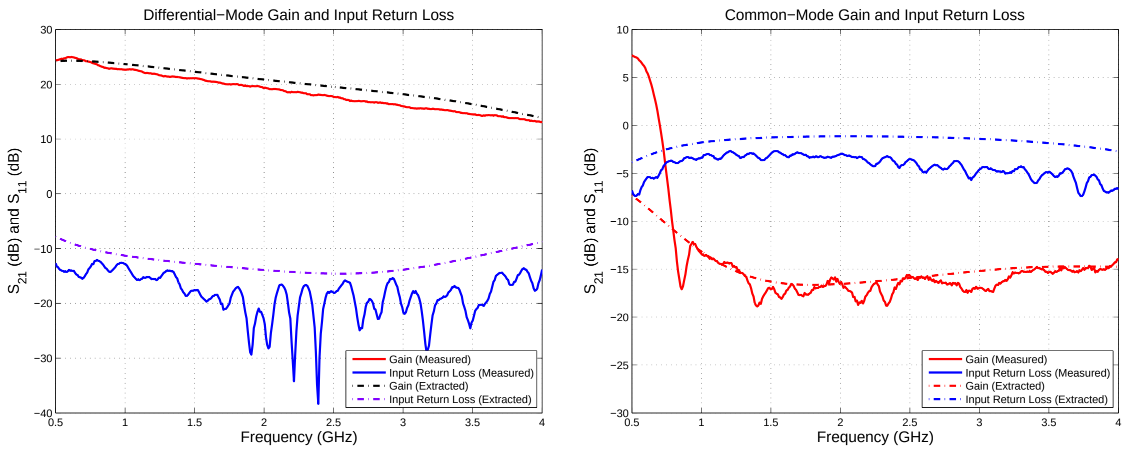

(a) Differential-Mode

(b) Common-Mode

Figure 6.18: Gain and Input Return Loss (Measured vs. Extracted)

The resulting CMRR along with mode conversion gains are presented in Fig. 6.19. As seen from the graphs, extracted results are close to measured data with regard to CMRR while mode conversions gains are poorly predicted. The graph substantiates the claim that the method chosen for measuring mixed-mode s-parameters (i.e. using hybrids) does not support mode-conversion characterization.

The output return loss and reverse isolation for the differential-mode and common-mode, respectively, are shown in Fig. 6.20(a) and 6.20(b). Similar to the differential-mode case the extracted results are close to measured data with regard to output return loss while reverse isolation measurements seem to be limited by calibration accuracy. Probe crosstalk can be another factor that defines a measurement noise floor, which can be as high as -60dB for a probe separation of 1mm in silicon substrates [102].

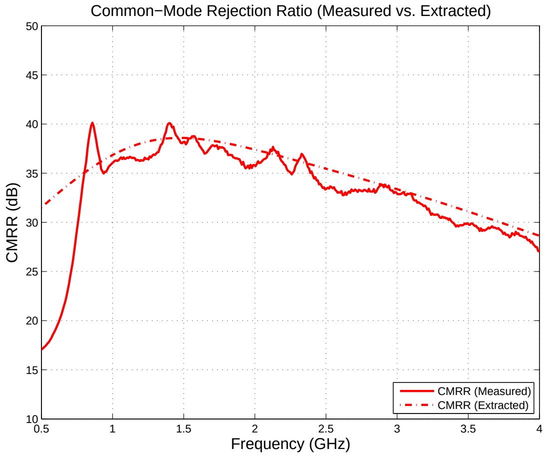

(a) Common Mode Rejection Ratio

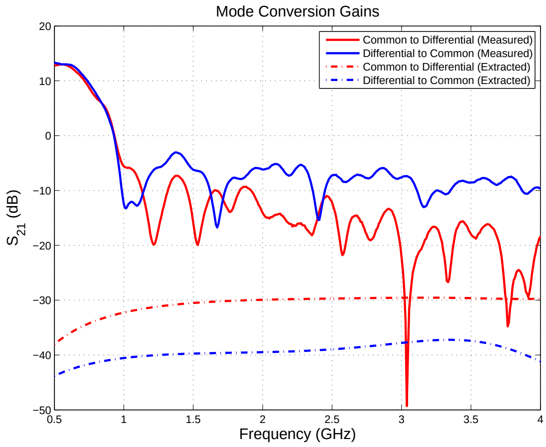

(b) Mode Conversion Gains

Figure 6.19: Measured vs. Extracted CMRR and Mode Conversion Gains

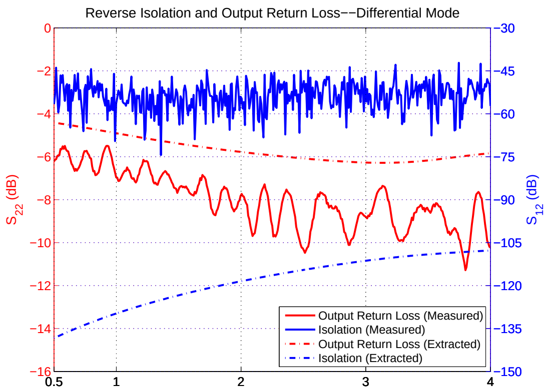

(a) Differential-Mode

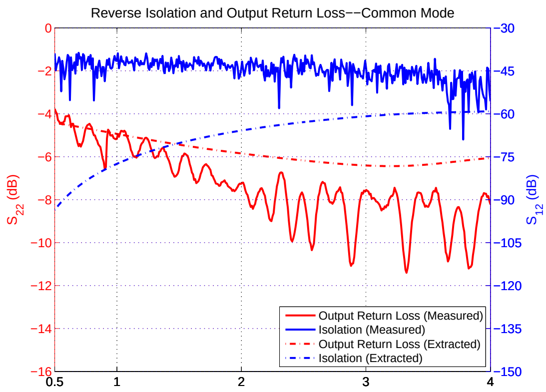

(b) Common-Mode

Figure 6.20: Reverse Isolation and Output Return Loss (Measured vs. Extracted)

6.2.2 Noise Figure

Measurement setup for the differential noise figure is depicted in Fig. 6.21. As in the case of mixed mode S-parameters the differential stimuli is generated via the hybrids. Losses in the hybrids, cables and connections are de-embbeded. From the analysis presented in Section 4.3.2 the error in differential NF measurement due to imbalances and finite CMRR of the amplifier is anticipated to be around $0.1-0.3$dB. Differential Noise Figure measurements

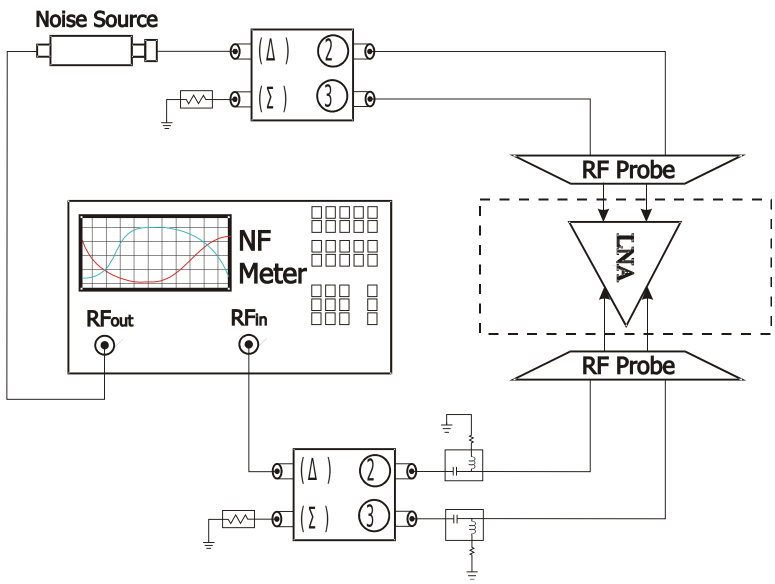

Figure 6.21: Measurement Setup for Differential Noise Figure.

are presented in Fig. 6.22. In addition to the aforementioned level of uncertainty, much of the discrepancy between measured and modeled data can be attributed to the discrepancy found between extracted and measured differential gains of the LNA. This is especially true at higher frequencies where there is significant gain rolloff. Noise figure can be improved at higher frequencies by re-tweaking the design and minimizing parasitic losses at the input while employing EM modeling software to better characterize passive devices, interconnects and transmission lines.

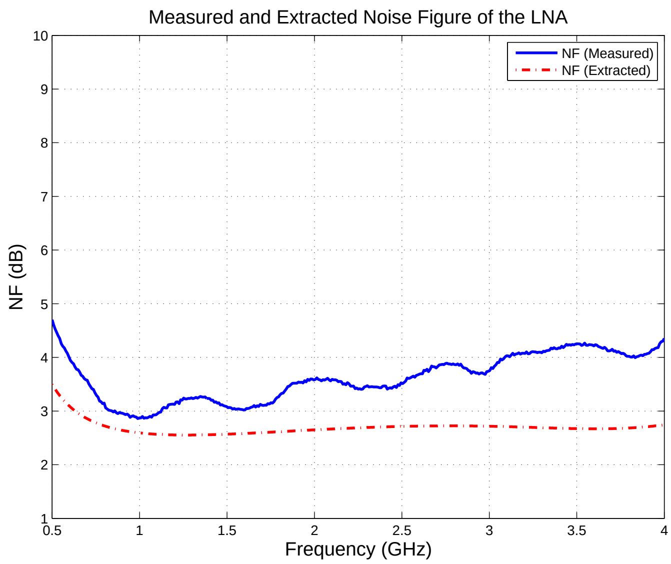

Figure 6.22: Differential Noise Figure.

6.2.3 Nonlinear Performance

The nonlinear behavior of the LNA is characterized by recording the output spectrum while the DUT is driven with a single tone or two closely spaced tones. The power levels of the fundamental and third-order products are recorded versus input power and a collection of data points is used to extrapolate the intersection of the fundametal and distortion lines.

Single Tone Measurements

Measurement setup for characterizing single tone nonlinearity is shown in Fig. 6.23. Experimental data for large signal gain of the amplifier are shown at 1GHz, 2GHz and 3GHz with the results plotted in Fig. 6.24(a). In addition, output powers of the main tone, second and third harmonis are shown in Fig. 6.24(b), 6.25(a) and 6.25(b) for the three aforementioned frequency points.

In general the nonlinear behavior compares well with the extracted simulations documented in Section 5.4.2. Gain is lower at higher frequencies as previously discussed in the mixed-mode s-parameters section; gain at lower input power levels matches with the small-signal gain (S_{21}^{dd}), a check of consistency. A "knee" in the large signal gain is predicted around

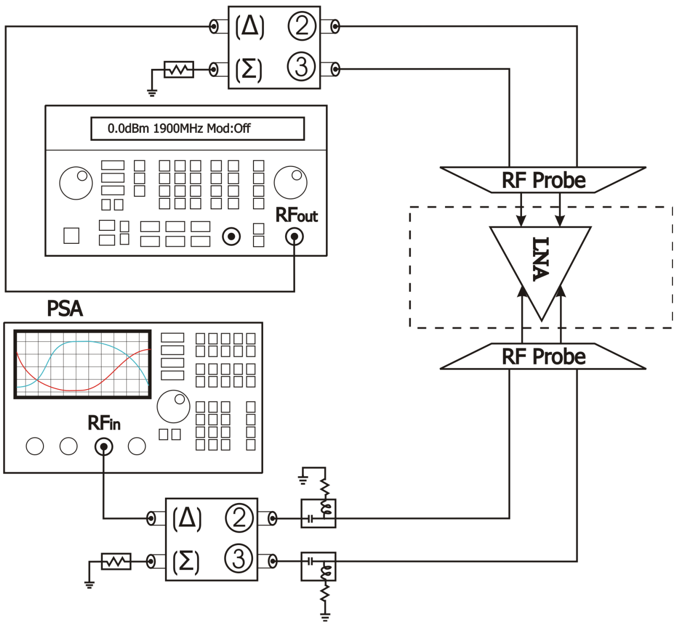

Figure 6.23: Setup for Single Tone Nonlinearity Measurement.

−25dBm which matches predictions with the extracted netlist. In additions, measured data are predicted well in terms of third-order single-tone intercept points, ≈ 10dBm at all frequencies.

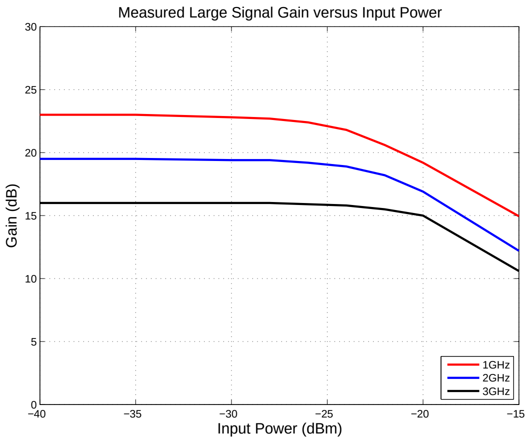

(a) Large Signal Gain

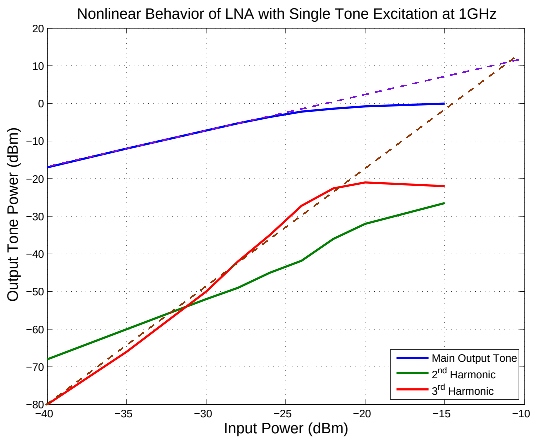

(b) Harmonic Content at 1GHz

Figure 6.24: Large Signal Gain and Harmonic Content at 1GHz (Measured)

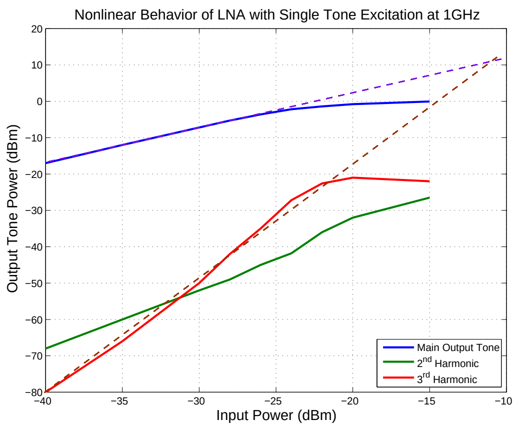

(a) Harmonic Content at 2GHz

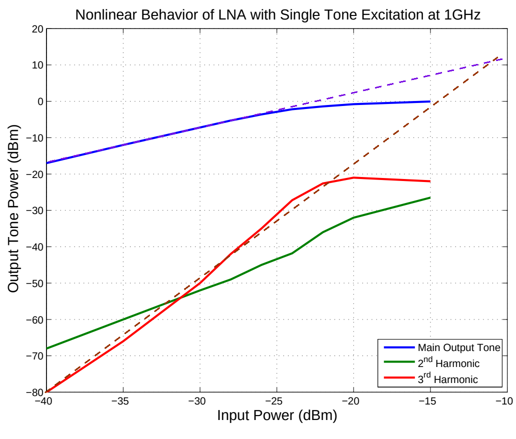

(b) Harmonic Content at 3GHz

Figure 6.25: Harmonic Content at 2 and 3GHz (Measured)

Two Tone Results

Measurement setup for characterizing two tone intercept points is shown in Fig. 6.26. Nonlinear gain and OTOI is recorded at 1, 2 and 3GHz as the input tone power is varied.

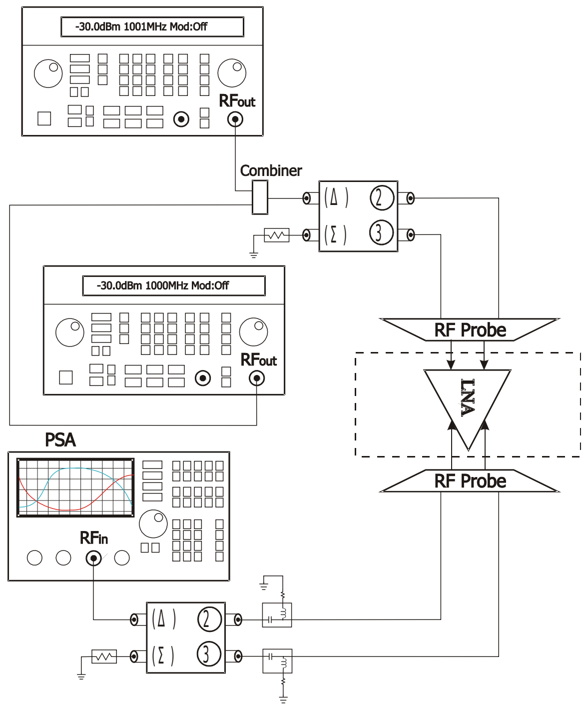

Figure 6.26: Setup for Two Tone Nonlinearity Measurement

Two tone 3^{rd} order intercept point with stimuli centered around 1, 2 and 3GHz are shown in Fig. 6.27(b), 6.28(b) and 6.29(b), while the corresponding large signal gains are shown in Fig. 6.27(a), 6.28(a) and 6.29(a). The tones are centered around the frequencies indicated above with spacing of 1MHz between them. Overall, the extracted model simulations are close to measurements, escpecially with regard to OTOI. At higher frequencies OTOI degrades due to lower gain; any gain discrepancies are explained in section 6.2.1. As in the case of single tone measurements, at low input power levels, large signal gain results approach differential gain measurements acquired with the PNA.

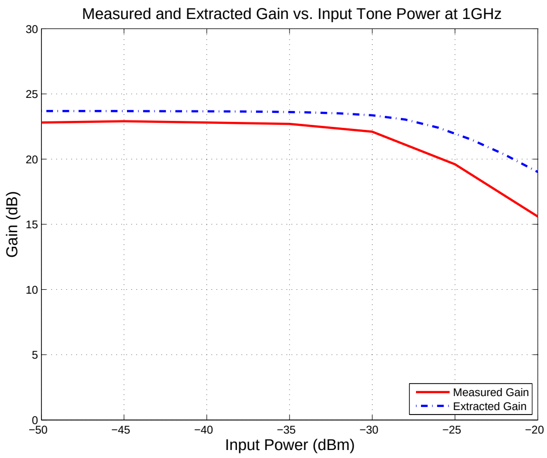

(a) Nonlinear Gain vs. Tone Power at 1GHz

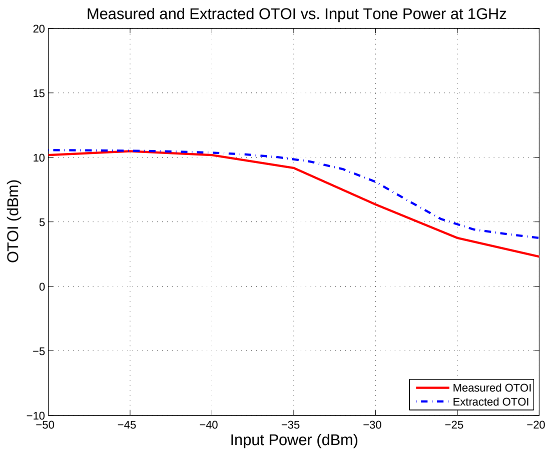

(b) OTOI vs. Tone Power at 1GHz

Figure 6.27: Measured vs. Extracted OTOI and Nonlinear Gain at 1GHz

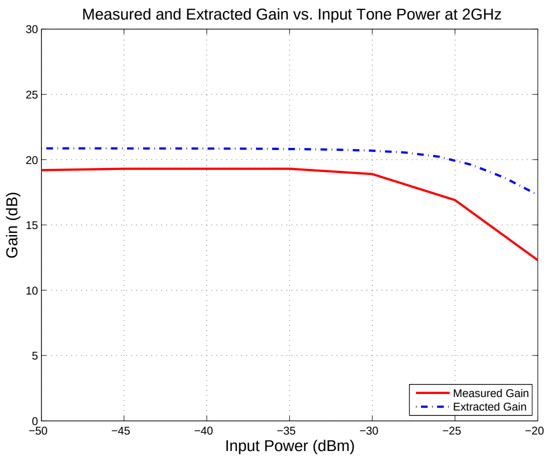

(a) Nonlinear Gain vs. Tone Power at 2GHz

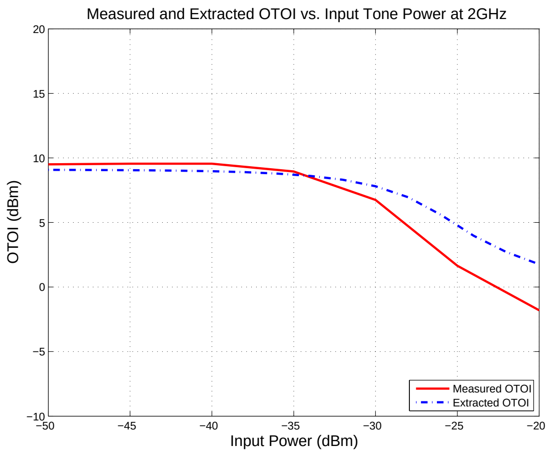

(b) OTOI vs. Tone Power at 2GHz

Figure 6.28: Measured vs. Extracted OTOI and Nonlinear Gain at 2GHz

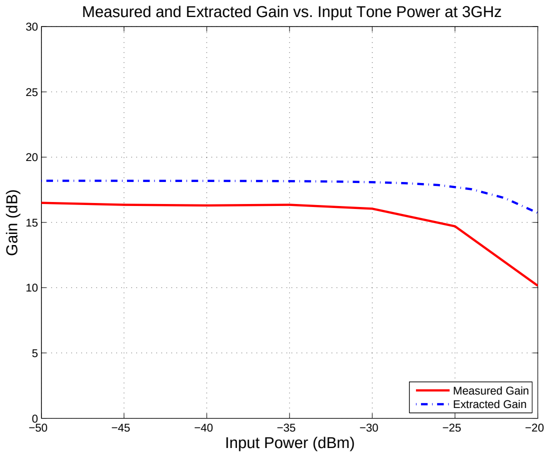

(a) Nonlinear Gain vs. Tone Power at 3GHz

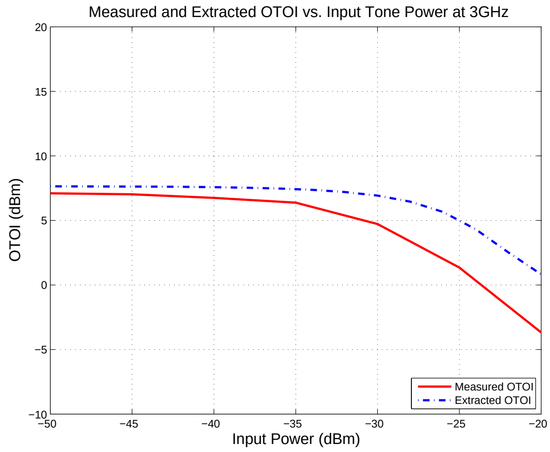

(b) OTOI vs. Tone Power at 3GHz

Figure 6.29: Measured vs. Extracted OTOI and Nonlinear Gain at 3GHz

6.3 LNA System-IC Performance

The aim of the system-IC tests is to examine the performance of the LNA in a similar setup to the phase-cancellation system. Software based predictions were carried out with the harmonic balance tool in ADS and showed that when the interferer is fed equally to the differential inputs of the LNA the rejection at the output is better than 35dB throughout the band. Two tone simulations (SOI and interferer) were carried out to estimate both rejection and nonlinearities as a function of both the signal of interest and interferer input power levels and phase. CMRR suffers when there is a phase shift between the interfering signals fed at the differential inputs and the more critical cases were observed when the amplitudes of the interfering signals at the differential inputs were unequal (even with perfect phase matching).

The following tests plan to provide an environment with an array of different conditions with regards to amplitude and phase offsets, while recording the ability of the amplifier to reject common mode signals. Measurement setup for evaluating the system performance of the LNA IC is shown in Fig. 6.30. The PNA records differential and common-mode gains while phase and amplitude mismatches are varied. Wideband hybrids are used to split and re-combine the signal. The device is biased for optimum operation while peripherals accomplish phase, ϕ, and attenuation, α, fine tuning. A list of instruments used and their purpose is documented in Table 6.4.

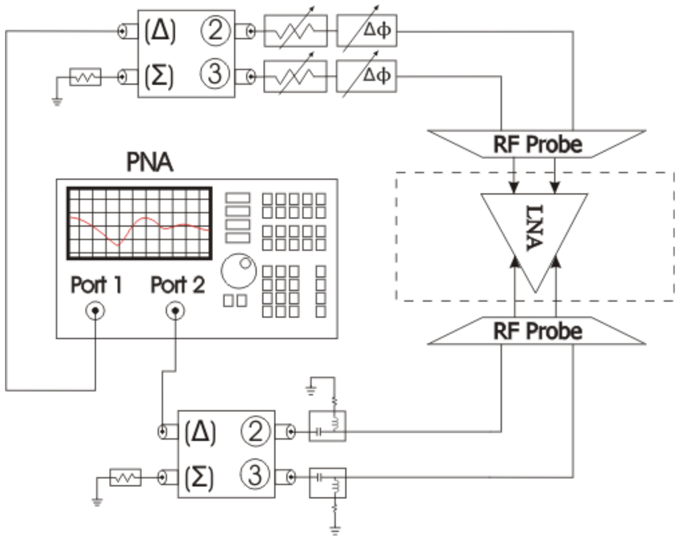

Figure 6.30: Setup for LNA IC System Performance.

Name	**Equipment Description**	**Purpose**
Summit 12000	Cascade Probe Station	On-wafer Probing
E8364B	Two Port Network Analyzer	S-parameter Characterization
4010180	$1 - 18$GHz Hybrid	Differential, Common-Mode Stimuli
Atten. PCB	Variable Attenuator	Compensating Amplitude Mismatches
9428A	1-18 GHz Phase Shifter	Compensating Phase Mismatches

Table 6.4: Equipment used for Characterizing the LNA System-IC Performance

Gain as a function of bias current is presented in Fig. 6.31. More ripple is seen in measured data at higher bias currents. Such ripples can be caused by VSWR interactions or measurement issues. The probes used for these measurements have beryllium-copper tips which are not ideal for probing silicon ICs (unbeknownst to the author at the time); aluminum pads

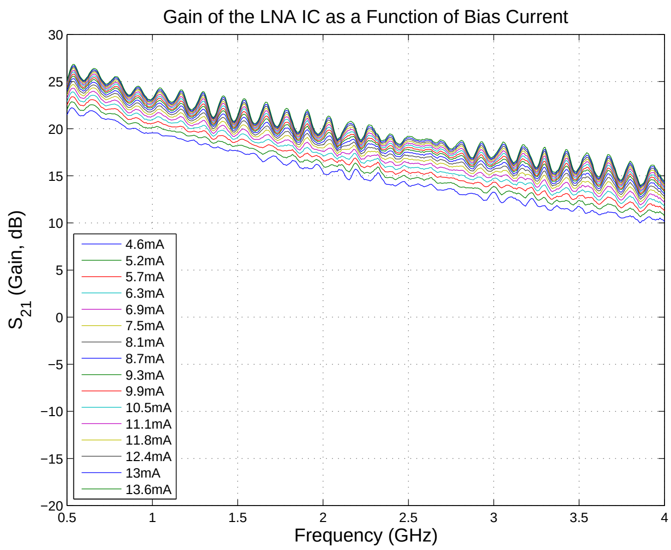

Figure 6.31: Gain as a Function of Bias Conditions.

tend to build up oxide and probe tips must be cleaned after some testing time. As a matter of fact, unexplained intermittent issues were observed when testing several LNA ICs; lifting and re-landing the probes turned a seemingly non-working chip into a functional one.

Evaluating the ability of the design to reject common mode interference was carried out by measuring common mode rejection as phase and amplitude mismatches were varied. The data points were interpolated in MATLAB using the built-in cubic fit; results are presented for the following frequencies: 955MHz in Fig. 6.32(a) with corresponding contour plot in Fig. 6.32(b), 1.55GHz in Fig. 6.33(a) with corresponding contour plot in Fig. 6.33(b), 1.85GHz in Fig. 6.34(a) with corresponding contour plot in Fig. 6.34(b) and 2.4GHz in Fig. 6.35(a) with corresponding contour plot in Fig. 6.35(b).

A similar analysis was carried out in Section 3.4 with ideal amplifier characteristics so the results are numerically different; whereas predictions have a very sharp, nearly infinite, peak in SIR improvement, this is limited in measurements by the common-mode rejection of the setup. Note that the common-mode rejection of the setup is better than that of the amplifier at select frequency points, which may be an indication that the mismatches in the hybrids also play an important role and a better optimum may be found by slight

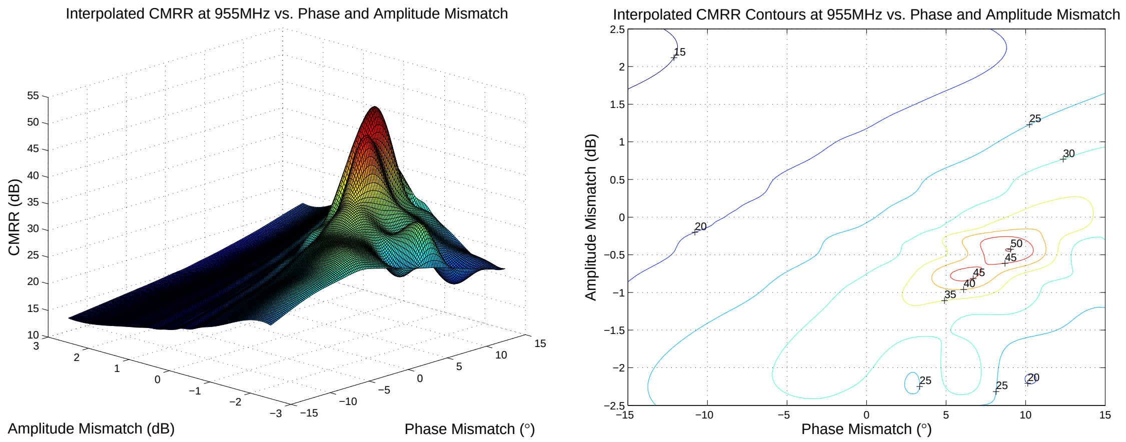

(a) CMRR Surface Plot (b) CMRR Contour Plot

Figure 6.32: CMRR as a Function of Phase and Amplitude Mismatches at 955MHz

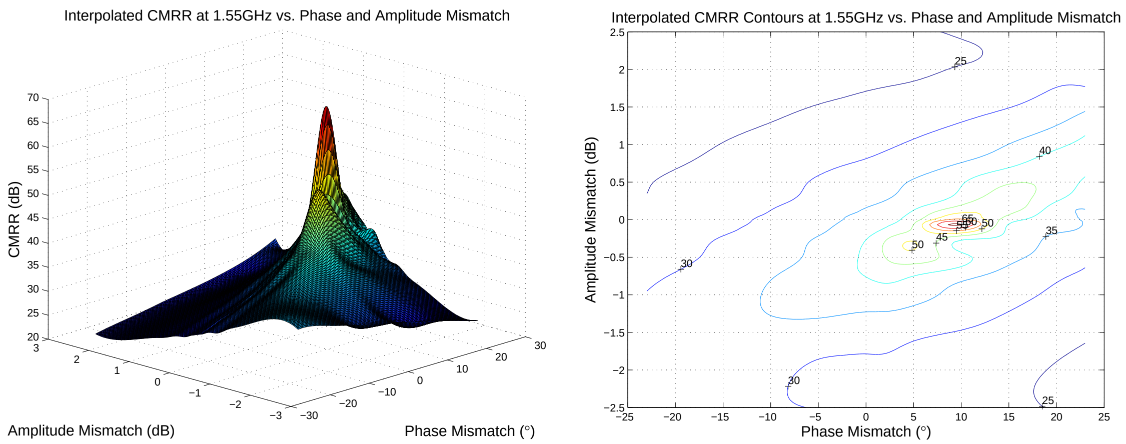

(a) CMRR Surface Plot (b) CMRR Contour Plot

Figure 6.33: CMRR as a Function of Phase and Amplitude Mismatches at 1.55GHz

offset values of amplitude or phase. The hardware provides for wider rejection peaks than simulations and these peaks are not centered around $\Delta\theta = 0$ or $\Delta\alpha = 0$. In addition, there is significant variation with frequency as the rejection depends on the offsets of the systems, including but not limited to hybrids, cable lengths and probe mismatches.

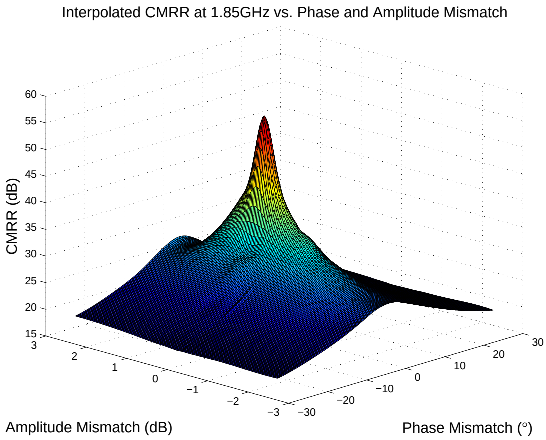

(a) CMRR Surface Plot

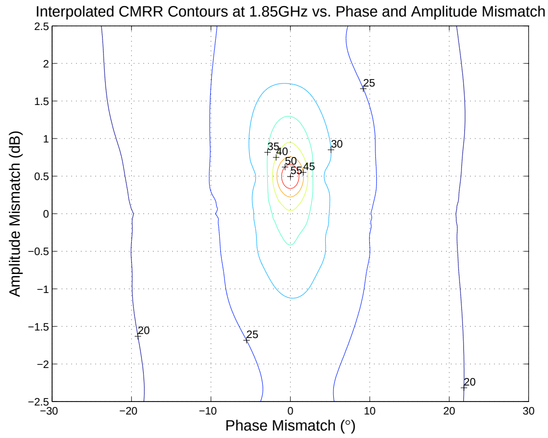

(b) CMRR Contour Plot

Figure 6.34: CMRR as a Function of Phase and Amplitude Mismatches at 1.85GHz

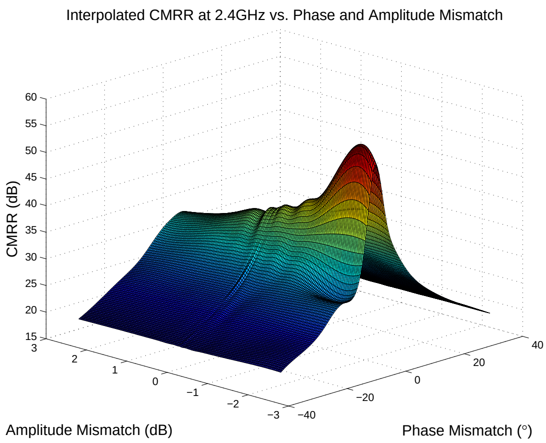

(a) CMRR Surface Plot

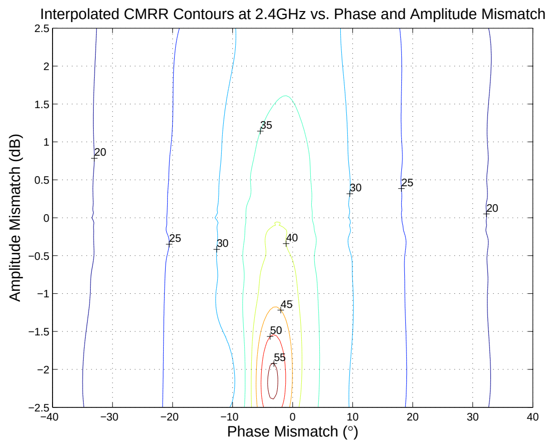

(b) CMRR Contour Plot

Figure 6.35: CMRR as a Function of Phase and Amplitude Mismatches at 2.4GHz

The optimum phase and amplitude offsets for maximum attainable CMRR are found through an exhaustive search; results are plotted for the whole test-band in Fig. 6.36. Maximum CMRR is higher than 40dB with few exceptions, one notably around 2.2GHz; it is possible that at such frequencies optimum amplitude and phase offsets are outside of the

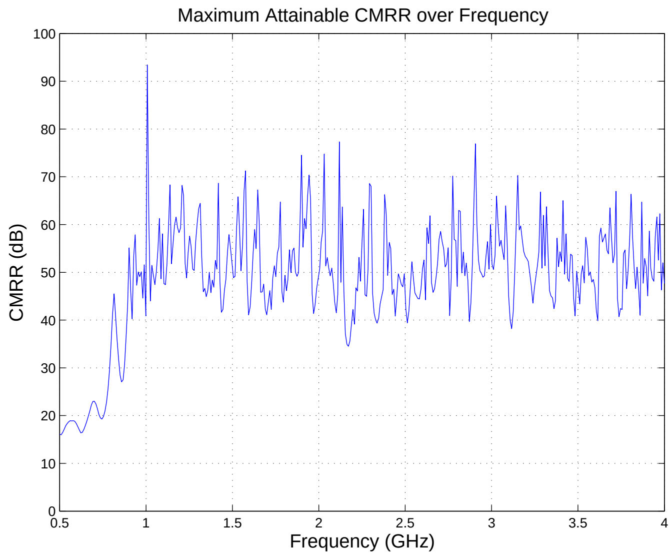

Figure 6.36: Maximum Attainable CMRR throughout the Test Range.

tested ranges. In the case that the applied setup is different in terms of rejection profile from what is tested, the system should be able to find, through an exhaustive search, the optimum set of amplitude and phase offsets for a desired frequency range.

6.4 Full-System Tests

This section presents tests conducted with the complete phase-cancellation system configuration including the differential LNA, attenuators, filters and phase shifters.

6.4.1 Experimental Setup

With the full characterization of the LNA chip completed, system tests are in order to evaluate the performance of the phase-cancellation system as a whole. The goal of these tests is to record the SINR improvement as a function of system parameters, and draw comparisons with the predictions in Section 3.3. Measurement setup for conducting full-system tests is shown in Fig. 6.37.

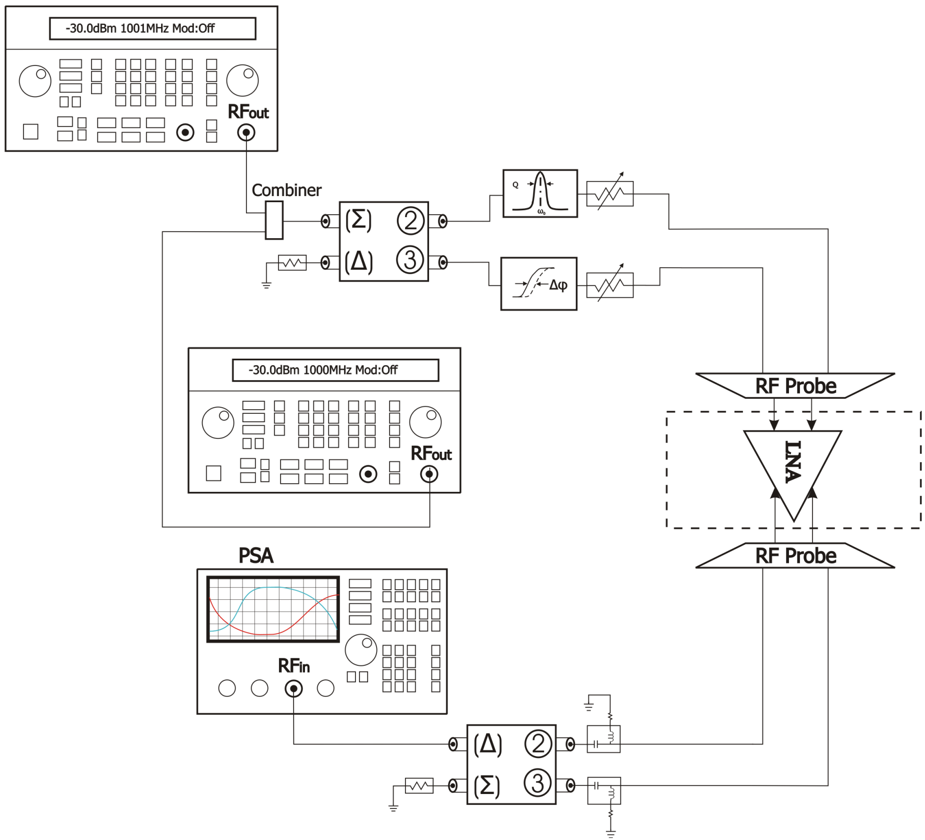

Figure 6.37: Setup for Full System Tests.

With optimal phase and amplitude offsets found from the system-IC tests, the system parameters that are independently varied include:

1. Interferer proximity to the signal of interest.
2. Accuracy of notch center frequency to that of interferer.
3. Amplitude of interferer and SOI.

The various instruments used in testing the phase-cancellation system performance are documented in Table 6.5.

Name	**Equipment Description**	**Purpose**
Summit 12000	Cascade Probe Station	On-wafer Probing
E4446A	PSA Spectrum Analyzer	Spectrum Measurement
E8257D	PSG Signal Generator	RF Signal Source
4010180	$1-18$GHz Hybrid	Differential, Common-Mode Stimuli
Atten. PCB	Variable Attenuator	Compensating Amplitude Mismatches
Combline PCB	Tunable Combline Filter	Interferer Tracking
Dielectric PCB	Dielectric Filter	Interferer Tracking
9428A	1-18 GHz Phase Shifter	Compensating Phase Mismatches
40A-GSG-125 -D-250	125um Pitch, Dual RF Probe	On-wafer Probing

Table 6.5: Equipment used for System Level Tests

6.4.2 SINR Improvement with Tunable Combline Filter

The system was tested $\approx$ 1.46GHz, which corresponds with the second mode of the tunable combline filter. In this case, the bandpass filter tracks the interfering tone, whose frequency is swept; the center frequency of the signal is kept constant. SINR improvement as a function of proximity and accuracy using the combline filter is shown in Fig. 6.38 and

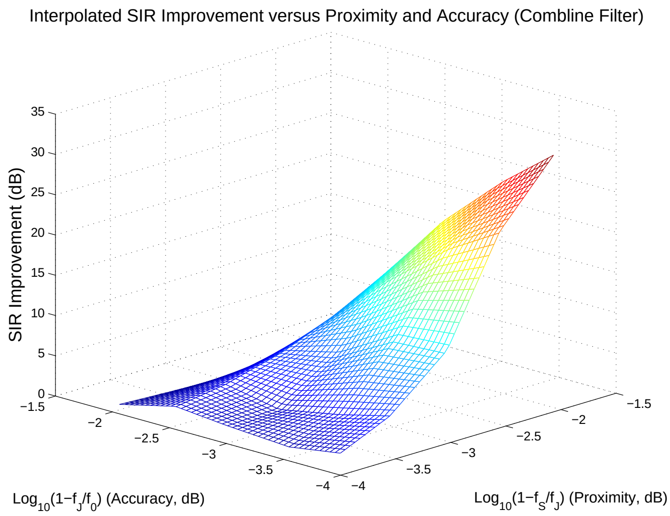

Figure 6.38: SINR Improvement vs. Proximity and Accuracy.

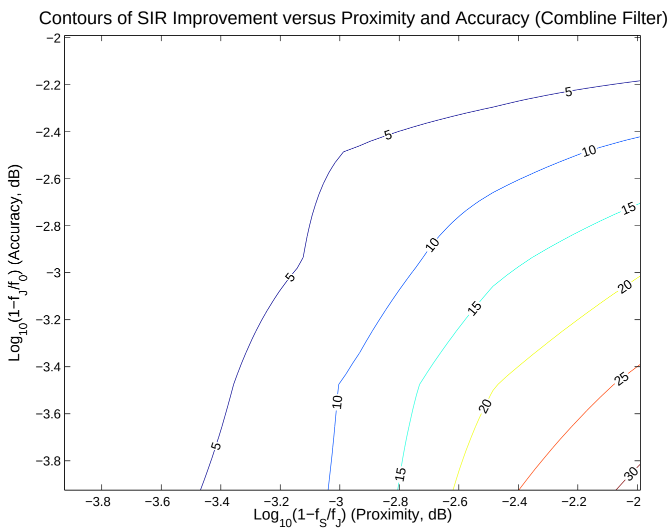

Figure 6.39: SINR Improvement Contours vs. Proximity and Accuracy.

contours of measured data are presented in Fig. 6.39. The system achieves $\approx$ 34dB of SINR improvement when the signal and interferer are significantly apart. While this is a lower value than expected, the filter's phase response has a significant effect. The system relies on having the interfering tones appear as common mode (same phase) to the amplifier inputs;

conversely, the signal tones should have sufficiently different phase (not common mode). Since the combline filter has multiple modes, the phase wraps around to 0 or $\pm 2n\pi$ for odd-modes; this is seen in the measured filter response. A second order bandpass filter has zero phase only at the center frequency. As the signal tones come closer to "common-mode" the system partially rejects the signal as well. From this aspect a multi-mode filter is not optimal.

6.4.3 SINR Improvement with Fixed Dielectric Filter

The system was tested $\approx$ 1.56GHz, which corresponds to the center frequency of the dielectric filter. Since the center frequency of the filter is not tunable, accuracy and proximity are varied by changing the signal frequency and that of the interferer, respectively. SINR improvement as a function of proximity and accuracy using the dielectric filter is shown in Fig. 6.40 and contours of measured data are presented in Fig. 6.41.

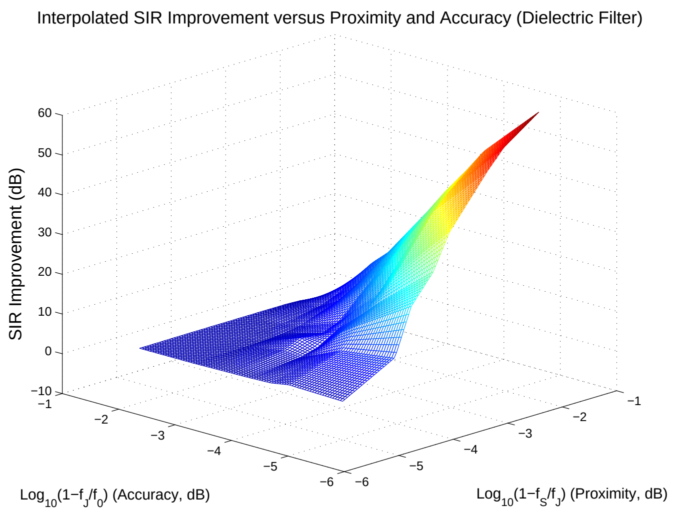

Figure 6.40: SINR Improvement vs. Proximity and Accuracy.

It is important to note that the dielectric filter has lower Q than the tunable combline, yet a "more monotonic" phase response, as previously explained. In this case the system achieves 58dB of SINR improvement, which is a remarkable advancement in interference rejection at RF or microwave frequencies.

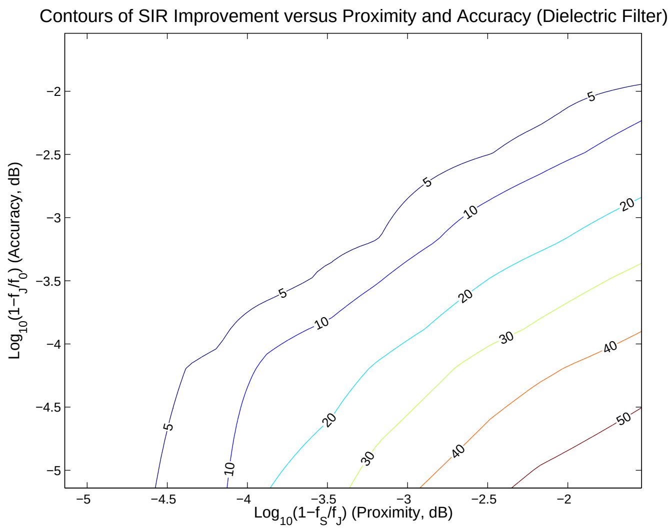

Figure 6.41: SINR Improvement Contours vs. Proximity and Accuracy.

The dynamic range of the system has been characterized by varying the power levels of the interferer and SOI while choosing fixed proximity and accuracy values; these values represent $\approx$ 50dB SINR improvement. These tests were carried out with the dielectric filter since it provides better rejection. Output SINR values as a function of interferer and SOI input power levels are shown in Fig. 6.42 with contour data presented in Fig. 6.43. The graph shows that the system achieves, on average, $45 - 50$dB of SINR improvement even at high jammer power levels. For example, at -10dBm jammer and -20dBm SOI power levels the SINR value is $\approx$ 40dB; this represents a 50dB SINR improvement ($\text{SINR}_{OUT} - \text{SINR}_{IN}$). Such improvement is maintained throughout the tested dynamic range. Large signal gain degrades only with regard to the SOI power level $\gtrapprox -20$dBm, as the gain of the differential LNA approaches its 1dB compression point. No sign of large signal degradation with regard to jammer power is visible throughout the tested rage.

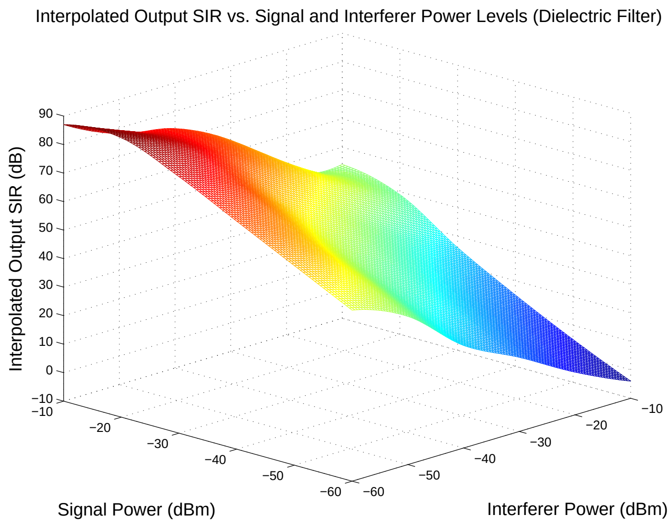

Figure 6.42: SINR Surface vs. Power Levels.

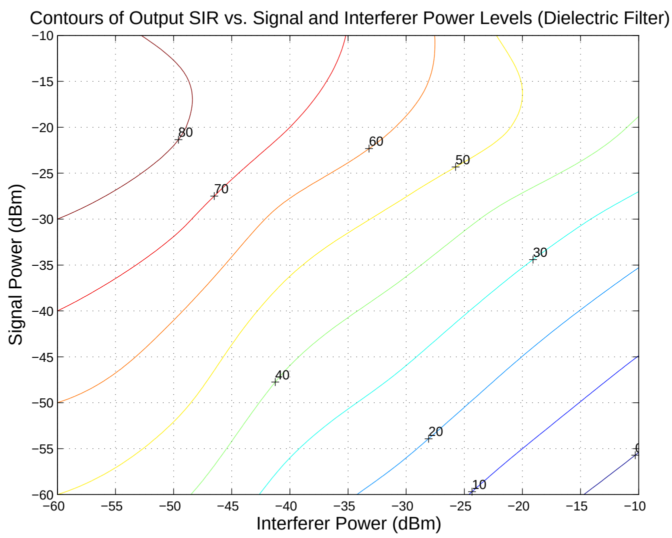

Figure 6.43: SINR Contours vs. Power Levels.

Chapter 7

Discussion and Conclusions

This project investigates the implementation of a phase cancellation technique to the design of a silicon germanium (SiGe) integrated circuit used in monitoring and attenuating interfering signals in RF communication systems in the 1-3GHz frequency range. As a precursor to this work, a literature review of interference scenarios and existing solutions underscores the importance of this study and provides background material for devising a fundamental solution to the interference induced problems, such as distortion or blocking. A MATLAB model of relevant interference scenarios has been constructed to study performance limitations of proposed solutions; implementation of the desired function include a second order notch filter and a phase cancellation technique; practical issues and desired goals render the phase cancellation technique more feasible and attractive at RF or microwave bands. The proposed system comprises of a bandpass filter that coarsely tracks the interfering signal, a delay network that fine tunes the phase so as to present common mode interfering tones to a differential amplifier with high CMRR. Candidate topologies for a differential LNA have been investigated in ADS with emphasis put on differential gain, input match, broadband operation, robustness to parasitics, low noise figure and nonlinearities; simulations aid in choosing a common base LNA with cross-coupling negative feedback to improve gain and noise figure. Layout of the amplifier has been completed using IBM's 8HP BiCMOS kit in Cadence design environment and an IC has been produced. On-wafer measurements have been conducted in order to:

1. Ensure functionality of the LNA and compare performance to ADS simulations
2. Study its IC system performance, mainly how CMRR is affected by mismatches
3. Evaluate its full-system functionality and the effectiveness of the proposed scheme

Measured data lines up well with predictions in terms of CMRR, gain, input and output return losses of the differential LNA. System-IC tests indicate the targeted 40dB CMRR has been met or surpassed throughout the test band. Choosing phase and amplitude "sweet spots" for maximizing CMRR faciliates in the full system tests. With relatively moderate filter quality factor ($Q_L \approx$25), whole system tests show 58dB SINR improvement, which provides a significant boost to a receiver's dynamic range and exceeds results from similar rejection methods published in the literature.

7.1 Future Recommendations

While overall the notch function is implemented surprisingly well, there are many improvements that can be suggested. First, rejection is greater with the fixed, commercial dielectric filter due to its monotonic phase response, yet, such filter can only work for a small range of frequencies. The tunable combline while able to track the jammer, did not perform as well with rejection of only about 34dB; this could be mainly attributed to its phase response wrapping around at several odd modes and partially cancelling the SOI. A bandpass filter with zero phase only at its center frequency is recommended. Since most applications would not have to cover such a wide frequency spectrum, it may be beneficial to target a narrower band. It is possible to investigate other tunable higher Q filters that can produce higher rejection. To improve loss, higher quality dielectric PCB material and lower loss varactors can be utilized. Improvements can also be made to the gain, noise figure and CMRR of the amplifier throughout the band. The gain rolls off at higher frequencies, most likely due to poorly modeled parasitics; a more appropriate modeling method would be to use a 3D planar simulator (like Momentum) to model the passive structures and combine them with the design kit active models. Improving gain would also improve noise figure and improving symmetry would increase CMRR. Integrating all the peripherals with the amplifier IC would also remove many interface, cabling issues but would certainly require more silicon area; additionally, since passives are lossier in silicon, the overall system noise figure would be degraded. Finally, while the tuning and tracking of interfering signals has been done manually, future work can focus on implementing such functionality with digital circuitry and software.

Appendix A

PCB Screenshots

A.1 Attenuator PCB

A screenshot of the attenuator PCB is shown in Fig. A.1.

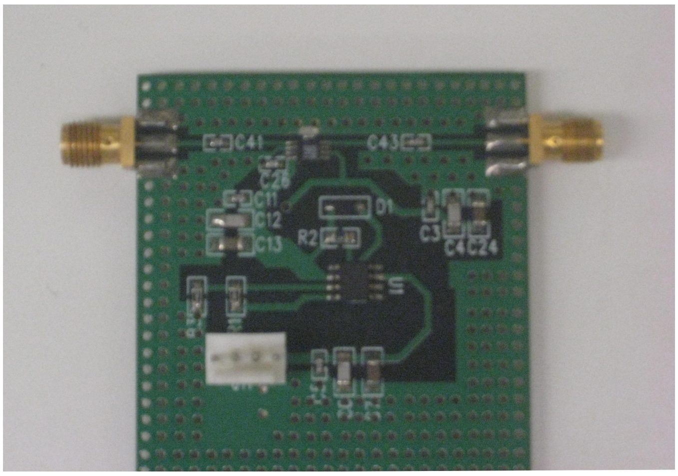

Figure A.1: PCB of Attenuator Module.

A.2 Dielectric Filter PCB

A screenshot of both dielectric filter PCBs is shown in Fig. A.2

A.3 Phase Shifter PCB

A screenshot of the phase shifter PCB is shown in Fig. A.3.

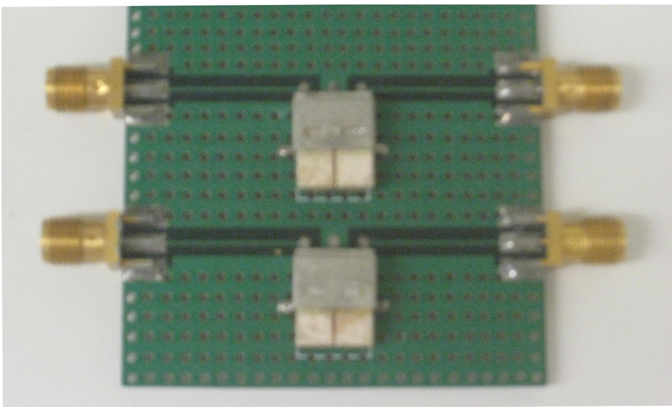

Figure A.2: PCB of both Dielectric Filters.

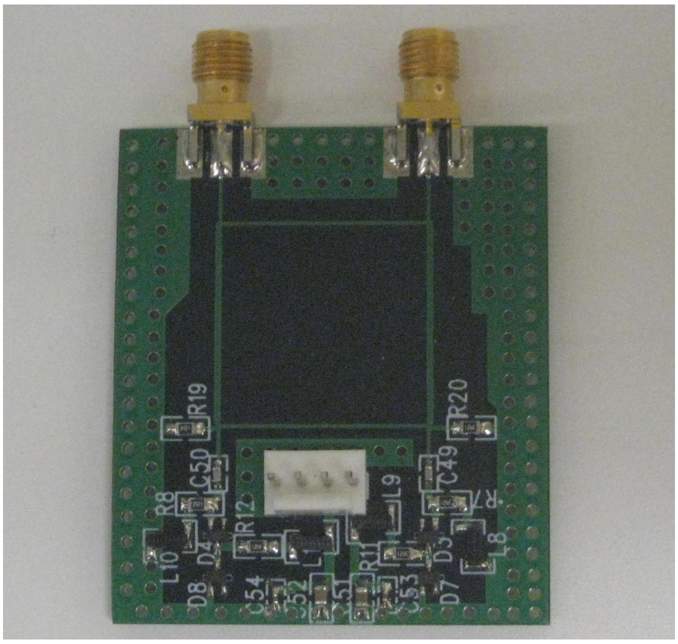

Figure A.3: PCB of Phase Shifter Module.

A.4 Combline Filters PCBs

Screenshots of the fixed frequency and tunable combline filters PCBs are shown in Fig. A.4 and A.5, respectively.

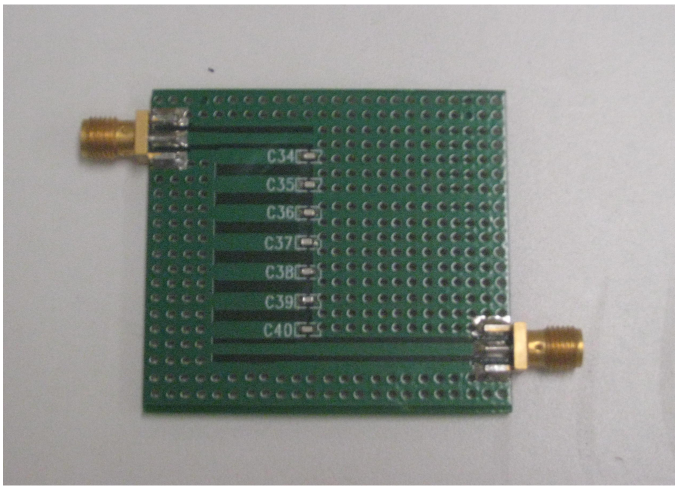

Figure A.4: PCB of Fixed Frequency Combline Filter.

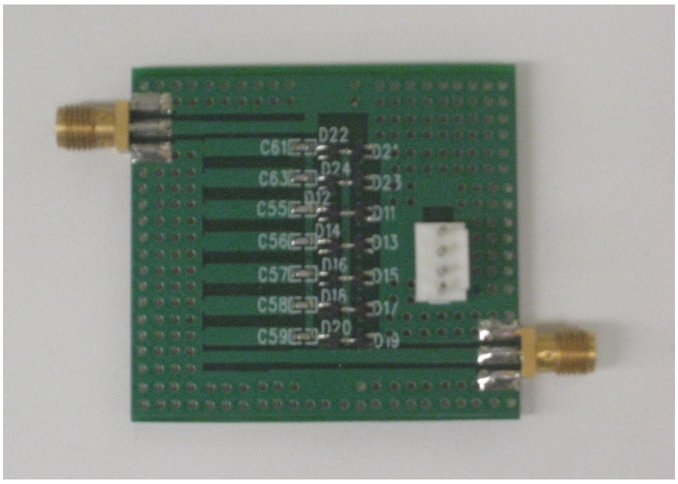

Figure A.5: PCB of Tunable Combline Filter.

Appendix B

Matlab Code for Second Order Notch Filter Simulations

B.1 Proximity and Accuracy for Q=50

```
% Transfer function filter study
% Studying SIR as a function of jammer proximity and accuracy

clc
clear all;
close all;
% grid
fs_grid = logspace(-6,-1,151);
f0_grid = logspace(-6,-1,151);
[x,y] = meshgrid(fs_grid,f0_grid);

% frequencies (w0=1e6 normalization)
f0 = 1e6;
w0 = 2*pi*f0;
w0_sq = w0^2;
wj = w0./(1-x);
ws = w0.*((1-x).*(1-y));

% Transfer function
Amin_dB = -60;
Amin = 10^(Amin_dB/20);
Q = 50;
rej_factor = ((Amin*w0)/Q);

a = [1 rej_factor w0_sq];    % rejection factor
b = [1 (w0/Q) w0_sq];    % 1/Q

% Transfer function
Hsig = freqs(a,b,ws);    % signal
Hjam = freqs(a,b,wj);    % jammer

% SNR improvement
V = [3 10 20 30 40 50];
```

```
SNR_improvement=abs(Hsig./Hjam).^2;

% Contour Plots
figure(1)
[C, h] = contour(log10(x),log10(y),10*log10(SNR_improvement),V);
clabel(C,h,V);
xlabel('Log(1-\omega_{J}/\omega_{0}) (accuracy)','FontSize',14);
ylabel('Log(1-\omega_{S}/\omega_{J}) (proximity)','FontSize',14);
set(gca,'XTick',-5:1:-1);
set(gca,'YTick',-5:1:-1);
set(gca,'XTickLabel',{'-5','-4','-3','-2','-1'},'FontSize',13);
set(gca,'YTickLabel',{'-5','-4','-3','-2','-1'},'FontSize',13);
set(gca,'XGrid','on');
set(gca,'YGrid','on');
title('Contours of SIR Improvement (dB) vs. Proximity and Accuracy (Q=50)');
print -depsc2 SIR_improvement_contour_Q50.eps

% 3D Plots
figure (2)
g = surf(log10(x),log10(y),10*log10(SNR_improvement));
view([-38,26]);

set(gca,'XGrid','on');
set(gca,'YGrid','on');
set(gca,'ZGrid','on');
xlabel('Log(1-\omega_{J}/\omega_{0}) (accuracy)','FontSize',14);
ylabel('Log(1-\omega_{S}/\omega_{J}) (proximity)','FontSize',14);
zlabel('SIR Improvement (dB)','FontSize',14);
title('SIR Improvement vs. Proximity and Accuracy (Q=50)','FontSize',14);
print -depsc2 SIR_improvement_Q50.eps
```

B.2 Fixed SINR Improvement for Q=10,30,50,100

```
% Transfer function filter study
% Studying SIR as a function of accuracy and jammer proximity for Q's considered

clc
clear all;
close all;
% grid
fs_grid = logspace(-6,-1,151);
f0_grid = logspace(-6,-1,151);
[x,y] = meshgrid(fs_grid,f0_grid);

% frequencies (w0=1e6 normalization)
f0 = 1e6;
w0 = 2*pi*f0;
w0_sq = w0^2;
wj = w0./(1-x);
ws = w0.*((1-y).*(1-x));

% Transfer function
Amin_dB = -60;
Amin = 10^(Amin_dB/20);
```

```
Q = 10;
rej_factor = ((Amin*w0)/Q);

a = [1 rej_factor w0_sq];     % rejection factor
b = [1 (w0/Q) w0_sq];     % 1/Q

% Transfer function
Hsig = freqs(a,b,ws);     % signal
Hjam = freqs(a,b,wj);     % jammer
SNR_improvement_q10=abs(Hsig./Hjam).^2;

% Repeat for Q =30
Q = 30;
rej_factor = ((Amin*w0)/Q);

a = [1 rej_factor w0_sq];     % rejection factor
b = [1 (w0/Q) w0_sq];     % 1/Q

% Transfer function
Hsig = freqs(a,b,ws);     % signal
Hjam = freqs(a,b,wj);     % jammer
SNR_improvement_q30=abs(Hsig./Hjam).^2;

% Repeat for Q =50
Q = 50;
rej_factor = ((Amin*w0)/Q);

a = [1 rej_factor w0_sq];     % rejection factor
b = [1 (w0/Q) w0_sq];     % 1/Q

% Transfer function
Hsig = freqs(a,b,ws);     % signal
Hjam = freqs(a,b,wj);     % jammer
SNR_improvement_q50=abs(Hsig./Hjam).^2;

% Repeat for Q =100
Q = 100;
rej_factor = ((Amin*w0)/Q);

a = [1 rej_factor w0_sq];     % rejection factor
b = [1 (w0/Q) w0_sq];     % 1/Q

% Transfer function
Hsig = freqs(a,b,ws);     % signal
Hjam = freqs(a,b,wj);     % jammer
SNR_improvement_q100=abs(Hsig./Hjam).^2;

% Plot SIR improvement
V = [-100 40];
figure(1)
[C, h] = contour(log10(x),log10(y),10*log10(SNR_improvement_q10),V,'g-');
hold on
contour(log10(x),log10(y),10*log10(SNR_improvement_q30),V,'k-');
hold off
hold on
```

```
contour(log10(x),log10(y),10*log10(SNR_improvement_q50),V,'r-');
hold off
hold on
contour(log10(x),log10(y),10*log10(SNR_improvement_q100),V,'b-');
hold off

%clabel(C,h,V);
set(gca,'XGrid','on');
set(gca,'YGrid','on');
xlabel('Log(1-\omega_{J}/\omega_{0}) (accuracy)','FontSize',14);
ylabel('Log(1-\omega_{S}/\omega_{J}) (proximity)','FontSize',14);
text('String','Q=100 \rightarrow',...
    'Position',[-5.09 -1.746 17.32],...
    'FontSize',16);
text('String','\leftarrow Q=10',...
    'Position',[-3.697 -1.646 17.32],...
    'FontSize',16);
set(gca,'XTick',-5:1:-1);
set(gca,'YTick',-5:1:-1);
set(gca,'XTickLabel',{'-5','-4','-3','-2','-1'},'FontSize',13);
set(gca,'YTickLabel',{'-5','-4','-3','-2','-1'},'FontSize',13);
legend('Q=10','Q=30','Q=50','Q=100',4);
title('40dB SIR Improvement vs. Proximity and Accuracy (Q=10,30,50,100)');
print -depsc2 SIR_improvement_40dB_Qsweep.eps
```

B.3 Dynamic Range Investigation

```
% Dynamic Range filter study
% Studying SINR as a function of NF, Noise and Interferer Power

clc
clear all
close all

% Frequencies (w0=1e6 normalization), accuracy 10^-4
% and proximity 10^-1
pts = 151;
f0 = 1e6;
w0 = 2*pi*f0;
w0_sq = w0^2;
wj = w0*(1-10^(-5));
ws = wj*(1-10^(-1));

% Transfer function
Amin_dB = -60;
Amin = 10^(Amin_dB/20);
Q = 50;
rej_factor = ((Amin*w0)/Q);

% Pick points for the frequencies wj and ws and find transfer functions
Hsig = (-ws.^2 + i.*ws.*rej_factor + w0_sq)./(-ws.^2 + i.*ws.*(w0./Q) + w0_sq);
Hjam = (-wj.^2 + i.*wj.*rej_factor + w0_sq)./(-wj.^2 + i.*wj.*(w0./Q) + w0_sq);

% Power of interferer, noise and noise factor
```

```
Pj_ni_grid = logspace(-1,9,pts);
[Pj_ni,ni_Pj] = meshgrid(Pj_ni_grid);
nf_grid = logspace(-2,0.303,pts);
[nf, nf2] = meshgrid(nf_grid);
nf_db = 10.*nf;
power_tf = ((abs(Hjam)./abs(Hsig)).^2);
SINR_improvement=10.*log10((1+(Pj_ni))./(power_tf.*(Pj_ni)+ 10.^(nf2)));

% Plot SNR improvement contours
V = [0 10 20 30 40 50 60];
figure(1)
[C, h] = contour(10.*log10(1./Pj_ni),10*nf2,SINR_improvement,V);
clabel(C,h,V);
set(gca,'XGrid','on');
set(gca,'YGrid','on');
xlabel('10Log_{10}(Input Noise Power/P_{J}) (dB)','FontSize',14);
ylabel('Noise Figure (dB)','FontSize',14);
title('SINR Improvement (dB) vs. Interferer, Input Noise and NF (Q=50)');
print -depsc2 SINR_improvement_contour_q50.eps

% Plot 3D
figure (2)
g = mesh(10.*log10(1./Pj_ni),10*nf2,SINR_improvement);
view([45,30]);
set(gca,'XGrid','on');
set(gca,'YGrid','on');
set(gca,'ZGrid','on');
xlabel('10Log_{10}(Input Noise Power/P_{J}) (dB)','FontSize',14);
ylabel('Noise Figure (dB)','FontSize',14);
zlabel('SINR Improvement (dB)','FontSize',14);
title('SINR Improvement (dB) vs. Interferer, Input Noise and NF (Q=50)');
print -depsc2 SINR_improvement_q50.eps
```

Appendix C

Matlab Code for Phase Cancellation System Simulations

C.1 Proximity and Accuracy for Q=50

```
% Studying SIR as a function of proximity and bandpass accuracy
% Signal and Interferer are on opposite sides of passband

clc
clear all
close all
pts =151;
min_atten = 0.3;
diff_gain_dB = 25;
diff_gain = 10^(diff_gain_dB/20);
comm_gain_dB = -38;
comm_gain = 10^(comm_gain_dB/20);
dif2comm_gain_dB = -38;
diff2comm_gain = 10^(comm_gain_dB/20);

% grid
fx_grid = logspace(-5,-1,pts);
fy_grid = logspace(-5,-1,pts);
[x,y] = meshgrid(fx_grid,fy_grid);

% Signal and interferer frequencies (w0=1e6 normalization)
fbp = 1e9;
wbp = 2*pi*fbp;
wbp_sq = wbp^2;
wj = wbp.*(1-x);
ws = wj./(1-y);
phi_slope = (pi/3)/1e9;

% Second order Bandpass Q=50
Q = 50;
a = [0 -(wbp/Q) 0];       % numerator
b = [1 (wbp/Q) wbp_sq];   % denominator
```

```
% Transfer function values at ws and wj
divider = 1/sqrt(2);
Hs_up = freqs(a,b,ws);     % signal
Hj_up = freqs(a,b,wj);     % interferer
Hs_up = divider.*Hs_up;     % signal
Hj_up = divider.*Hj_up;     % interferer

phi = angle(Hj_up);
alpha = abs(Hj_up);
Hs_down = alpha.*exp(i.*(phi+(abs(ws-wj)).*phi_slope));
Hj_down = alpha.*exp(i.*phi);
Hsig = diff_gain.*(Hs_up - Hs_down) +
(1/2)*comm_gain.*(Hs_up+Hs_down)+diff2comm_gain.*(Hs_up - Hs_down);
Hjam = diff_gain.*(Hj_up - Hj_down) +
(1/2)*comm_gain.*(Hj_up+Hj_down)+diff2comm_gain.*(Hj_up - Hj_down);

SIR_improvement=(abs(Hsig./Hjam)).^2;

% SNR improvement
V = [-10 0 3 10 20 30 40 50 60];
figure(1)
[C, h] = contour(log10(x),log10(y),10.*log10(SIR_improvement),V);
clabel(C,h,V);
set(gca,'XGrid','on');
set(gca,'YGrid','on');
xlabel('Log_{10}(\omega_{J}/\omega_{BP})','FontSize',14);
ylabel('Log_{10}(\omega_{J}/\omega_{S})','FontSize',14);
title('Contours of SIR Improvement (dB) vs. Proximity and Accuracy (Q=50)');
print -depsc2 SIR_contours_otherSide_q50.eps

figure (2)
g = surf(log10(x),log10(y),10.*log10(SIR_improvement));
view([-40,30]);
set(gca,'XGrid','on');
set(gca,'YGrid','on');
set(gca,'ZGrid','on');
xlabel('Log_{10}(1-\omega_{J}/\omega_{BP})','FontSize',14);
ylabel('Log_{10}(1-\omega_{J}/\omega_{S})','FontSize',14);
zlabel('SIR Improvement (dB)','FontSize',14);
title('SIR Improvement (dB) vs. Proximity and Accuracy (Q=50)');
print -depsc2 SIR_otherSide_q50.eps
```

C.2 Fixed SINR Improvement for Q=10,30,50,100

```
% Altin Pelteku
% Transfer function of complete system
% SOI and nearby interferer
% Studying SIR for all Qs

clc
clear all
close all
pts =151;
min_atten = 0.3;
```

```
diff_gain_dB = 25;
diff_gain = 10^(diff_gain_dB/20);
comm_gain_dB = -38;
comm_gain = 10^(comm_gain_dB/20);
dif2comm_gain_dB = -38;
diff2comm_gain = 10^(comm_gain_dB/20);

% grid
fx_grid = logspace(-5,-0.01,pts);
fy_grid = logspace(-5,-0.01,pts);
[x,y] = meshgrid(fx_grid,fy_grid);

% Signal and interferer frequencies (w0=1e6 normalization)
fbp = 1e9;
wbp = 2*pi*fbp;
wbp_sq = wbp^2;
wj = wbp.*(1-x);
ws = wj.*(1-y);
phi_slope = (pi/3)/1e9;

% Second order Bandpass Q=10
Q = 10;
a = [0 -(wbp/Q) 0];       % numerator
b = [1 (wbp/Q) wbp_sq];   % denominator

% Transfer function values at ws and wj
divider = 1/sqrt(2);
Hs_up = freqs(a,b,ws);     % signal
Hj_up = freqs(a,b,wj);     % interferer
Hs_up = divider.*Hs_up;     % signal
Hj_up = divider.*Hj_up;     % interferer

phi = angle(Hj_up);
alpha = abs(Hj_up);
Hs_down = alpha.*exp(i.*(phi-(abs(wj-ws)).*phi_slope));
Hj_down = alpha.*exp(i.*phi);
Hsig = diff_gain.*abs(Hs_up - Hs_down) +
(1/2)*comm_gain.*abs(Hs_up+Hs_down)+diff2comm_gain.*abs(Hs_up - Hs_down);
Hjam = diff_gain.*abs(Hj_up - Hj_down) +
(1/2)*comm_gain.*abs(Hj_up+Hj_down)+diff2comm_gain.*abs(Hj_up - Hj_down);

SIR_improvement_q10=(abs(Hsig./Hjam)).^2;

% Second order Bandpass Q=30
Q = 30;
a = [0 -(wbp/Q) 0];       % numerator
b = [1 (wbp/Q) wbp_sq];   % denominator

% Transfer function values at ws and wj
divider = 1/sqrt(2);
Hs_up = freqs(a,b,ws);     % signal
Hj_up = freqs(a,b,wj);     % interferer
Hs_up = divider.*Hs_up;     % signal
Hj_up = divider.*Hj_up;     % interferer
```

```
phi = angle(Hj_up);
alpha = abs(Hj_up);
Hs_down = alpha.*exp(i.*(phi-(abs(wj-ws)).*phi_slope));
Hj_down = alpha.*exp(i.*phi);
Hsig = diff_gain.*abs(Hs_up - Hs_down) +
(1/2)*comm_gain.*abs(Hs_up+Hs_down)+diff2comm_gain.*abs(Hs_up - Hs_down);
Hjam = diff_gain.*abs(Hj_up - Hj_down) +
(1/2)*comm_gain.*abs(Hj_up+Hj_down)+diff2comm_gain.*abs(Hj_up - Hj_down);

SIR_improvement_q30=(abs(Hsig./Hjam)).^2;

% Second order Bandpass Q=50
Q = 50;
a = [0 -(wbp/Q) 0];       % numerator
b = [1 (wbp/Q) wbp_sq];   % denominator

% Transfer function values at ws and wj up and down branches
divider = 1/sqrt(2);
Hs_up = freqs(a,b,ws);     % signal
Hj_up = freqs(a,b,wj);     % interferer
Hs_up = divider.*Hs_up;     % signal
Hj_up = divider.*Hj_up;     % interferer

phi = angle(Hj_up);
alpha = abs(Hj_up);
Hs_down = alpha.*exp(i.*(phi-(abs(wj-ws)).*phi_slope));
Hj_down = alpha.*exp(i.*phi);
Hsig = diff_gain.*abs(Hs_up - Hs_down) +
(1/2)*comm_gain.*abs(Hs_up+Hs_down)+diff2comm_gain.*abs(Hs_up - Hs_down);
Hjam = diff_gain.*abs(Hj_up - Hj_down) +
(1/2)*comm_gain.*abs(Hj_up+Hj_down)+diff2comm_gain.*abs(Hj_up - Hj_down);

SIR_improvement_q50=(abs(Hsig./Hjam)).^2;

% Second order Bandpass Q=100
Q = 100;
a = [0 -(wbp/Q) 0];       % numerator
b = [1 (wbp/Q) wbp_sq];   % denominator

% Transfer function values at ws and wj
divider = 1/sqrt(2);
Hs_up = freqs(a,b,ws);     % signal
Hj_up = freqs(a,b,wj);     % interferer
Hs_up = divider.*Hs_up;     % signal
Hj_up = divider.*Hj_up;     % interferer

phi = angle(Hj_up);
alpha = abs(Hj_up);
Hs_down = alpha.*exp(i.*(phi-(abs(wj-ws)).*phi_slope));
Hj_down = alpha.*exp(i.*phi);
Hsig = diff_gain.*abs(Hs_up - Hs_down) +
(1/2)*comm_gain.*abs(Hs_up+Hs_down)+diff2comm_gain.*abs(Hs_up - Hs_down);
Hjam = diff_gain.*abs(Hj_up - Hj_down) +
(1/2)*comm_gain.*abs(Hj_up+Hj_down)+diff2comm_gain.*abs(Hj_up - Hj_down);
```

```
SIR_improvement_q100=(abs(Hsig./Hjam)).^2;

% Plot 40 dB SIR improvement contours
V = [0 40];
figure(1)
[C, h] = contour(log10(x),log10(y),10.*log10(SIR_improvement_q10),V,'g-');
clabel(C,h,V);
hold on
[C, h] = contour(log10(x),log10(y),10.*log10(SIR_improvement_q30),V,'k-');
clabel(C,h,V);
hold off
hold on
[C, h] = contour(log10(x),log10(y),10.*log10(SIR_improvement_q50),V,'r-');
clabel(C,h,V);
hold off
hold on
[C, h] = contour(log10(x),log10(y),10.*log10(SIR_improvement_q100),V,'b-');
clabel(C,h,V);
hold off
set(gca,'XGrid','on');
set(gca,'YGrid','on');
xlabel('Log_{10}(1-\omega_{J}/\omega_{BP})','FontSize',14);
ylabel('Log_{10}(1-\omega_{S}/\omega_{J})','FontSize',14);
legend('Q=10','Q=30','Q=50','Q=100',2);
title('40dB SIR Improvement Contours vs. Proximity and Accuracy','FontSize',14);
print -depsc2 SIR_improvement_contours_40dB.eps
```

C.3 SIR Improvement as a function of Mismatches

```
% SIR Improvement as a function of amplitude and phase mismatches

clc
clear all
close all
pts =151;
min_atten = 0.3;
diff_gain_dB = 25;
diff_gain = 10^(diff_gain_dB/20);
comm_gain_dB = -38;
comm_gain = 10^(comm_gain_dB/20);
dif2comm_gain_dB = -38;
diff2comm_gain = 10^(comm_gain_dB/20);

% Mismatch grid
da_grid = linspace(1/1.26,1.26,pts);
dphi_grid = linspace(-pi/8,pi/8,pts);
[da,dphi] = meshgrid(da_grid,dphi_grid,pts);

% Signal and interferer frequencies (w0=1e6 normalization)
fbp = 1e9;
wbp = 2*pi*fbp;
wbp_sq = wbp^2;
wj = wbp.*(1-10^(-10));
ws = wj.*(1-10^(-2));
```

```
phi_slope = (pi/3)/1e9;

% Second order Bandpass Q=30
Q = 30;
divider = 1/sqrt(2);
Hs_up = (-i.*ws.*(wbp./Q))./(-ws.^2 + i.*ws.*(wbp./Q) + wbp_sq);    % signal
Hj_up = (-i.*wj.*(wbp./Q))./(-wj.^2 + i.*wj.*(wbp./Q) + wbp_sq);    % interferer
Hs_up = divider.*Hs_up;    % signal
Hj_up = divider.*Hj_up;    % interferer

phi = angle(Hj_up)+dphi;
alpha = abs(Hj_up).*da;
Hs_down = alpha.*exp(i.*(phi-(abs(wj-ws)).*phi_slope));
Hj_down = (alpha).*exp(i.*(phi));
Hsig = diff_gain.*abs(Hs_up - Hs_down) +
(1/2)*comm_gain.*abs(Hs_up+Hs_down)+diff2comm_gain.*abs(Hs_up - Hs_down);
Hjam = diff_gain.*abs(Hj_up - Hj_down) +
(1/2)*comm_gain.*abs(Hj_up+Hj_down)+diff2comm_gain.*abs(Hj_up - Hj_down);
SIR_improvement_q30=(abs(Hsig./Hjam)).^2;

% Plot SIR improvement contours and 3D
V = [3 10 15 20 30 40];
figure(1)
[C, h] = contour(20.*log10(da),dphi,10.*log10(SIR_improvement_q30),V);
clabel(C,h,V);
set(gca,'XGrid','on');
set(gca,'YGrid','on');
xlabel('Amplitude Mismatch \pm\Delta\alpha (dB)','FontSize',14);
ylabel('Phase Mismatch \Delta\phi (rad)','FontSize',14);
title('SIR Improvement Contours vs. Phase and Amplitude Mismatch (Q=30)');
print -depsc2 SIR_improvement_contours_Q30.eps

figure (2)
g = surf(20.*log10(da),dphi,10.*log10(SIR_improvement_q30));
view([-40,20]);
set(gca,'XGrid','on');
set(gca,'YGrid','on');
set(gca,'ZGrid','on');
xlabel('Amplitude Mismatch \pm\Delta\alpha (dB)','FontSize',14);
ylabel('Phase Mismatch \Delta\phi (rad)','FontSize',14);
zlabel('SIR Improvement (dB)','FontSize',14);
title('SIR Improvement vs. Phase and Amplitude Mismatch (Q=30)');
print -depsc2 SIR_improvement_q30.eps
```

Appendix D

Matlab Code for Combline Filter

D.1 Combline Design

```
% Altin Pelteku
% Equations for Combline Filter design

% define constants and variables
eps0 = 8.8541878176e-12;
Z0 = 50;
f0 = 1.8e9;
omega0 = 2*pi*f0;
c = 3e8;
epsr = 4.4;
epseff = 3.22948;
YA = 1/Z0;

% Choose filter sections
n = 7;
g0 = 1;
g8 = 1;
g = [1.7372 1.2583 2.6381 1.3444 2.6381 1.2583 1.7372];
w = 0.01;
omega1_pr=1;

% Resonator lengths and angle at center frequency
lambda0 = c/f0/sqrt(epseff);
length = lambda0/8;
theta0 = 2*pi*length/lambda0;

% Define port impedances
for i = 1:n
    Zk(i)=50;
    Yk(i)=1/Zk(i);
end

% Terminating capacitances
for i = 1:n
    Clump(i)=Yk(i)*cot(theta0)/(omega0);
end
```

```
% Find inverter elements
for i = 1:n
    Bk(i) = (1/2)*Yk(i)*(cot(theta0)+theta0*(csc(theta0))^2);
end

for i = 1:n-1
    Jkk(i) = w*sqrt(Bk(i)*Bk(i+1)/(g(i)*g(i+1)));
end

% Compute mutual admittances
% Here Ymn is the same as GTn from Matthaei

Y11 = Yk(1) - Jkk(1)*tan(theta0);
Y77 = Yk(n) - Jkk(n-1)*tan(theta0);

Y01 = w*Bk(1)/(g0*g(1));
Y78 = w*Bk(n)/(g(n)*g8);

for i = 1:n-1
    Ykk(i) = Jkk(i)*tan(theta0);
end

% Compute self-capacitances
C0_e = 376.7*YA*(1-sqrt(Y01/YA))/sqrt(epseff);
Ck_e(1) = 376.7*YA*((Yk(1)/YA)-1+(Y01/YA)-
      (Jkk(1)/YA)*tan(theta0))/sqrt(epseff) + C0_e;
for i = 2:n-1
    Ck_e(i) = 376.7*YA*((Yk(i)/YA)-(Jkk(i-1)/YA)*tan(theta0)-
          (Jkk(i)/YA)*tan(theta0))/sqrt(epseff);
end

Ck_e(8) = 376.7*YA*(1-sqrt(Y78/YA))/sqrt(epseff);
Ck_e(7) = 376.7*YA*((Yk(7)/YA)-1+(Y78/YA)-
      (Jkk(n-1)/YA)*tan(theta0))/sqrt(epseff) + Ck_e(8);

% Compute mutual capacitances

C01_e = 376.7*YA/sqrt(epseff)-C0_e;

for i = 1:n-1
    Ckk_e(i) = 376.7*YA*(Jkk(i)*tan(theta0)/YA)/sqrt(epseff);
end

Ckk_e(7) = 376.7*YA/sqrt(epseff)-Ck_e(8);
```

D.2 Physical Parameters for PCB Implementation

```
% Altin Pelteku
% Dimensions for Combline Filter design
% Using 4pcb.com fab

% define ustrip parameters in mils
t = 1.4;
```

```
b = 47.7;
w = 60;

t_b = t/b

% Extract s/b parameters from graphs
length_mils = length*100000/2.54
s = [0.59*b 1.33*b 1.38*b 1.384*b 1.384*b 1.38*b 1.33*b 0.59*b]
s_b = s./b

% Extract cfe and cf capacitances

cfe = (1/100)*[0.5 0.62 0.64 0.641 0.641 0.64 0.62 0.5];
cf = 0.65;

% Find parallel plate capacitances and linewidths
cp0_e = (C0_e-2*cf-2.*cfe(1))./2
w0 = cp0_e*b
cp_e(8) = (Ck_e(8)-2*cf-2.*cfe(8))./2;
w(8) = cp_e(8)*b;

for i = 1:n
    cp_e(i) = (Ck_e(i)-2*cfe(i)-2*cfe(i+1))./2;
    w(i) = cp_e(i)*b;
end

cp_e
w
```

Bibliography

[1] R. G. Meyer and A. K. Wong, "Blocking and desensitization in RF amplifiers," *IEEE Journal of Solid-State Circuits*, vol. 30, no. 8, pp. 944-946, Aug. 1995.

[2] A. A. Abidi, "Direct-conversion radio transceivers for digital communications," *IEEE Journal of Solid-State Circuits*, vol. 30, no. 12, pp. 1399-1410, Dec. 1995.

[3] B. Razavi, "Design considerations for direct-conversion receivers," *IEEE Transactions on Circuits and SystemsII: Analog and Digital Signal Processing*, vol. 44, no. 6, pp. 428-435, June 1997.

[4] 3GPP, "Radio frequency system scenarios," 3GPP, Technical Report 25.942, ver. 8.0.0, Dec. 2008.

[5] P. Leaves et al., "Dynamic spectrum allocation in composite reconfigurable wireless networks," *IEEE Communications Magazine*, vol. 42, no. 5, pp. 72-81, May 2004.

[6] J. D. Laster and J. H. Reed, "Interference rejection in digital wireless communications," *IEEE Signal Processing Magazine*, vol. 14, no. 3, pp. 37-62, May 1997.

[7] A. Şafak, "Optimal channel reuse in cellular radio systems with multiple correlated log-normal interferers," *IEEE Transactions on Vehicular Technology*, vol. 43, no. 2, pp. 304-312, May 1994.

[8] A. Durantini, F. Mazzenga and G. Santella, "A semi-analytic approach for CDMA systems performance evaluation with adjacent channel interference," in *59th IEEE Vehicular Technology Conference*, vol. 3, Milan, Italy, May 2004, pp. 1466-1470.

[9] S. A. Musa and W. Wasylkiwskyj, "Co-Channel interference of spread spectrum systems in a multiple user environment," *IEEE Transactions on Communications*, vol. COM-26, no. 10, pp. 1405-1413, Oct. 1978.

[10] S. K. Park, D. H. Kim, S. H. Cho and K. R. Cho, "Downlink blocking probability in the handover region for uncoordinated WCDMA and cdma2000 systems," in *10th International Conference on Telecommunications*, vol. 2, Papeete, French Polynesia, Feb.-March 2003, pp. 1161-1166.

[11] M. Suryanegara, E. R. Hutabarat and D. Gunawan, "The interference on WCDMA system in 3G coexistence network," in *17th IEEE International Symposium on Personal, Indoor and Mobile Radio Communications*, Helsinki, Finland, Sept. 2006, pp. 1-5.

[12] C. Hamacher, "Spectral coexistence of DVB-T and UMTS in a hybrid radio system," in *IST Mobile Communications Summit*, Barcelona, Spain, Sept. 2001, pp. 203-208.

[13] K. Heiska, H. Posti, P. Muszynski, T. Rautiainen and J. Numminen, "WCDMA downlink coverage reduction due to adjacent channel interference," *Wireless Personal Communications*, vol. 23, no. 2, pp. 217-242, Nov. 2002.

[14] V. Aparin and L. E. Larson, "Analysis and reduction of cross-modulation distortion in CDMA receivers," *IEEE Transactions on Microwave Theory and Techniques*, vol. 51, no. 5, pp. 1591-1602, May 2003.

[15] C. R. Chang, S. Cassidy, J. Panicker, J.-Z. Wan, M. Yee and S. Tran, "Experimental investigations of PCS interference between CDMA and GSM," in *49th IEEE Vehicular Technology Conference*, Houston, TX, vol. 1, Jul. 1999, pp. 772-776.

[16] S.-J. Park, H.-B. Ha, J.-T. Chung, Y.-S. Shun and D.-Y. Lee, "Frequency coordination between adjacent carriers of two CDMA operators," in *46th IEEE Vehicular Technology Conference*, Atlanta, GA, vol. 3, Apr.-May 1996, pp. 1458-1461.

[17] W. Chang-guo and Z. Hong-bo, "Evaluation of co-site interference between PCS1900 and UMTS in a typical outdoor environment," in *2005 Asia-Pacific Microwave Conference Proceedings*, Suzhou, China, vol. 2, Dec. 2005, pp. 1-8.

[18] K. Hamied, and G. Labedz, "AMPS cell transmitter interference to CDMA mobile receiver," in *46th IEEE Vehicular Technology Conference*, Atlanta, GA, vol. 3, Apr.-May 1996, pp. 1467-1471.

[19] I. Timang and H. Y. Kanalebe, "Interference impact of WCDMA mobile station on IS-95 Mobile Station performance," in *5th IFIP International Conference on Wireless and Optical Communications Networks*, Surabaya, Indonesia, May 2008, pp. 1-4.

[20] V. Vanghi, M. Saglam and J. Jindi, "Frequency coordination between UMTS and GSM systems at 900 MHz," in *18th IEEE International Symposium on Personal, Indoor and Mobile Radio Communications*, Athens, Greece, Sept. 2007, pp. 1-5.

[21] C.-M. Su and L. B. Milstein, "Analysis of a coherent frequency-hopped spread-spectrum receiver in the presence of jamming," *IEEE Transactions on Communications*, vol. 38, no. 5, pp. 715-726, May 1990.

[22] R. L. Pickholtz, D. L. Schilling and L. B. Milstein, "Theory of spread-spectrum communications–a tutorial." *IEEE Transactions on Communications*, vol. COM-30, no. 5, pp. 855-884, May 1982.

[23] F. M. Hsu and A. A. Giordano, "Digital whitening techniques for improving spread spectrum communications performance in the presence of narrowband jamming and interference," *IEEE Transactions on Communications*, vol. COM-26, no. 2, pp. 209-216, Feb. 1978.

[24] J. W. Ketchum and J. G. Proakis, "Adaptive algorithms for estimating and suppressing narrow-band interference in PN spread-spectrum systems," *IEEE Transactions on Communications*, vol. COM-30, no. 5, pp. 913-924, May 1982.

[25] R. A. Iltis and L. B. Milstein, "Performance analysis of narrow-band interference rejection techniques in DS spread-spectrum systems," *IEEE Transactions on Communications*, vol. COM-32, no. 11, pp. 1169-1177, Nov. 1984.

[26] E. Masry and L. B. Milstein, "Performance of DS spread-spectrum receiver employing

interference-suppression filters under a worst-case jamming condition," *IEEE Transactions on Communications*, vol. COM-34, no. 1, pp. 13-21, Jan. 1986.

[27] L. B. Milstein, "Interference rejection techniques in spread spectrum communications," *IEEE Proceedings*, vol. 76, no. 6, pp. 657-671, June 1988.

[28] L. A. Rusch and H. V. Poor, "Narrowband interference suppression in CDMA spread spectrum communications," *IEEE Transactions on Communications*, vol. 42, no. 234, part 3, pp. 1969-1979, Apr. 1994.

[29] R. Vijayan and H. V. Poor, "Nonlinear techniques for interference suppression in spread-spectrum systems," *IEEE Transactions on Communications*, vol. 38, no. 7, pp. 1060-1065, July 1990.

[30] W. Zhu et al., "MIMO systems for military communications," in *2006 IEEE Military Communications Conference*, Washington, DC, Oct. 2006, pp. 1-7.

[31] B. Widrow et al., "Adaptive noise cancelling: Principles and applications," *IEEE Proceedings*, vol. 63, no. 12, pp. 1692-1716, Dec. 1975.

[32] D. A. Rich, S. Bo and F. A. Cassara, "Cochannel FM interference suppression using adaptive notch filters," *IEEE Transactions on Communications*, vol. 42, no. 7, pp. 2384-2389, July 1994.

[33] V. Aparin, G. J. Ballantyne, C. J. Persico and A. Cicalini, "An integrated LMS adaptive filter of TX leakage for CDMA receiver front ends," *IEEE Journal of Solid-State Circuits*, vol. 41, no. 5, pp. 1171-1182, May 2006.

[34] A. Yoshizawa and Y. Tsividis, "A Blocker-vigilant channel-select filter with adaptive IIP3 and power dissipation," in *2006 IEEE International Solid-State Circuits Conference Digest of Technical Papers*, San Francisco, CA, Feb. 2006, pp. 462-463.

[35] S. K. Reynolds, B. A. Floyd, T. J. Beukema, T. Zwick and U. R. Pfeiffer, "Design and compliance testing of a SiGe WCDMA receiver IC with integrated analog baseband," *Proceedings of the IEEE*, vol. 93, no. 9, pp. 1624-1636, Sept. 2005.

[36] S. Eriksson and K. Chen, "Offset-compensated switched-capacitor leapfrog filters," *Electronics Letters*, vol. 20, no. 18, pp. 731-733, Aug. 1984.

[37] R. G. Meyer, R. Eschenbach and W. M. Edgerley, "A wide-band feedforward amplifier," *IEEE Journal of Solid-State Circuits*, vol. SC-9, no. 6, pp. 422-428, Dec. 1974.

[38] V. Steel, D. Scott and S. Ludvik, "A 6-18 GHz, high dynamic range MMIC amplifier using a feedforward technique," in *1990 IEEE MTT-S International Microwave Symposium Digest*, Dallas, TX, vol. 2, May 1990, pp. 911-914.

[39] H.-S. Lee, R. D. Pollard and C. M. Snowden, "A high linearity and wide band feedforward amplifier design," in *25th European Microwave Conference*, Bologna, Italy, vol. 2, Oct. 1995, pp. 668-672.

[40] Y. K. G. Hau, V. Postoyalko and J. R. Richardson, "Compensation of amplifier nonlinear phase response to improve wideband distortion cancellation of feedforward amplifiers," *Electronics Letters*, vol. 33, no. 6, pp. 500-502, March 1997.

[41] Y. K. G. Hau, V. Postoyalko and J. R. Richardson, "Design and characterization of a microwave feed-forward amplifier with improved wide-band distortion cancellation," *IEEE Transactions on Microwave Theory and Techniques*, vol. 49, no. 1, pp. 200-203, Jan. 2001.

[42] A. Safarian, A. Shameli, A. Rofougaran, M. Rofougaran and F. De Flaviis, "Integrated blocker filtering RF front ends," in *2007 IEEE Radio Frequency Integrated Circuits Symposium*, Honolulu, HI, June 2007, pp. 13-16.

[43] S. Ayazian and R. Gharpurey, "Feedforward interference cancellation in radio receiver front-ends," *IEEE Transactions on Circuits and Systems II: Express Briefs*, vol. 54, no. 10, pp. 902-906, Oct. 2007.

[44] H. Darabi, "A blocker filtering technique for wireless receivers," in *2007 IEEE International Solid-State Circuits Conference Digest of Technical Papers*, San Francisco, CA, Feb. 2007, pp. 84-85.

[45] R. Poisel, *Introduction to Communication Electronic Warfare Systems*, Boston, MA: Artech House, 2002.

[46] V. G-Hansen and M. T. Ngo, “Radar dynamic range specification and measurement,” in *2009 International RADAR Conference - Surveillance for a Safer World*, Bordeaux, France, Oct. 2009, pp. 1-6.

[47] C. A. Putman, S. S. Rappaport and D. L. Schilling, “Tracking of frequency-hopped spread-spectrum signals in adverse environments,” *IEEE Transactions on Communications*, vol. 31, no. 8, pp. 955-964, Aug. 1983.

[48] D. J. Torrieri, “Fundamental limitations on repeater jamming of frequency-hopping communications,” *IEEE Journal on Selected Areas in Communications*, vol. 7, no. 4, pp. 569- 575, May 1989.

[49] J. D. Mosinski, “Electronic countermeasures,” in *Proceedings of the 1992 Tactical Communications Conference*, Fort Wayne, IN, vol. 1, Apr. 1992, pp. 191-195.

[50] B. H. Tanaka and R. L. Yuan, “Anti-jam performance of fast frequency hopped MFSK with coding against worst-case multitone jamming,” in *1987 IEEE Military Communications Conference*, Washington, DC, Oct. 1987, pp. 128-133.

[51] A. R. Hammons Jr., “Effects of partial-band jamming on space-time coded systems,” in *2004 IEEE Military Communications Conference*, Monterey, CA, vol. 3, Oct.-Nov. 2004, pp. 1623-1627.

[52] J. Ward, “Space-time adaptive processing for airborne radar,” M.I.T. Lincoln Laboratory, Lexington, MA, Technical Report TR1015, Dec. 1994.

[53] G. R. Cooper, “Tone jammer cancellation in a tapped-delay line correlator,” in *1984 IEEE Military Communications Conference*, Los Angeles, CA, Oct. 1984, pp. 469-473.

[54] R. N. Adams, L. L. Horowitz and K. D. Senne, “Adaptive main beam nulling for narrow-beam antenna systems,” *IEEE Transactions on Aerospace and Electronic Systems*, vol. AES-16, no. 4, pp. 509-516, July 1980.

[55] R. L. Fante, R. M. Davis and T. P. Guella, "Wideband cancellation of multiple mainbeam jammers," *IEEE Transactions on Antennas and Propagation*, vol. 44, no. 10, pp. 1402-1413, 1996.

[56] D. Madurasinghe and A. P. Shaw, "Mainlobe Jammer nulling via TSI finders: a space fast-time adaptive processor," *EURASIP Journal on Applied Signal Processing*, vol. 2006, Article ID 48789, pp. 1-13, 2006.

[57] S. M. Kogon, D. B. Williams and E. J. Holder, "Exploiting coherent multipath for mainbeam jammer suppression," *IEE Proceedings Radar, Sonar and Navigation*, vol. 145, no. 5, pp. 303-308, Oct. 1998.

[58] K. Pietikäinen, A. Silvennoinen, M. Hall and S.-G. Häggman, "IEEE 802.11G tolerance to narrowband jamming," in *2005 IEEE Military Communications Conference*, Baltimore, MD, Oct. 2005, pp. 1825-1830.

[59] K. Shi, Y. Zhou, B. Kelleci, T. W. Fischer, E. Serpedin and A. İ. Karşılayan, "Impacts of narrowband interference on OFDM-UWB receivers: analysis and mitigation," *IEEE Transactions on Signal Processing*, vol. 55, no. 3, pp. 1118-1128, March 2007.

[60] T. W. Fischer, B. Kelleci, K. Shi, A. İ. Karşılayan and E. Serpedin, "An analog approach to suppressing in-band narrow-band interference in UWB receivers," *IEEE Transactions on Circuits and Systems I: Regular Papers*, vol. 54, no. 5, pp. 941-950, May 2007.

[61] S. Vogeler, L. Broetje, K.-D. Kammeyer, R. Rueckriem and S. Fechtel, "Blind Bluetooth interference detection and suppression for OFDM transmission in the ISM band," in *Conference Record of the 37th Asilomar Conference on Signals, Systems and Computers*, Pacific Grove, CA, vol.1, Nov. 2003, pp. 703-707.

[62] D. G. Yoon, S. Y. Shin, W. H. Kwon and H. S. Park, "Packet error rate analysis of IEEE 802.11b under IEEE 802.15.4 interference," in *63rd IEEE Vehicular Technology Conference*, Melbourne, Australia, May 2006, pp. 1186-1190.

[63] A. Sikora and V. F. Groza, "Coexistence of IEEE802.15.4 with other Systems in the 2.4 GHz-ISM-band," in *Proceedings of the IEEE Instrumentation and Measurement Technology Conference*, Ottawa, Canada, May 2005, pp. 1786-1791.

[64] M. Petrova, L. Wu, P. Mähönen and J. Riihijärvi, "Interference measurements on performance degradation between colocated IEEE 802.11g/n and IEEE 802.15.4 networks," in *Proceedings of the Sixth International Conference on Networking*, Sainte-Luce, Martinique, France, Apr. 2007, pp. 93-93.

[65] J. Wel and M. Yan, "Bit error rate analysis of Wi-Fi and bluetooth under the interference of 2.45 GHz RFID," *The Journal of China Universities of Posts and Telecommunications*, vol. 14, pp. 89-93, Oct. 2007.

[66] Y. M. Shobowale and K. A. Hamdi, "Interference characterization in the unlicensed band," *IEEE Communications Letters*, vol. 10, no. 6, pp. 450-452, June 2006.

[67] J. T. MacDonald and D. R. Ucci, "Interference temperature limits of IEEE 802.11 protocol radio channels," in *2007 IEEE International Conference on Electro-Information Technology*, Chicago, IL, May 2007, pp. 64-69.

[68] S. Haykin, "Cognitive radio: brain-empowered wireless communications," *IEEE Journal on Selected Areas in Communications*, vol.23, no.2, pp.201-220, Feb. 2005.

[69] M. Biggs, F. Sanders and B. Ramsey, "Measurements to characterize aggregate signal emissions in the 2400-2500 MHz frequency range," National Telecommunications and Information Administration, Boulder, CO, Report 95-323, Aug. 1995.

[70] G. Watkins, "Potential interfering signals in software defined radio," in *6th IEEE High Frequency Postgraduate Student Colloquium*, Cardiff, UK, Sept. 2001, pp. 41-46.

[71] F. J. Block, "Performance of wideband digital receivers in jamming," in *2006 IEEE Military Communications Conference*, Washington, DC, Oct. 2006, pp. 1-7.

[72] A. A. Abidi, "Evolution of a software-defined radio receiver's RF front-end," in *2006 IEEE Radio Frequency Integrated Circuits (RFIC) Symposium*, San Francisco, CA, June 2006, pp. 1-4.

[73] A. Safarian, A. Shameli, A. Rofougaran, M. Rofougaran and F. De Flaviis, "An integrated RFID reader," in *2007 IEEE International Solid-State Circuits Conference Digest of Technical Papers*, San Francisco, CA, Feb. 2007, pp. 218-219.

[74] H. T. Friis, "Noise figures of radio receivers," *Proceedings of the IRE*, vol. 32, no. 7, pp. 419-422, July 1944.

[75] H. L. Krauss, C. W. Bostian and F. H. Raab, *Solid State Radio Engineering*, New York: John Wiley, 1980.

[76] A. van der Ziel, *Noise; sources, characterization, measurement*, New Jersey: Prentice-Hall, 1980.

[77] H.A. Haus et al., "Representation of noise in linear twoports," *Proceedings of the IRE*, vol. 48, no. 1, pp. 69-74, Jan. 1960.

[78] A. A. Abidi and J. C. Leete, "De-Embedding the noise figure of differential amplifiers," *IEEE Journal of Solid-State Circuits*, vol. 34, no. 6, pp. 882-885, June 1999.

[79] L. Belostotski and J. Haslett, "A Technique for differential noise figure measurement of differential LNAs," *IEEE Transactions on Instrumentation and Measurement*, vol. 57, no. 7, pp. 1298-1303, July 2008.

[80] J. Randa, "Multiport noise characterization and differential amplifiers," in *55th ARFTG Conference Digest*, Boston, MA, vol. 37, June 2000, pp. 1-10.

[81] V. Aparin, "Linearization of CDMA receiver front-ends," Ph.D. Dissertation, University of California, San Diego, CA, 2005.

[82] S. Maas, *Nonlinear Microwave and RF Circuits*, 2nd ed., Boston, MA: Artech House Publishers, 2003.

[83] N. Wiener, "Response of a nonlinear device to noise," M.I.T. Radiation Laboratory, Cambridge, MA, Technical Report V-16S, Apr. 1942.

[84] A. G. Bose, "A theory of nonlinear systems," M.I.T. Research Laboratory of Electronics, Cambridge, MA, Technical Report 309, May 1956.

[85] R. J. Gilmore and F. J. Rosenbaum, "Modeling of nonlinear distortion in GaAs MESFETs," in *MTT-S International Microwave Symposium Digest*, vol. 84, no. 1, May 1984, pp. 430-431.

[86] A. R. Kerr, "A technique for determining the local oscillator waveforms in a microwave mixer," *IEEE Transactions on Microwave Theory and Techniques*, vol. 23, no. 10, pp. 828-831, Oct. 1975.

[87] R. Melville, P. Feldmann, J. Roychowdhury, "Efficient multi-tone distortion analysis of analog integrated circuits," in *Proceedings of the IEEE 1995 Custom Integrated Circuits Conference*, Santa Clara, Ca, May 1995, pp. 241-244.

[88] M. Nakhla and J. Vlach, "A piecewise harmonic balance technique for determination of periodic response of nonlinear systems," *IEEE Transactions on Circuits and Systems*, vol. 23, no. 2, pp. 85-91, Feb. 1976.

[89] J. C. Pedro and N. B. Carvalho, *Intermodulation Distortion in Microwave and Wireless Circuits*, Norwood, MA: Artech House Publishers, 2003.

[90] S. Narayanan, "Transistor distortion analysis using Volterra series representation," *Bell System Technical Journal*, vol. 46, pp. 991-1024, May 1967.

[91] R. A. Minasian, "Intermodulation distortion analysis of MESFET amplifiers using the Volterra series representation," *IEEE Transactions on Microwave Theory and Techniques*, vol. MTT-28, no. 1, pp. 1-8, Jan. 1980.

[92] R. G. Sea and A. G. Vacroux, "On the computation of intermodulation products for a power series nonlinearity," *Proceedings of the IEEE*, vol. 57, no. 3, pp. 337-338, March 1969.

[93] K. Kundert, "Introduction to RF simulation and its application," *IEEE Journal of Solid-State Circuits*, vol. 34, no. 9, pp. 1298-1319, Sept. 1999.

[94] K. Kundert, *Steady-State Methods for Simulating Analog and Microwave Circuits*, Norwell, MA: Kluwer Academic, 1990.

[95] T. J. Aprille Jr.and T. N. Trick, "Steady-state analysis of nonlinear circuits with periodic inputs," *Proceedings of the IEEE*, vol. 60, no. 1, pp. 108-114, Jan. 1972.

[96] D. E. Bockelman, "The theory, measurement, and application of mode specific scattering parameters with multiple modes of propagation," Ph.D. Dissertation, University of Florida, 1997.

[97] D. E. Bockelman and W. R. Eisenstadt, "Combined differential and common-mode scattering parameters: theory and simulation," *IEEE Transactions on Microwave Theory and Techniques*, vol. 43, no. 7, pp. 1530-1539, Jul. 1995.

[98] D. E. Bockelman and W. R. Eisenstadt, "Pure-mode network analyzer for on-wafer measurements of mixed-mode S-parameters of differential circuits," *IEEE Transactions on Microwave Theory and Techniques*, vol. 45, no. 7, pp. 1071-1077, Jul. 1997.

[99] D. E. Bockelman, W. R. Eisenstadt and R. Stengel, "Accuracy estimation of mixed-mode scattering parameter measurements," *IEEE Transactions on Microwave Theory and Techniques*, vol. 47, no. 1, pp. 102-105, Jan. 1999.

[100] J. Dunsmore, "New methods & non-linear measurements for active differential devices," in *2003 IEEE MTT-S International Microwave Symposium Digest*, vol. 3, June 2003, pp. 1655-1658.

[101] K. Kundert, *A Test bench for differential circuits*, Designer's Guide Consulting, Los Altos, CA, Sept. 2006, available from www.designers-guide.org/Analysis/diff.pdf.

[102] W. R. Eisenstadt and D. E. Bockelman, "Common and differential crosstalk characterization on the silicon substrate," *IEEE Microwave and Guided Wave Letters*, vol. 9, no. 1, pp. 25-27, Jan. 1999.

[103] C. Seguinot, P. Kennis, J.-F. Legier, F. Huret, E. Paleczny and L. Hayden, "Multimode TRL-a new concept in microwave measurements: theory and experimental verification," *IEEE Transactions on Microwave Theory and Techniques*, vol. 46, no. 5, pp. 536-542, May 1998.

[104] H.-J. Eul and B. Schiek, “A generalized theory and new calibration procedures for network analyzer self-calibration,” *IEEE Transactions on Microwave Theory and Techniques*, vol. 39, no. 4, pp. 724-731, April 1991.

[105] J.C. Tippet and R.A. Speciale, “A rigorous technique for measuring the scattering matrix of a multiport device with a 2-port network analyzer,” *IEEE Transactions on Microwave Theory and Techniques*, vol. 30, no. 5, pp. 661-666, May 1982.

[106] R.B. Marks, “A multiline method of network analyzer calibration,” *IEEE Transactions on Microwave Theory and Techniques*, vol. 39, no. 7, pp. 1205-1215, July 1991.

[107] S. Sercu, and L. Martens, “Characterizing n-port packages and interconnections with a 2-port network analyzer,” in *6th IEEE Topical Meeting on Electrical Performance of Electronic Packaging*, San Jose, CA, Oct. 1997, pp.163-166.

[108] E. Vanlil, “Comments on ’A rigorous technique for measuring the scattering matrix of a multiport device with a 2-port network analyzer’,” *IEEE Transactions on Microwave Theory and Techniques*, vol. 33, no. 3, pp. 286-287, March 1985.

[109] H. Dropkin, “Comments on A rigorous technique for measuring the scattering matrix of a multiport device with a 2-port network analyzer,” *IEEE Transactions on Microwave Theory and Techniques*, vol. 31, no. 1, pp. 79-81, Jan. 1983.

[110] R. G. Meyer and W. D. Mack, “A 1-GHz BiCMOS RF front-end IC,” *IEEE Journal of Solid-State Circuits*, vol. 29, no. 3, pp. 350-355, March 1994.

[111] D. K. Shaeffer and T. H. Lee, “A 1.5-V, 1.5-GHz CMOS low noise amplifier,” *IEEE Journal of Solid-State Circuits*, vol. 32, no. 5, pp. 745-759, May 1997.

[112] A. Ismail and A. A. Abidi, “A 3-10GHz low-noise amplifier with wideband LC-ladder matching network,” *IEEE Journal of Solid-State Circuits*, vol. 39, no. 12, pp. 2269-2277, Dec. 2004.

[113] A. Bevilacqua and A. M. Niknejad, “An ultrawideband CMOS low-noise amplifier for 3.1-10.6-GHz wireless receivers,” *IEEE Journal of Solid-State Circuits*, vol. 39, no. 12, pp. 2259-2268, Dec. 2004.

[114] X. Duo, L.-R. Zheng, M. Ismail and H. Tenhunen, "Analysis of lossy packaging parasitics for common emitter LNA in system-on-package," in *13th IEEE Topical Meeting on Electrical Performance of Electronic Packaging*, Portland, OR, Oct. 2004, pp. 75-78.

[115] R. C. Jaeger, "Common-mode rejection limitations of differential amplifiers," *IEEE Journal of Solid-State Circuits*, vol. 11, no. 3, pp. 411-417, June 1976.

[116] J. Lee and Y. Kim, "CMOS low noise amplifier design techniques using shunt resistive feedback," in *2005 Asia-Pacific Microwave Conference Proceedings*, vol. 3, Suzhou, China, Dec. 2005, pp. 1-4.

[117] C. W. Kim, M.-S. Kang, P.-T. Anh, H.-T. Kim, and S.-G. Lee, "An ultra-wideband CMOS low noise amplifier for 3-5-GHz UWB system," *IEEE Journal of Solid-State Circuits*, vol. 40, no. 2, pp. 544-547, Feb. 2005.

[118] Y. Lu, R. Krithivasan, W.-M. L. Kuo and J. D. Cressler, "A 1.8-3.1 dB noise figure (3-10 GHz) SiGe HBT LNA for UWB applications," in *2006 IEEE Radio Frequency Integrated Circuits (RFIC) Symposium*, San Francisco, CA, June 2006, pp. 1-4.

[119] F. Bruccoleri, E. A. M. Klumperink and B. Nauta, "Wide-band CMOS low-noise amplifier exploiting thermal noise canceling", *IEEE Journal of Solid-State Circuits*, vol. 39, no. 2, pp. 275-282, Feb. 2004.

[120] N. Shiramizu, T. Masuda, M. Tanabe and K. Washio, "A 3-10 GHz bandwidth low noise and low-power amplifier for full-band UWB communications in 0.25-um SiGe BiCMOS technology," in *2005 IEEE Radio Frequency Integrated Circuits (RFIC) Symposium*, Long Beach, CA, June 2005, pp. 39-42.

[121] D. J. Allstot, X. Li, and S. Shekhar, Design considerations for CMOS low-noise amplifiers, *Proc. IEEE Radio Frequency Integrated Circuits Symp.*, pp.97-100, June 2004.

[122] W. Zhuo et al., "A capacitor cross-coupled common-gate low-noise amplifier," *IEEE Transactions On Circuits and Systems II: Express Briefs*, vol. 52, no. 12, pp. 875-879, Dec. 2005.

[123] Y. Ge and K. Mayaram, "A comparative analysis of CMOS low noise amplifiers for RF applications," in *Proceedings of the 1998 IEEE International Symposium on Circuits and Systems*, vol. 4,Monterey, CA, May-June 1998, pp. 349-352.

[124] B. M. Ballweber, R. Gupta, and D. J. Allstot, "A fully integrated 0.5-5.5 GHz CMOS distributed amplifier," *IEEE Journal of Solid-State Circuits*, vol. 35, no. 2, pp. 231-239, Feb. 2000.

[125] R.-C. Liu, C.-S. Lin, K.-L. Deng and H. Wang, "A 0.5-14G-Hz 10.6dB CMOS cascode distributed amplifier," in *2003 Symposium on VLSI Circuits Digest of Technical Papers*, Kyoto, Japan, June 2003, pp. 139-140.

[126] B. Stengel and B. Thompson, "Neutralized differential amplifiers using mixed-mode S-parameters," in *2003 IEEE MTT-S International Microwave Symposium Digest*, vol. 1, Philadelphia, PA, June 2003, pp. A197-A200.

[127] P. Gamand, "Analysis of the oscillation conditions in distributed amplifiers," *IEEE Transactions on Microwave Theory and Techniques*, vol. 37, no. 3, pp. 637-640, March 1989.

[128] D. Lieberman, "Cross-modulation figure of merit for transistor amplifier stages," *Proceedings of the IEEE*, vol. 58,no. 7,pp. 1063-1071, July 1970.

[129] W. Sansen, "Distortion in elementary transistor circuits," *IEEE Trans. Circuits Syst. II, Analog Digit. Signal Process.*, vol. 46,no. 3,pp. 315-325, March 1999.

[130] C. Cho, W. R. Eisenstadt, B. Stengel and E. Ferrer, "IIP3 estimation From the gain compression curve," *IEEE Transactions on Microwave Theory and Techniques*, vol. 53, no. 4, pp. 1197-1202, April 2005.

[131] G. Qin, N. Jiang, G. Wang and Zh. Ma, "SiGe HBT linearity comparison between CE and CB configurations," *Semiconductor Science and Technology*, vol. 22, no. 1, pp. S216-S220, Jan 2007.

[132] Compact Model Development Staff, *BiCMOS-8HP Model Reference Guide*, IBM Microelectronics Division, 2007.

[133] Mixed Signal Technology Development Staff, *BiCMOS8HP Design Manual*, IBM Microelectronics Division, 2007.

[134] H. K. Gummel and H. C. Poon, “An integral charge-control model of bipolar transistors,” *Bell System Technical Journal*, vol. 49, no. 5, pp. 827-852, May-June 1970.

[135] C. C. McAndrew et al., “VBIC95, the vertical bipolar inter-company model,” *IEEE Journal of Solid-State Circuits*, vol. 31, no. 10, pp. 1476-1483, Oct. 1996.

[136] J. Dunn et al., “Bipolar transistor having raised extrinsic base with selectable self-alignment and methods of forming same,” U.S. Patent 20060081934 A1, Apr. 20, 2006.

[137] J. M. Rollett, “Stability and power-gain invariants of linear twoports,” *IRE Transactions on Circuit Theory*, vol. 9, no. 1, pp. 29-32, March 1962.

[138] P. J. Owens and D. Woods, “Reappraisal of the unconditional stability criteria for active 2-port networks in terms of S parameters,” *Electronics Letters*, vol. 6, no. 10, pp. 315-315, May 1970.

[139] M. L. Edwards and J. H. Sinsky, “A new criterion for linear 2-port stability using a single geometrically derived parameter,” *IEEE Transactions on Microwave Theory and Techniques*, vol. 40, no. 12, pp. 2303-2311, Dec. 1992.

[140] A. Platzker and W. Struble, “Rigorous determination of the stability of linear n-node circuits from network determinants and the appropriate role of the stability factor K of their reduced two-ports,” in *Third International Workshop on Integrated Nonlinear Microwave and Millimeterwave Circuits*, Duisburg, Germany, Oct. 1994, pp. 93-107.

[141] A. Platzker, W. Struble and K. T. Hetzler, “Instabilities diagnosis and the role of K in microwave circuits,” in *1993 IEEE MTT-S International Microwave Symposium Digest*, vol. 3, Atlanta, GA, June 1993, pp. 1185-1188.

[142] D. M. Pozar, *Microwave Engineering*, 2nd ed. New York: John Wiley, 1998.

[143] G. Gonzalez, *Microwave Transistor Amplifiers*, 2nd ed. New Jersey: Prentice Hall, 1997.

[144] K. Kurokawa, "Power waves and the scatering matrix," *IEEE Transactions on Microwave Theory and Techniques*, vol. 13, no. 2, pp. 194-202, March 1965.

[145] G. Matthaei, L. Young and E.M.T. Jones, *Microwave Filters, Impedance-matching Networks and Coupling Structures*, New York:McGraw-Hill, 1964.

[146] G. L. Matthaei, "Comb-Line band-pass filters of narrow or moderate bandwidth," *Microwave Journal*, vol.6, pp.82-91, Aug. 1963.

[147] W. J. Getsinger, "Coupled rectangular bars between parallel plates," *IRE Transactions on Microwave Theory and Techniques*, vol. 10, no. 1, pp.65-72, Jan. 1962.

[148] R. M. Kurzrok, "Design of comb-Line band-pass filters," *IEEE Transactions on Microwave Theory and Techniques*, vol. 14, no. 7, pp. 351-353, July 1966.

[149] Ch. Wang, "Determining dielectric constant and loss tangent in FR-4," UMR EMC Laboratory, University of Missouri, Rolla, MO, Technical Report TR00-1-041, Mar. 2000.

[150] A. Pelteku and J. McNeill, "Analysis and implementation of an RF system with real time autonomous and intelligent control", in *2007 Sarnoff Symposium Student Paper Proceedings*, Princeton, NJ, May 2007, pp. 1-4.

[151] A. Pelteku and J. McNeill, "Analysis and implementation of a phase cancellation technique used in adaptive interference suppression," in *24th Biennial Symposium on Communications*, Kingston, ON, June 2008, pp. 298-301.

[152] E. S. Sabisky and H. J. Gerritsen, "Measurements of dielectric constant of rutile (TiO_2) at microwave frequencies between 4.2° and 300°K," *Journal of Applied Physics*, vol. 33, no. 4, pp. 1450-1453, Apr. 1962.

[153] A. Okaya and L. F. Barash, "The dielectric microwave resonator," *Proc. IRE*, vol. 50, no. 10, pp. 2081-2092, Oct. 1962.

[154] S. B. Cohn, "Microwave bandpass filters containing high-Q dielectric resonators,"

IEEE Transactions on Microwave Theory and Techniques, vol. MTT-16, no. 4, pp. 218-227, Apr. 1968.

[155] A. Karp, H. J. Shaw and D. K. Winslow, “Circuit properties of microwave dielectric resonators,” *IEEE Transactions on Microwave Theory and Techniques*, vol. MTT-16, no. 10, pp. 818-828, Oct. 1968.

[156] R. V. D’Aiello and H. J. Prager, “Dielectric resonators for microwave applications,” *IEEE Transactions on Microwave Theory and Techniques* (Correspondence), vol. MTT-12, no. 5, pp. 549550, Sept. 1964.

[157] E. O. Ammann and R. J. Morris, “Tunable, dielectric-loaded microwave cavities capable of high Q amd high filling factor,” *IEEE Transactions on Microwave Theory and Techniques*, vol. MTT-11, no. 6, pp. 528-542, Nov. 1963.

[158] Toko, “Dielectric filters for surface mounting,” 4DFA-1575B-12 datasheet, Feb. 2008.

[159] R. N. Hardin, E. J. Downey and J. Munushian, “Electronically-variable phase shifters utilizing variable capacitance diodes,” *Proc. IRE*, vol. 48, pp. 944-945, May 1960.

[160] C.-L. Chen et al., “A low-loss Ku-band monolithic analog phase shifter,” *IEEE Transactions on Microwave Theory and Techniques*, vol. MTT-35, No. 3, pp. 315-320, March 1987.

[161] S. Lucyszyn and I. D. Robertson, “Synthesis techniques for high performance octave bandwidth 180° analog phase shifters,” *IEEE Transactions on Microwave Theory and Techniques*, vol. 40, No. 4, pp. 731-740, April 1992.

[162] R. V. Garver, “360° varactor linear phase modulator,” *IEEE Transactions on Microwave Theory and Techniques*, vol. MTT-17, No. 3, pp. 137-147, March 1969.

[163] J. H. Qureshi et al., “A low-loss compact linear varactor based phase-shifter,” in *2007 IEEE Radio Frequency Integrated Circuits Symposium*, Honolulu, HI, June 2007, pp. 453-456.

[164] D. M. Klymyshyn, S. Kumar and A. Mohammadi, "Linear reflection phase shifter with optimized varactor gamma," *Electronics Letters*, vol. 33, no. 12, pp. 1054-1055, June 1997.

[165] K. Buisman et al., "Distortion-free varactor diode topologies for RF adaptivity," in *2005 IEEE MTT-S International Microwave Symposium Digest*, June 2005, pp. 157-160.

[166] M/A-COM Inc., "Low tuning voltage/low Rs silicon hyperabrupt varactor diode," MA4ST1200 Series datasheet, Jan. 2008.

[167] Hittite Microwave, "GaAs MMIC SMT voltage-variable attenuator, DC-8 GHz," HMC346MS8G datasheet, Jan. 2008.

[168] Hittite Microwave, "Designing with the HMC346MS8G voltage variable attenuator," HMC346MS8G Product Note, pp. 67-76.

[169] Texas Instruments, "100-MHz low-noise high-speed amplifiers," THS4031/THS4032 datasheet, Jan. 2008.

[170] Krytar, "1-18 GHz 180°hybrid coupler," 4010180 datasheet, Feb. 2008 [Revised April 2009].

[171] Agilent Technologies, *RFIC dynamic link user guide*, Santa Clara, CA, Sept. 2004, Available: http://eesof.tm.agilent.com/docs/adsdoc2004A/pdf/dynlnkug.pdf.

[172] T. Oetiker, H. Partl, I. Hyna and E. Schlegl, "The not so short introduction to $\LaTeX\,2_\varepsilon$," *ctan.org*, ver. 4.26, Sept. 2008. [Online]. Available: http://tug.ctan.org/tex-archive/info/lshort/english/lshort.pdf. [Accessed: Mar. 12, 2009].